

SWOT* Project

MISSION PERFORMANCE AND ERROR BUDGET

Revision A

Prepared by:

Daniel Esteban Fernandez
KaRIn Lead System Engineer

Date

Approved:

Brian Pollard
Payload System Engineer

Date

Parag Vaze
Project Manager

Date

Concurred:

Robert Abelson
Project System Engineer

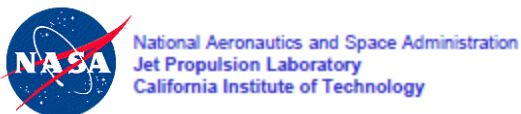
Date

Paper copies of this document may not be current and should not be relied on for official purposes. The current version is in the Product Data Management System (PDMS): <https://pdms.jpl.nasa.gov/>

This document has been reviewed and determined not to contain export controlled technical data.

** Proposed Mission - Pre-decisional - for Planning & Discussion Purposes Only*

October 7, 2013
JPL D-79084



CONTRIBUTIONS

This objective of this document is to describe the overall performance and error budget of the SWOT mission concept. A document like this is never the outcome of a single person, but rather includes a significant amount of work performed by a large team of people, in the form of discussions, exchanges, and analysis. In particular, the author would like to acknowledge the critical work and numerous contributions of Eva Peral, Ernesto Rodriguez, Brian Pollard, Dalia McWatters, Richard Hughes, Shannon Brown, Lee Fu, Clement Ubelmann, Bruce Haines, Shailen Desai, Dhemitrios Boussalis, Phil Callahan, and Brent Williams, among others.

Table of Contents

CONTRIBUTIONS	3
Table of Contents	4
1 SCOPE	7
2 REFERENCES AND APPLICABLE DOCUMENTS	8
3 TERMINOLOGY AND ABBREVIATIONS	9
4 SWOT MEASUREMENT OVERVIEW	10
4.1 Introduction	10
4.2 Ocean Measurement	11
4.3 Hydrology Measurement	13
4.4 KaRIn Overview	14
4.5 KaRIn Onboard processing overview	16
5 OCEAN MEASUREMENT REQUIREMENTS AND ERROR BUDGET	17
5.1 Error budget for ocean wavelengths < 1,000 km	18
5.1.1 Measurement sampling	19
5.1.2 Minimum wavelength and aliasing considerations	19
5.1.3 Error budget top-level break-down	21
5.2 Error budget for ocean wavelengths > 1,000 km	23
5.3 OCEAN MEDIA/WAVE ERROR REQUIREMENTS	24
5.3.1 Sea-State Bias	24
5.3.2 Ionosphere	25
5.3.3 Dry troposphere	25
5.3.4 Wet troposphere	25
5.4 OCEAN RANDOM ERROR REQUIREMENTS	29
5.4.1 Ocean backscatter	30
5.4.2 Thermal decorrelation	32
5.4.3 Geometric Decorrelation	32
5.4.4 Angular decorrelation	35
5.4.5 Overall Random performance	37

5.5	OCEAN SYSTEMATIC ERROR REQUIREMENTS	38
5.5.1	Overview of Roll Drift Errors	39
5.5.2	Overview of Differential Phase Drift Errors	42
5.5.3	Overview of Baseline Dilation Drift Errors	45
5.5.4	Timing (Common Group Delay) Drift Errors	47
5.5.5	Orbit Radial Knowledge Errors	48
5.5.6	Wave Averaging Errors	51
5.5.7	Processing and Bias correction errors	53
5.5.8	Wavelength drifts	54
6	HYDROLOGY MEASUREMENT REQUIREMENTS AND ERROR BUDGET	55
6.1	Height and slope accuracy requirements	55
6.1.1	KaRin Performance for Hydrology	56
6.2	Cross-over correction for Systematic Error removal	56
6.3	Hydrology Random Error Requirements	59
6.3.1	Height Error	59
6.3.2	Slope Error	60
6.4	Systematic errors	62
6.4.1	Orbit Knowledge Error Requirements	65
6.5	LAND MEDIA ERROR REQUIREMENTS	67
6.5.1	Wet troposphere	67
6.6	Dry troposphere and Ionosphere	68
6.7	Classification accuracy	70
7	Flagging Requirements	73
8	Pointing Error Budget	75
8.1	Absolute Pointing Control Requirements	75
8.2	Relative pointing knowledge requirements	76
8.3	Absolute pointing knowledge requirements	77
8.4	Pointing requirements summary	77
9	Timing Correlation Error Budget	79
10	Appendix A: Proposed SWOT Orbit	81

11	Appendix B: Derivation of the spectral form of the slope error	83
----	--	----

1 SCOPE

This document presents the top-down error budget for the SWOT mission concept, including all the different systems and subsystems that have a significant contribution to the overall performance of the mission. It is structured in several parts corresponding to the key error contributions for both oceanography and hydrology, with a discussion of the main contributors to the global performance: Flight System, Payload and Payload Instruments, S/C bus, Algorithms, and Mission System. The error budget presented in this document forms the basis for the performance requirements for the SWOT Mission levied across all these elements.

2 REFERENCES AND APPLICABLE DOCUMENTS

- [1] SWOT Science Requirement Document, JPL D-61923.
- [2] SWOT L2 Mission Requirements, JPL D- D-61935.
- [3] Lee-Lueng Fu, D. Alsdorf, R. Morrow, E. Rodriguez, N. Mognard, Ed.: The Surface Water and Ocean Topography Mission. JPL Publication 12-05, February 2012.
- [4] Vandemark, D., B. Chapron, J. Sun, G. H. Crescenti, H. C. Graber, 2004: Ocean wave slope observations using radar backscatter and laser altimeters. J. Phys. Oceanogr., 34, 2825–2842. doi: <http://dx.doi.org/10.1175/JPO2663.1>.
- [5] Freilich, M.H. and P.G. Challenor, 1994: A new approach for determining fully empirical altimeter wind speed model functions. J. Geophys. Res., 99, 25,051-25,062.
- [6] Chelton, D. (1994). The sea state bias in altimeter estimates of sea level from collinear analysis of TOPEX data. Journal of Geophysical Research 99: doi: 10.1029/94JC02113. issn: 0148-0227.
- [7] Gaspar, P., Ogor, F., Le Traon, P. and Zanife, O. (1994). Estimating the sea state bias of the TOPEX and POSEIDON altimeters from crossover differences. Journal of Geophysical Research 99: doi: 10.1029/94JC01430. issn: 0148-0227.
- [8] J.Y Cherniawsky, M.G.G Foreman, and et al. Ocean tides from topex/poseidon sea level data. Journal of Atmos. And Oceanic Tech.,18, 2001.
- [9] F.Gatelli, A.M.Guamieri, F.Parizzi, P.Pasquali, C.Prati, and F.Rocca. The wavenumber shift in sar interferometry. Geoscience and Remote Sensing, IEEE Transactions on, 32(4):855–865, Jul. 1994.

3 TERMINOLOGY AND ABBREVIATIONS

ADC	Analog-to-Digital Converter
AMR	Advanced Microwave Radiometer
CoG	Center of Gravity
EIK	Extended Interaction Klystron
EMB	Electromagnetic Bias
ISLR	Integrated Side Lobe Ratio
LNA	Low-Noise Amplifier
OBP	Onboard Processor
POD	Precision Orbit Determination
PRF	Pulse Repetition Frequency
PRI	Pulse Repetition Interval
RF	Radio Frequency
RSS	Root-Square Sum
RX	Receive (event)
SAR	Synthetic Aperture Radar
SNR	Signal-to-Noise Ratio
SRD	Science Requirements Document
SSB	Sea-State Bias
SSH	Sea Surface Height
TRF	Transmit Repetition Frequency
TX	Transmit (event)
WSOA	Wide-Swath Ocean Altimeter

4 SWOT MEASUREMENT OVERVIEW

4.1 Introduction

The proposed SWOT mission would measure the water elevation of the global oceans, as well as terrestrial water bodies, to answer key scientific questions on the kinetic energy of the ocean circulation, the spatial and temporal variability of the world’s surface freshwater storage and discharge, and to provide societal benefits on predicting climate change, coastal zone management, flood prediction, and water resources management.

The core oceanographic objective is to characterize the ocean mesoscale and sub-mesoscale circulation at spatial resolutions of 15 km and larger. Current altimeter constellations can only resolve the ocean circulation at resolutions larger than 200-300 km [3]. Fundamental questions on the dynamics of ocean variability at scales shorter than 300 km, the mesoscale and sub-mesoscale processes, such as the formation, evolution, and dissipation of eddy variability (including narrow currents, fronts, and quasi-geostrophic turbulence) and its role in air-sea interaction, are to be addressed by these new observations. Global study of the circulation in the scales between 15 and 300 km are essential for quantifying the kinetic energy of ocean circulation and the ocean uptake of climate relevant tracers such as heat and carbon. The SWOT mission concept is the only available option to open a window on these dynamics.

SWOT would also target hydrology science objectives, by providing measurements of water storage changes in terrestrial surface water bodies and would provide estimates of discharge in large (50 m-100 m width) rivers, globally.

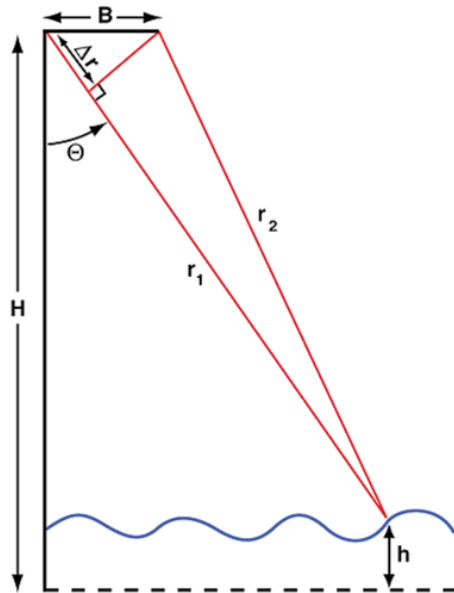


Figure 1. The interferometric measurement concept is basically triangulation. The baseline (mechanically stable) forms the base. The range is determined by the system timing accuracy, and the difference between the two sides, Δr , is obtained from the phase difference, ϕ , between the two radar channels.

The core instrument for the SWOT mission concept is the Ka-Band Radar Interferometer (KaRIn) instrument, originally developed from the efforts of the Wide Swath Ocean Altimeter (WSOA). While conventional altimetry relies on the power and the specific shape of the leading edge of the return waveform, which is only available for the nadir point, the interferometric technique relies on the measurement of the relative delay between the signals measured by two antennas separated by a known distance (hereafter termed “baseline”), together with the system ranging information, to derive the height for every imaged pixel in the scene. For a given point on the ground, a triangle is thus formed by the baseline B , and the range distance to the two antennas, r_1 and r_2 , which can be used to geolocate in the plane of the observation (see Figure 1). Using radar pulses transmitted from one of the antennas to form the interferometric pair (this operation mode is commonly referred to as “single transmit antenna”), the range difference between r_1 and r_2 is determined by the relative phase difference ϕ between the two signals as given by the following equation:

$$\phi = 2kr_1 - k(r_1 + r_2) \approx kB \sin(\theta)$$

where θ is the look angle, and k is the electromagnetic wavenumber. From the phase measurement, and with precise knowledge of the range distance and the look direction θ , the

height h above a reference plane can be obtained using the equation:

$$h \approx H - r_1 \cos(\theta)$$

where H is the platform height. The KaRIn instrument would be complemented with the following suite of instruments:

- A dual-frequency (C- and Ku-band) Nadir Altimeter, similar to the Poseidon altimeter flown on the Jason series,
- A three-frequency microwave radiometer, similar to the Advanced Microwave Radiometer (AMR) flown on the Jason series,
- A DORIS receiver, a GPS receiver, and a Laser Retroreflector Array (LRA) for Precise Orbit Determination (POD).

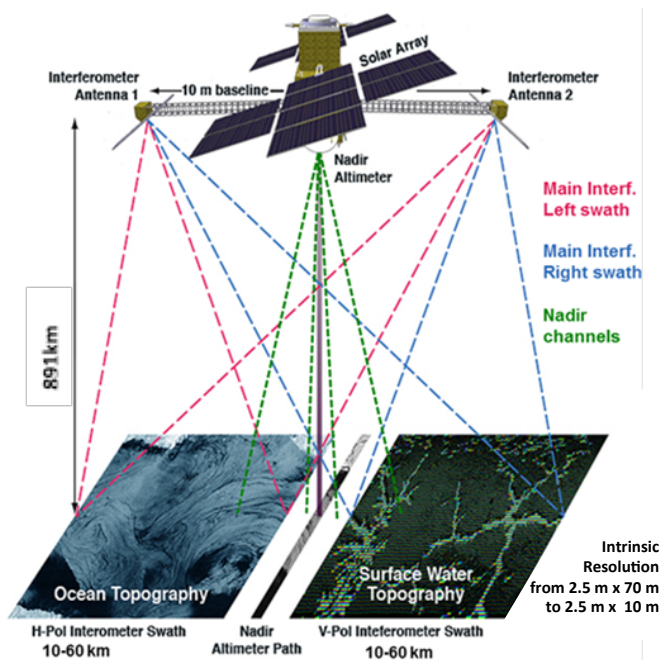


Figure 2. Conceptual illustration of the SWOT mission measurement concept. The Ka-band Radar Interferometer (KaRIn) illuminates two swaths of 50 km (± 10 to 60 km on each side of the nadir track).

Figure 2 shows an artist's concept of the observatory with the antennas in the deployed state. In order to minimize the impact of tidal signals aliasing into the ocean topography data, while still covering important polar ocean areas, the satellite would operate during the nominal science mission in a 20.86 day repeat, non sun-synchronous orbit, at an altitude of 890.5 km and 77.6 deg inclination. An initial calibration phase 1-day repeat orbit would also be established, at an altitude of 857 km and 77.6 deg inclination, with the main objectives of: 1) obtain fast-repeat ocean observations towards the calibration and validation objectives; and 2) understand the decorrelation times of the ocean mesoscale and sub-mesoscale processes, which are expected to suffer from relatively fast temporal decorrelations at the short ocean scales.

4.2 Ocean Measurement

For SWOT, the ocean measurement drives the required performance of the system, since centimetric accuracies are required to resolve sub-mesoscale processes. The high accuracy requirements for ocean topography measurements imply that the measurement error budget must be well understood and properly sub-allocated. The ocean measurement is conceptualized differently in two different wavelength regions: a) the region below 1,000 km, where the fundamental topographic measurement is provided by KaRIn, as a swath measurement; and b) the region above 1,000 km, where the fundamental measurement is provided by the nadir altimeter as a nadir-only measurement.

In general, several sources of errors limit the accuracy of the final height measurement:

- 1) **Random errors.** These are errors related to the variance of the height (or phase) measurements, most notably the intrinsic noise of the interferometer, as well as other destructive errors that increase the variance, and which cannot be corrected on the ground. The random error

contribution depends on several factors, such as the system signal-to-noise ratio (SNR), the length of the interferometric baseline, and the processing algorithm. Additionally, it drives the pointing control stability of the observatory and the deployment accuracy and stability of the KaRIn antennas to minimize SNR loss over the desired swath on the ground.

2) **S/C and instrument systematic errors.** These are non-destructive errors typically associated with drifts or range variations that end up introducing bias in the measured heights, and which could be corrected if known. Some of the most important systematic errors are associated with a baseline roll, a change in the baseline length, and to range (or timing) and phase drift errors. Lack of knowledge in the spacecraft roll angle, changes in the baseline due to thermal contraction or expansion, system timing and phase drifts introduced by the antennas or the KaRIn electronics would induce height errors.

3) **Orbit and electromagnetic propagation (or media) errors.** The ranges measured onboard by the interferometer must be corrected to account for additional delays caused by propagation effects through the ionosphere and troposphere. These include wet and dry troposphere errors, as well as ionosphere errors, which include cross-track variations within the swath. While KaRIn would not directly measure the tropospheric and ionospheric signals, the SWOT radiometer would be used to obtain range corrections of the wet troposphere, which is the largest source of media errors. The dry troposphere and ionosphere signals at Ka-band constitute relatively small errors for the ocean scales of interest (ocean wavelengths < 1,000 km). Since they do not drive the error budget, they are allocated without requiring specific corrections during ground processing. Lastly, the POD suite of instruments would be used to correct radial orbit errors.

4) **Wave-related errors,** such as Sea-State (also termed “electromagnetic”, EM) Bias (SSB) and significant wave height (SWH) errors. The spatial variability of the wave and wind fields will introduce height biases.

The table below shows the science traceability matrix for oceanography, mapping the science objectives into science requirements, and in turn into instrument functional requirements.

Science Objectives	Scientific Measurement Requirements	Instrument Functional Requirements
Measure mesoscale and sub-mesoscale activity, including: <ul style="list-style-type: none"> • fronts, eddies, and boundary currents; • eddy mean-flow interactions, eddy transports, and the role of eddies in climate; • physical-biological interactions and the role of eddies in the carbon cycle; • coastal tides and open ocean internal tides • and coastal currents. • Estimate global change in mesoscale and sub-mesoscale dynamics at sub-monthly, seasonal, and annual time scales 	<ul style="list-style-type: none"> • Monitor global mesoscale and sub-mesoscale activity (ocean wavelengths ranging from 15 km to 1,000 km) through the measurement of sea surface height (SSH) with a spatial resolution no coarser than 2 km x 2 km. • Global coverage of sea surface height measurements for ice free oceans (up to 74-78 deg latitude), with a repeat cycle of 21 to 23 days, with minimal tidal aliasing. • The SSH accuracy shall meet the envelope listed in the SRD. 	<p><u>Ka-band Interferometer:</u></p> <ul style="list-style-type: none"> • Height measurements with 2 km x 2 km resolution and ensemble average of the height error spectrum not to exceed the envelope listed in the SRD for wavelengths < 1,000 km • Provide above measurement accuracy over a two swaths of 50 km each. <p><u>Microwave Radiometer:</u></p> <ul style="list-style-type: none"> • Resolve wet tropospheric correction. <p><u>Nadir Altimeter (Ku and C band):</u></p> <ul style="list-style-type: none"> • Height measurement with Jason class performance. <p><u>POD Suite:</u></p> <ul style="list-style-type: none"> • Determine orbit.
	<ul style="list-style-type: none"> • 42 month operation for capturing 3 seasonal cycles and inter-annual variability. 	<ul style="list-style-type: none"> • 42 month reliability

A high-level view of the flow of the key error budget components for wavelengths < 1,000 km is illustrated in the figure below, where KaRIn would provide the basic height measurement. For simplicity, those elements that are pass-through are not shown.

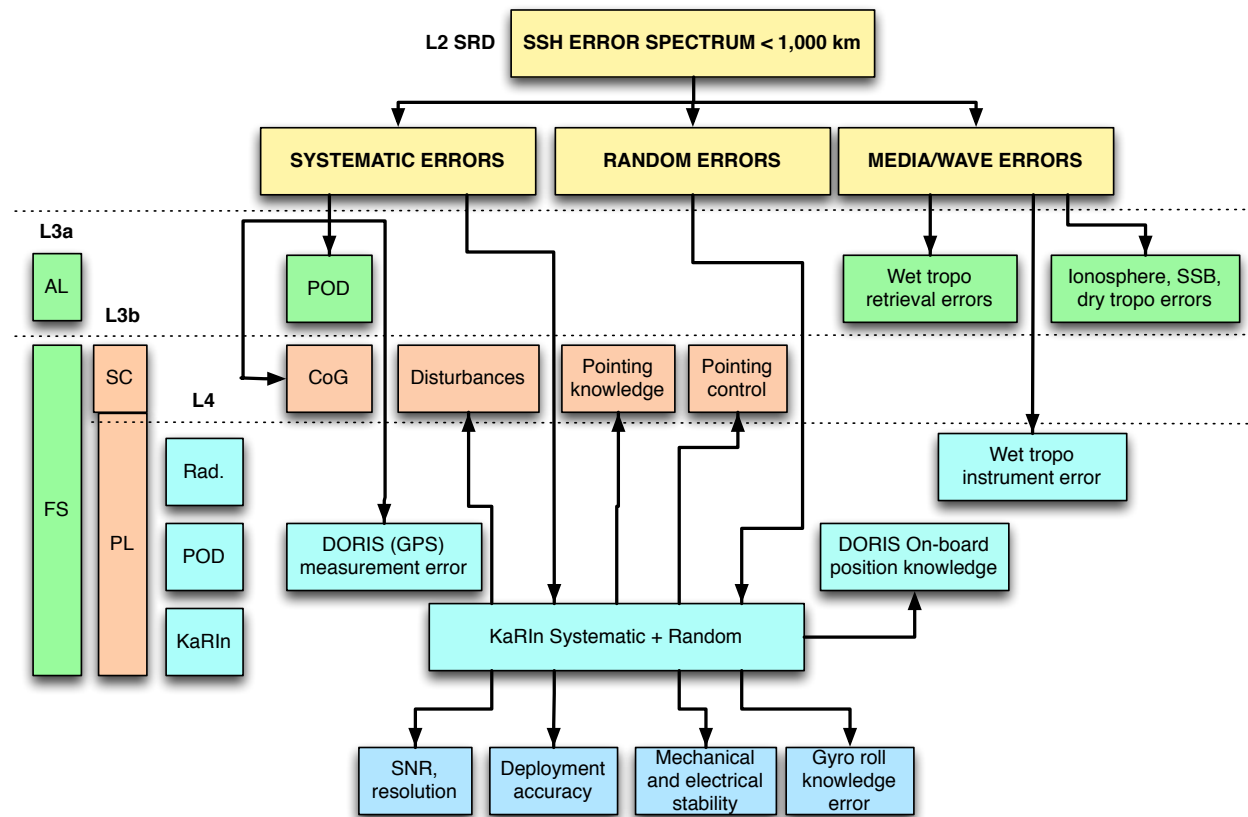


Figure 3. Overview of the key error budget components across levels for $\lambda < 1,000$ km.

The Nadir Altimeter would provide the measurements for wavelengths longer than 1,000 km, with a required accuracy equal or better than the Jason series of altimeters, radiometers, and POD.

4.3 Hydrology Measurement

Storage of water at and near the land surface is a key term in the terrestrial water balance, yet the dynamics, and even the amount, of water stored in lakes, streams, reservoirs, and wetlands globally is poorly known [3]. Furthermore, surface water stage and/or slope is a key measurement for derivation of streamflow, yet such measurements are currently only made at points via in situ methods, the spatial distribution of which is highly non-uniform, and mostly concentrated in the most populous parts of the developed world.

The primary SWOT hydrology science question relates to the global water cycle: “What is the spatial and temporal variability in the world’s terrestrial surface water storage and discharge? How can we predict these variations more accurately?” The ability of SWOT to provide Water Surface Elevation (WSE), as well as freshwater discharge and storage change in lakes, reservoirs, wetlands, and rivers at the global scale, would provide a tremendous leap forward in understanding the dynamics of the land surface branch of the global water cycle. The second SWOT hydrology science question is: “How much water is stored on a floodplain and

subsequently exchanged with its main channel? How much carbon is potentially released from inundated areas?” SWOT measurements would provide the means to study the nature of the floodplain hydraulics. A better understanding of the global water cycle would allow for a detailed investigation of linkages with the global Carbon cycle. The third SWOT hydrology science question is: “What policy implications would freely available water storage data have for water management? Can health issues related to waterborne diseases be predicted through better mappings?” For trans-boundary rivers, where water resources and flood risk management are international in nature, SWOT measurements of upstream reservoir levels could prove useful.

These science questions lead to the following key mission performance requirements, as specified in [1]:

- a) The area of all water bodies greater than 250 m x 250 m, and rivers wider than 100 m must be measured with a relative error $\leq 15\%$ (1-sigma) of the total water body area.
- b) The vertical precision of WSE measurements averaged over an area of 1 km² (lake, reservoir, wetland, and river) elevations must not exceed 10 cm (1-sigma)
- c) The river slopes for river widths > 100 m must be measured to an accuracy of 10 μ rad (1 cm/km) after averaging no more than 10 km downstream the river.

The table below shows the science traceability matrix for hydrology, mapping the science objectives into science requirements, and in turn into instrument functional requirements.

Science Objectives	Scientific Measurement Requirements	Instrument Functional Requirements
<ul style="list-style-type: none"> • Determine surface water storage change and discharge to predict the land surface branch of the global hydrologic cycle. • Measure flood hydraulics. • Assess the role of fresh water storage as a regulator of biogeochemical cycles such as carbon and nutrients. • Estimate global storage change in terrestrial surface water bodies and global change in river discharge at sub-monthly, seasonal, and annual time scales 	<ul style="list-style-type: none"> • Global monitoring of storage change by measuring changes in water body height and spatial extent with time for all bodies whose surface area exceeds (250m)² and rivers whose width exceeds 100 m. • Estimation of water mask extent to within 15% of body area. • Derivation of river discharge from measurements of slope and spatial extent within a hydrodynamic model assimilation. • Revisit time ~2 weeks in the tropics and less than 1 week in the Arctic (including ascending and descending orbits). 	<p style="text-align: center;"><u>Ka-band Interferometer:</u></p> <ul style="list-style-type: none"> • Height measurement for water bodies and rivers. • Slope measurement relative to surrounding topography. • Spatial resolution of 70 m postings or finer at the near-swath. • Provide above measurement accuracy over two swaths of 50 km each. <p style="text-align: center;"><u>POD Suite:</u></p> <ul style="list-style-type: none"> • Determine orbit.
	<ul style="list-style-type: none"> • 42 month baseline operation for capturing 3 seasonal cycles and interannual variability 	<ul style="list-style-type: none"> • 42 month reliability

4.4 KaRIn Overview

KaRIn is a synthetic aperture (“imaging”) radar interferometer operating at Ka-band (35.75 GHz center frequency). The key system parameters are shown in the table below. The antenna subsystem is formed by two 5 m long and ~0.3 m wide deployable antennas on opposite ends of a 10 m deployable boom (which forms the interferometric baseline). The antenna employs printed reflectarray technology, which is basically a flat panel with etched elements on its surface providing the phase change required to collimate the beam, emulating a parabolic

reflector. This architecture enables stowage of the antenna to fit inside the launcher fairing, while structurally being low mass, to minimize the tip-mass for best overall baseline system stiffness.

Table 1. KaRIn Key System Parameters

Parameter	Value
Center frequency	35.75 GHz
TX Bandwidth	200 MHz
TX Pulse length	4.5 us
Pulse Repetition Frequency (average)	2 x 4420 Hz
Peak Transmit Power (EOL)	1,500 W
Physical Baseline Length	10 m
Antenna size	5 m x 0.25 m
Boresight Look Angle	+/- 2.7 deg
Polarization, Right Swath	VV
Polarization, Left Swath	HH

One of the antennas transmits, and both receive the radar echoes. The interferometer is a dual-swath system, alternatively illuminating the left and right swaths on each side of the nadir track (see figure below). This is accomplished by an offset dual-feed design operating with orthogonal linear polarizations (V and H polarizations), which enables each reflectarray antenna to generate two separate beams scanned ± 2.7 deg off boresight, one at each polarization.

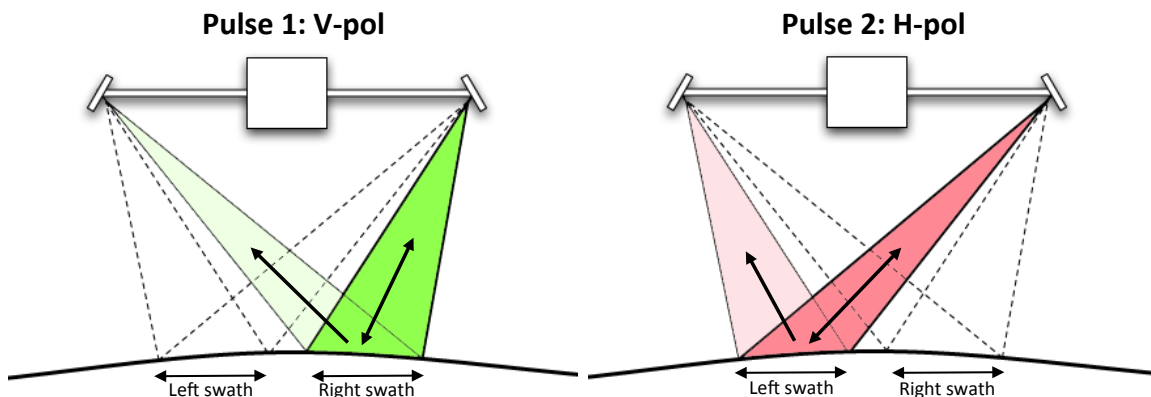


Figure 4. The timing sequence is formed by two pulses, interleaving left and right swaths. The left swath is imaged by a single pulse from the transmit antenna, followed by a pulse illuminating the right swath. The nominal pulse repeat frequency (PRF) is 4.42 KHz per swath, for a total transmit repetition frequency (TRF) of 8.84 KHz.

The instrument’s spatial resolution in the direction parallel to the baseline direction (across the swath) is determined by the system bandwidth. With a 200 MHz transmit bandwidth, KaRIn would achieve ground resolutions in the cross-track direction ranging from approximately 70 m (at the near edge of the swath) down to 10 m (at the far end of the swath). As a synthetic aperture radar (SAR), the spatial resolution in the along-track direction (perpendicular to the baseline

direction), is given by the length of the synthetic aperture that can be realized. The highest theoretical resolution that can be obtained is approximately given by half the antenna length, or 2.5 m. In practice, the resolution is determined by a combination of factors, including the antenna pattern, the azimuth bandwidth that is processed to achieve a desired ambiguity level (“contamination” level from adjacent pixels), and other design parameters, which make it closer to 2.63 m. In addition, the maximum resolution that can be synthesized would be in practice limited by the decorrelation time of the scene (the time for which the phase of the returns from a resolution cell is considered to be coherent, also referred to as coherence time). The decorrelation time needs to be longer than the integration time (the time of the synthesized aperture) in order to achieve azimuth resolutions close to the theoretical limit. Note that the decorrelation time only affects the achievable resolution and does not impact the accuracy of the interferometric measurement since, for a given swath, every echo pair observes the same realization of speckle noise.

KaRIn’s high resolution imposes stringent constraints on the onboard storage and the downlink needs of the overall observatory. In order to reduce the output data rates and downlink volumes to fit within existing capabilities, KaRIn’s digital subsystem performs onboard processing, which is discussed in the next section.

4.5 KaRIn Onboard processing overview

The KaRIn Onboard Processor (OBP) is integral to the overall functionality of the KaRIn system, performing a double duty for both surface water and ocean measurements:

- 1) Over land, the instrument performs standard SAR compression techniques: pre-summing by a factor of 2 (nominally; two pre-summing factors are implemented which can be selected by ground command), resampling to the system bandwidth (200 MHz), and Block Floating Point Quantization (BFPQ) to 3 bits. The allocated output data rate for this mode is 360 Mbps.
- 2) Over the oceans, the instrument processes the incoming radar signal from an interferometric channel pair and generates a complex interferogram, as well as amplitude images for each channel, to be downlinked to the ground. The amplitude images for each channel enable estimation of the interferometric coherence on the ground. The onboard processor also performs multi-look averaging to decrease the data rate over the oceans before downlink. The OBP averages down to a resolution of 1 km² at 1 km posting, achieving a reduction factor in the data rate in excess of two orders of magnitude. The allocated output data rate for this mode is 2.7 Mbps.

At a high-level, the ocean algorithm (shown in the figure below) implements the following steps for each swath: a pair of received echoes (one echo from each antenna) are first processed independently; each is range compressed (ie. a matched filter via an FFT in frequency domain), followed by sinc interpolation to co-register in time the echoes from both receive channels, and a range-adaptive spectral filtering to approximately flatten the phase and remove the non-common portion of the two spectra to minimize the coherence loss. This is accomplished by a two-step process: first, an opposite sign phase ramp is applied to each of the interferometric channels in the time domain to induce a frequency spectrum shift that aligns the spectral components of the interferometric channel pair (i.e. flattens the interferometric phase). Second, a FIR filtering is performed to remove the non-overlapping parts between channel spectra. This range-dependent filtering is implemented with a bank of filters, which are slowly adjusted along the orbit to account for mean sea surface (MSS) variations. The algorithm then takes 9 range-compressed

lines, which are corner-turned and stored in memory since the next steps operate in the azimuth direction, processing one range gate at a time. The azimuth processing implements a squinted unfocused azimuth SAR processing for each collection of range gates from a series of consecutive pulses. This effectively divides the real-aperture azimuth beamwidth into 9 separate sub-beams to maintain the number of looks, for an unfocused azimuth resolution of ~ 250 m. This step is accomplished by performing the complex multiplication of the 9 azimuth samples by 9 separate phase ramps that take into account the Doppler centroid (separately estimated by the algorithm, so as to relax what would otherwise be very stringent S/C pointing control or real-time knowledge requirements), to shift the Doppler spectrum to 9 different Doppler angles. The next stage in the algorithm is to compute the complex interferogram for each one of the 9 output beams by multiplying one channel by the conjugate of the other, as well as the amplitude images for each channel by multiplying each channel by its own complex conjugate. Finally, the algorithm performs multi-look averaging of each interferogram and the images power to achieve the required 1 km (along-track) x 1 km (cross-track) resolution.

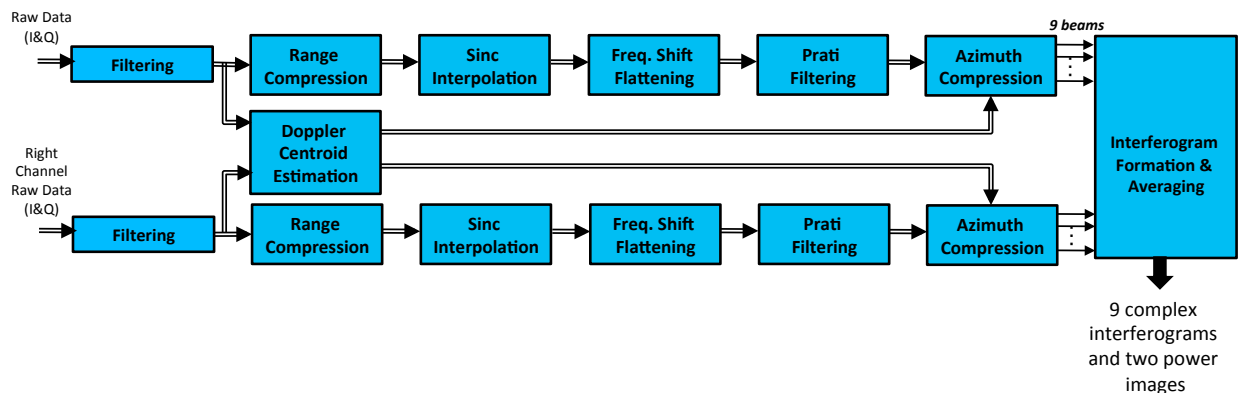


Figure 5. Basic steps of the KaRIn Onboard Processor for the oceans.

A raw data mode is also implemented in the KaRIn instrument, which can be selected by ground command, to enable the collection of raw Analog-to-Digital Converter (ADC) samples of the receive echoes for a continuous set of 2,800 pulses per swath (corresponding to a time duration of roughly 0.6 sec, or 4 km along-track). Ocean onboard processed data is also generated concurrently for downlink. The short duration of the raw-data mode is related to the fact that the instantaneous raw data rate is very high (close to 7 Gbps); since the rest of the Flight System is not able to cope with such data rate, it is buffered inside the instrument and output to the Solid State Recorded (SSR) at a not-to-exceed rate of 360 Mbps. The main objectives of this data collection mode includes support of the cal/val activities related to the OBP (allowing for a direct comparison of the onboard processed data against the raw data being processed on the ground), as well as to support diagnose of on-flight anomalies. As such, it is conceived as an engineering data collection mode, and does not serve any direct science objectives.

5 OCEAN MEASUREMENT REQUIREMENTS AND ERROR BUDGET

As indicated in the previous section, the ocean requirements are formulated for two separate wavenumber regions, which would be fulfilled by a different combination of payload instruments. We first discuss the measurement requirement and error budget for ocean wavelengths below 1,000 km, followed by the error budget for the other wavenumbers.

5.1 Error budget for ocean wavelengths < 1,000 km

We define the Sea Surface Height (SSH) error spectrum, $E_{SSH}(f)$, as a function of the spatial frequency f (i.e., $f=1/\text{ocean wavelength}=1/\lambda$) (the spatial frequency is the same as the term of "wave-number" used in some oceanographic literature). The key oceanographic requirement for the SSH is thus specified as the error spectrum defined in the SWOT Science Requirement Document in units of $\text{cm}^2/\text{cycle}/\text{km}$ as:

$$E_{SSH}(f) = 2 + 1.25 \cdot 10^{-3} f^{-2}, \quad 15 \text{ km} < \lambda < 1,000 \text{ km}$$

The error spectrum is defined as an "ensemble average" (1-sigma) requirement, such that the expected SSH error variance in a wavelength interval $[\lambda_{min}, \lambda_{max}]$ is given by the integral of $E_{SSH}(f)$:

$$\langle (\delta h)^2 \rangle = \int_{1/\lambda_{max}}^{1/\lambda_{min}} E_{SSH}(f) df$$

The total SSH error science allocation over $\lambda = [15, 1,000 \text{ km}]$ integrates to 1.168 cm. Figure 6 shows the error spectrum both for the science baseline and threshold requirements, where the latter one is defined as increasing the noise level from 2 $\text{cm}^2/\text{cycle}/\text{km}$ to 4 $\text{cm}^2/\text{cycle}/\text{km}$ in the equation above. Also shown in the figure are the global SSH signals in different percentiles estimated from Jason measurements (and extrapolated for wavelengths below ~ 100 km).

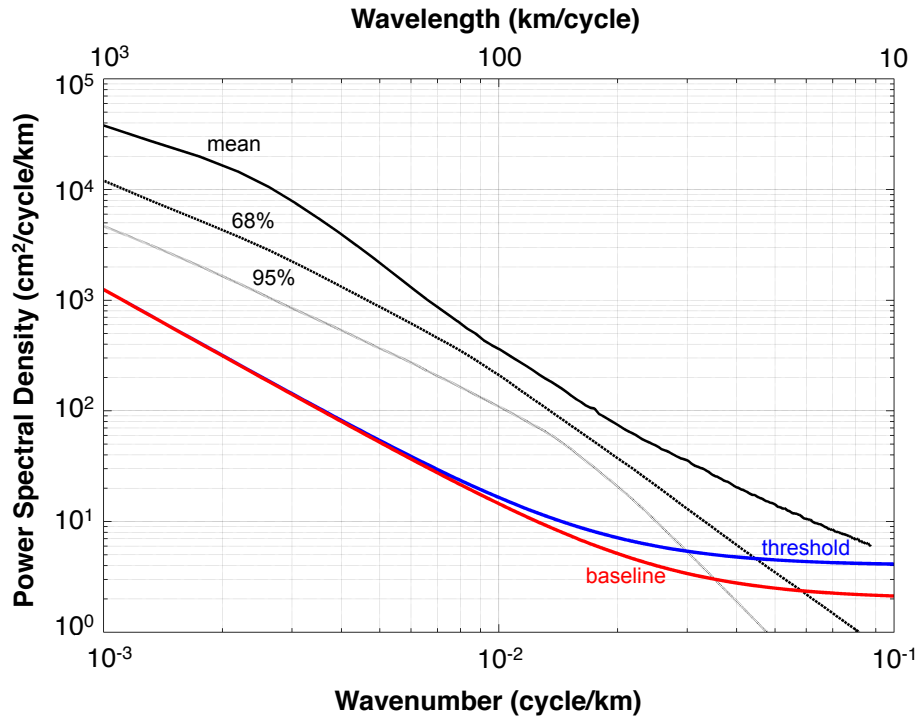


Figure 6. SSH error spectrum requirement (red curve) as a function of wavenumber. Shown, for reference is the global mean SSH spectrum estimated from the Jason-1 and Jason-2 observations (thick black line), the lower boundary of 68% of the spectral values (the upper gray dotted line), and the lower boundary of 95% of the spectral values (the lower gray dotted line). The intersections of the two dotted lines with the error spectrum at ~ 15 (68%) and ~ 25 km (95%) determine the resolving capabilities of the SWOT measurement. Also shown for reference is the threshold requirement, which follows the same expression as the baseline requirement but with a noise floor of 4 $\text{cm}^2/\text{cy}/\text{km}$.

5.1.1 Measurement sampling

In order to translate the SSH spectral requirement into the payload's overall performance requirement, we need to first consider how to derive an instrument sampling error spectrum from the ocean wavelength error spectrum. The conversion of spatial frequency f into sampling frequency f_s for any given payload instrument is given by the amount of time that it takes to cover a given wavelength λ , which is simply governed by the spacecraft ground speed. While the ground velocity changes slightly depending on the satellite's position along the orbit, we hereafter assume a constant (nominal) ground velocity of $v_g = 6.5$ km/s (the sensitivity of this parameter to the orbit altitude is not significant). Therefore, the relationship between spatial frequency and instrument sampling frequency is simply given by $f_s = v_g \cdot f = v_g / \lambda$. Therefore, the 1 km ocean wavelength corresponds to 6.5 Hz, and the 1,000 km wavelength corresponds to 0.0065 Hz. The latter value corresponds to a sampling time of 153.8 sec, or 2.6 min. It is worth noting that this period of time corresponds to the time where the Flight System, and KaRIn in particular, needs to remain sufficiently stable to meet the overall SSH error spectrum.

To resolve a minimum wavelength of 15 km, the data must be at least critically (Nyquist) sampled at 7.5 km. The SSH error spectrum requirement is specified as a single-sided along track spectrum after filtering the cross-track with an ideal square filter to 15 km wavelengths, and for the swath-average performance (from 10 km to 60 km). In this document, we will use the KaRIn standard deviation of the height error, σ_{cm} , for 1 km² averaged pixels as the basis for most formulations. The corresponding single-sided spectral density of the random noise, N_{random} , can be derived as:

$$N_{random} = 2 \cdot \frac{\sigma_{cm}^2}{\left(\frac{1cy}{km}\right)^2} \cdot \left(\frac{2}{\lambda_{min}}\right) \approx 0.267 \cdot \sigma_{cm}^2 \quad [cm^2/cy/km]$$

Note that not filtering above 15 km would mean that the noise spectral density would increase by a factor of $\lambda_{min} / 2 = 7.5$. It is also worth noting that the along-track averaging has no impact on the spectral density of the white noise in along-track. In forming a pixel of 7.5 km in along-track, its variance is reduced because one has effectively filtered in the along-track spectrum all frequencies that are above the Nyquist frequency corresponding to the 7.5 km; however, it has not changed the spectral density (and therefore it has not relevance with respect to the SSH spectral requirement). Therefore, the along-track averaging is only important if one is interested in finding the variance that a given pixel size would have, as it determines up to what frequency one should integrate the noise density (obviously, larger pixel sizes would exhibit less variance due to the filtering of the random noise). The difference in the cross-track direction is that the variance in the cross-track direction is the basis to form the white noise density that would then appear when one takes an along track spectrum. Therefore, in cross-track, averaging (or filtering) does have the ability to change the white noise density in the along-track. And it is only in cross-track that the pixel needs to be averaged to 7.5 km (consistent with resolving 15 km min wavelength) to assess against the SSH requirement.

5.1.2 Minimum wavelength and aliasing considerations

An additional consideration arises regarding the minimum wavelength. While the science performance requirement is specified down to 15 km wavelength, the effective maximum wavelength requirement needs to extend to at least half the sampling frequency; for a 2 km posting requirement, it needs to extend to at least 1/4 cy/km. Currently, the OBP produces 1 km²

pixels, posted every 1 km, with high frequency (>1 cy/km) errors being filtered in the process of obtaining the 1 km^2 pixels. This sampling introduces aliasing of frequencies above $1/2$ cy/km back into lower ones, as illustrated in the figure below. These aliased components cannot be removed later in processing; in order to be able to filter them, the posting would need to meet Nyquist for the pixel size, ie. a posting of 500 m for a 1 km^2 averaged pixel, which is not possible to implement due to the impact on the data rate, as it would roughly increase by a factor of four. It is thus crucial that no significant high frequency components appear in the region of $1/2$ cy/km to 1 cy/km (eg. errors associated to disturbances or other effects), to protect the measurement at wavelengths lower than 15 km. In order to achieve this, in what follows, we will extend the requirement as a PSD through 1 cy/km, which correspond to a sampling frequency of 6.5 Hz (0.15 seconds). In practical terms, this is mainly relevant to bound systematic errors, although the random noise component is also filtered in the same way, with a -3dB point at 1 cy/km.

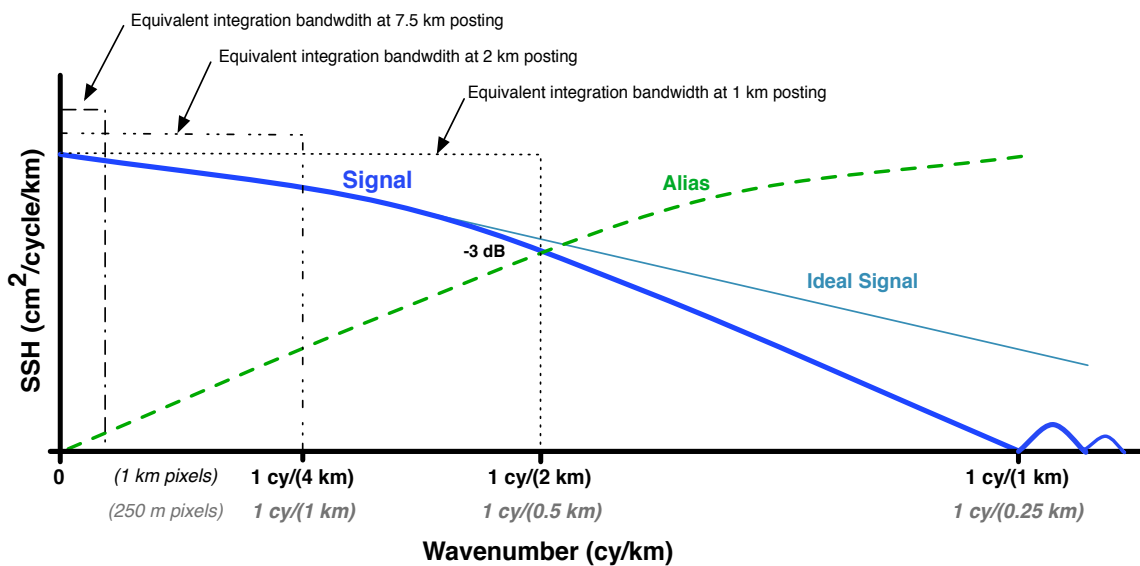


Figure 7. Illustration of high-frequency errors for different posting resolutions.

In addition, it is worth noting that the filtering that is implemented onboard for the 1 km^2 pixels also has the effect of tapering the signal in a spectral sense; an ideal rectangular window would result in a sinc function in frequency with a null right at 1 cy/km, and a -3dB taper at $1/2$ cy/km. The tapering reduces with longer wavelengths, and is negligible (< 0.1 dB) at $1/15$ cy/km, so it will not distort the spectrum of the SSH for the required range of wavelengths. As discussed later in more detail, the 1 km^2 pixel is filtered by a different averaging window to eliminate height biases that would otherwise appear, among other reasons, due to the presence of ocean waves.

It is also worth noting that implementing an increased pixel resolution of $250 \text{ m} \times 250 \text{ m}$ with a posting of 250 m would alias frequencies within the range of $1/0.5$ cy/km to $1/0.25$ cy/km, corresponding to sampling frequencies of 13 Hz to 26 Hz, which could not be filtered on the ground. To avoid having disturbances and other source of high frequency errors potentially contaminating significantly the measurements, a preferable alternative would be to consider $500 \text{ m} \times 500 \text{ m}$ pixels at a posting of 250 m , while would enable ground filtering in that range of frequencies while requiring the same increase in data rate as for $250 \text{ m} \times 250 \text{ m}$ pixels.

5.1.3 Error budget top-level break-down

A typical approach to establishing the interferometric error budget is to allocate a budget for each error source (systematic, random, and media) at one or more points along the swath, where the root-square sum (RSS) of all the errors satisfies the overall height accuracy requirement. However, it is important to note that for SWOT, the science requirements define the error as a swath-average performance requirement, rather than specifying the performance at some point in the swath. Also, the spectral form of the science requirements effectively specifies the error requirement over different time scales (or, equivalently, spatial scales), as given by the SSH spectral power density error spectrum. Therefore, the allocation rationale that will be applied throughout the ocean error budget is as follows:

- 1) We first define that the direct sum of all spectral errors (random, systematic, media, and POD error spectra), shall meet the required science error envelope, $E_{SSH}(f)$.
- 2) We define the KaRIn instrument standard deviation of the random error allocation as 2.5 cm, defined as a swath-average for an average 1 km² pixel, and for all wavelengths. This translates into a random error spectral density, $E_{random}(k) = 0.267 * (2.5)^2 \text{ cm}^2/\text{km}/\text{cycle} = 1.67 \text{ cm}^2/\text{km}/\text{cycle}$. By subtracting the random error from the overall science requirement, one is left with the residual error that can then be allocated to all the remaining errors (systematic, media, and POD).
- 3) We bound all the media, and POD errors by using error spectral envelopes. By subtracting all these spectral envelopes from the previous residual, one obtains the residual error that will be allocated to the systematic errors, $E_{SYS}(k)$:

$$E_{SYS}(k) = E_{SSH}(k) - E_{random}(k) - E_{wet\ tropo}(k) - E_{dry\ tropo}(k) - E_{SSB}(k) - E_{ionosphere}(k) - E_{POD}(k)$$

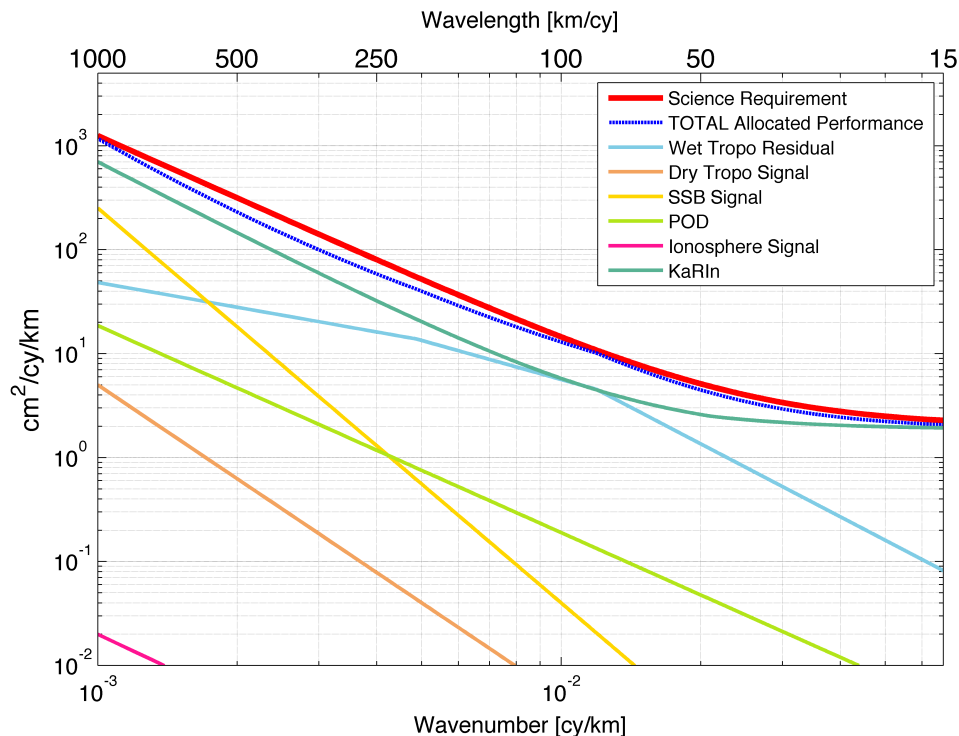


Figure 8. Break-down of the overall SSH error budget in spectral form for wavelengths < 1,000km. This includes all propagation, media, orbit, and the sum of all KaRIn errors.

The sub-allocations of the systematic error budget into its different components (roll, phase, baseline dilation, and system timing drifts), and how they flow into the different mission elements, are discussed in detail in the following sections.

The KaRIn allocation, including all random and systematic errors is given by:

$$E_{KaRIn}(f) = 1.89 + 3.6153 \cdot 10^{-4} f^{-2} + 1.5442 \cdot 10^{-5} f^{-2.5}, \quad f = [1 \text{ km}, 1,000 \text{ km}]$$

The figure below shows the allocation as well as the breakdown into its components: systematic errors, random noise, and the gyro knowledge error.

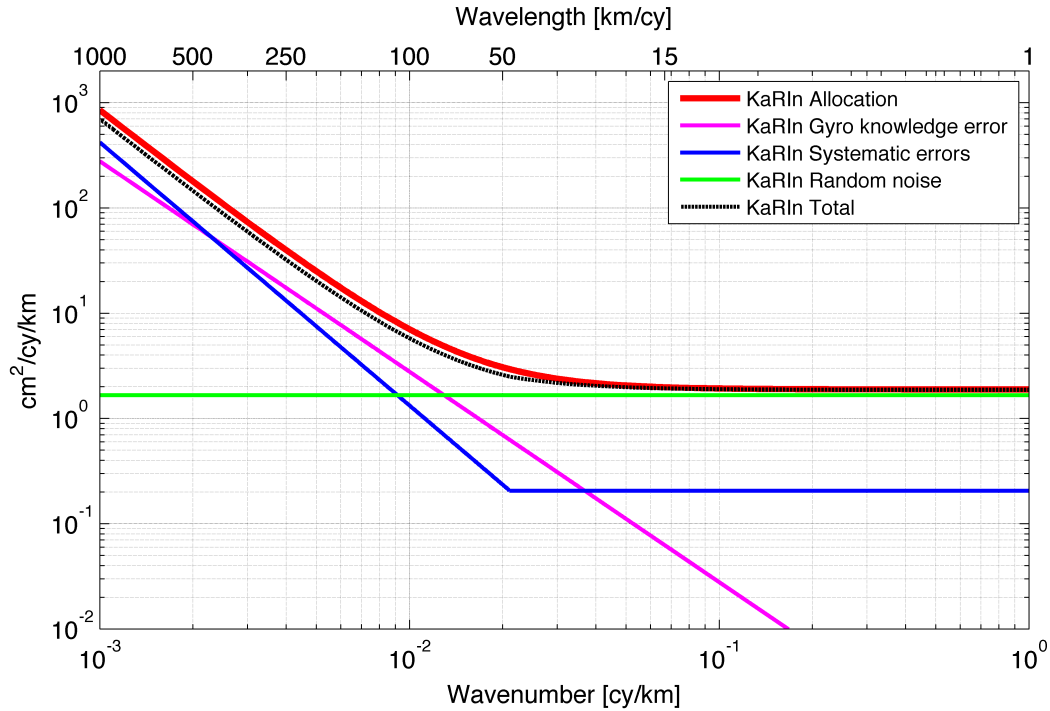


Figure 9. Break-down of the KaRIn errors in spectral form for wavelengths < 1,000 km.

Table 2. Top-level break down of the SSH science requirement for ocean wavelengths < 1,000 km in an integrated form across two wavelength ranges.

Ocean Error Component < 1,000 km	15-1,000 km [cm]	Comments
Ionosphere signal	0.004	Integrated signal
Sea-State Bias signal	0.301	Integrated signal
Dry Troposphere signal	0.050	Integrated signal
Wet Troposphere Residual	0.426	After cross-track radiometer correction
Orbit Radial Component	0.140	Integrated signal

KaRIn Random errors	0.352	Integrated signal
KaRIn Systematic errors	0.798	Includes gyro errors
Algorithm errors	0.219	Processing/correction errors
Total Allocated Error (RSS)	1.049	Total error, as allocated
Unallocated margin (RSS/SUM)	0.514 / 0.119	
Total (RSS) Sea Surface Height Error	1.168	Requirement

A breakdown of the total SSH error budget in its allocations as a fraction of the total SSH spectral requirement is presented in the figure below. It is worth noting that the unallocated margin is not constant throughout the entire wavelength region; for most wavelengths, the margins is larger than 10%, but it is slightly lower in a narrow region around 80 km due to the fact that the contribution of the wet tropo error peaks within that interval.

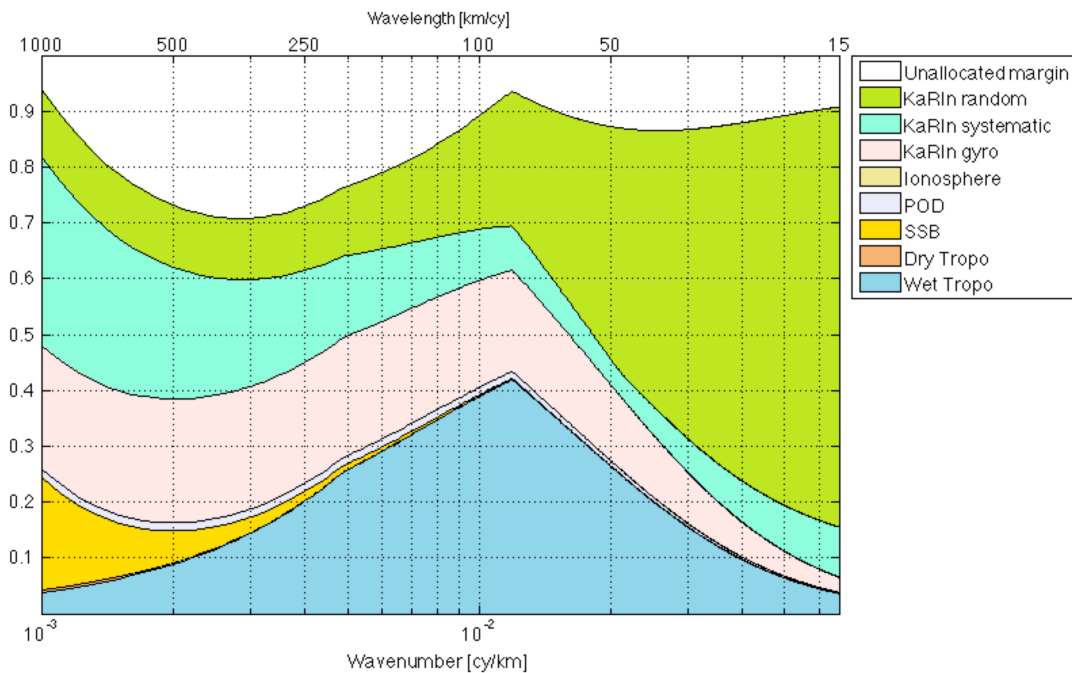


Figure 10. Stack-up of the allocations as a fraction of the total SSH requirement as a function of wavenumber.

5.2 Error budget for ocean wavelengths > 1,000 km

As previously mentioned, the measurement of the SSH spectral region above 1,000 km is performed by the nadir altimeter. The error budget is thus consistent with the break-down of the Jason-2 (and Jason-3) GDR product, as shown in the table below.

Ocean Error Component > 1,000 km	Error [cm]
Ionosphere signal	0.5
Sea-State Bias residual (1% of SWH)	2
Dry Troposphere signal	0.7
Wet Troposphere residual	1.2
Orbit Radial RMS Component	1.6
Altimeter Noise	1.7
Total (RSS) Sea Surface Height Error	3.4

It is worth noting that, contrary to the error budget for SSH<1000 km, the nadir altimeter requires well-established model corrections to meet the media error allocations.

5.3 OCEAN MEDIA/WAVE ERROR REQUIREMENTS

5.3.1 Sea-State Bias

The EM or sea-state bias (SSB) is a height bias that is introduced due to the varying reflectivity of wave crests and troughs, with wave troughs being better radar reflectors than wave crests at nadir. The mean scattering level is therefore shifted towards the wave troughs with respect to the true mean sea level, and for a standard altimeter, the range between the altimeter and the sea surface is overestimated. Also, the skewed wave height distribution with a median shifted towards wave troughs introduces another bias in measured sea level, which is referred to as skewness bias. Historically, the EM bias has usually been expressed as a fraction of the SWH, which is defined as the average height of the 1/3 highest waves observed. Airborne observations carried out by Walsh et al. shows that the bias values are around 1% of the SWH at Ka-band, around 3% at Ku-band, and approximately 4-5% at C-band. While corrections can be calculated from models, we envelope the full SSB spectrum signal derived using the four-parameter BM4 parametric model for Ka-band, which is given by [6][7]:

$$SSB(U, SWH) = (-0.021 - 0.0035 \cdot U + 0.00014 \cdot U^2 + 0.0027 \cdot SWH) \cdot SWH$$

Where U is the wind speed, and SWH is the Significant Wave Height, which is defined traditionally as the mean wave height (trough to crest) of the highest third of the waves. This could be considered a rather pessimistic upper bound of the error, since it is not assumed that that models (or retrieval estimates using Nadir Altimeter measurements) are used to reduce the error, as it is done for the Jason series of altimeters (reducing it from roughly 3% to 1% of the SWH). We do not consider a residual because for KaRIn the incidence angle dependence of the SSB (over the swath) does not have the Jason heritage. A global analysis of the SSB based on the above model has been used to derive an envelope allocation of the SSB error spectrum, given by:

$$E_{SSB}(f) = 10^{-9} f^{-3.8} [cm^2/cy/km]$$

The integrated SSH error for wavelengths between 1 and 1,000 km for the derived envelope is 0.301 cm.

5.3.2 Ionosphere

The ionosphere is a dispersive medium affecting the signal delay approximately proportional to the square of the radar wavelength, and includes long-wavelength effects due to variations in the total number of electrons (total electron content, TEC, where 10^{16} electrons/m²= 1 TEC unit, or TECU) present along the radar path, as well as large to medium scale disturbances (traveling ionospheric disturbances, TIDs) and short wavelength effects due to small-scale TIDs and turbulences at the base of the ionosphere. The ionosphere introduces a group delay (range error) that is given by:

$$dh = \frac{40.3}{f^2} \int_0^H ds N_0(s)$$

where $N_0(s)$ is the electron density (in units of #/m³), and f is the radar frequency. At the KaRIn frequency of 35.75 GHz, for a minimum solar cycle (20 TECU), the range error is roughly 7 mm, and for a near maximum solar cycle (~100 TECU) the range error is 33 mm. We have used the Ionex model to derive an envelope for the ionospheric error spectrum over the global oceans, which is given by:

$$E_{ionosphere}(f) = 10^{-8} f^{-2.1} [cm^2/cy/km]$$

The integrated SSH error for wavelengths between 1 and 1,000 km for the derived envelope is 0.004 cm.

5.3.3 Dry troposphere

The propagation velocity of an electromagnetic signal is slowed down by the "dry" gasses and the quantity of water vapor in the Earth's troposphere. The "dry" gas contribution is nearly constant and produces height errors of approximately -2.3 m. The gases in the troposphere contribute to the index of refraction. Its contribution depends on density and temperature. When hydrostatic equilibrium and the ideal gas law are assumed, the vertically integrated range delay is a function only of the surface pressure. The dry meteorological tropospheric range correction is equal to the surface pressure multiplied by -2.27 mm/mb. There is no straight forward way of measuring the nadir surface pressure from a satellite, so it is usually determined from model assimilated weather data from the European Center for Medium Range Weather Forecasting (ECMWF). The uncertainty on the dry tropospheric correction as an overall RMS is about 0.7 cm. We envelope the dry troposphere error spectrum from the results obtained from the Chelton model that is used to correct the Jason altimeter measurements, which is given by:

$$\text{Dry Tropo Correction} = -2.277 * P_{\text{atm}} * (1 + 0.0026 \cdot \cos(2 \cdot \text{latitude})) [mm]$$

where P_{atm} is surface atmospheric pressure in mbar, ϕ is latitude. This results in an envelope error spectrum given by:

$$E_{dry\ troposphere}(f) = 5 \cdot 10^{-9} \cdot f^{-3} [cm^2/cy/km]$$

The integrated SSH error for wavelengths between 1 and 1,000 km for the derived envelope is 0.05 cm.

5.3.4 Wet troposphere

While the spectral form of the wet tropospheric path delay is well known over the oceans from AMSR-E and Jason-1/2 measurements, the error of interest here is the residual to the corrections that the onboard radiometer would introduce. Let's first assume an isotropic 2D spectrum, (f_s ,

$f_c) = A_{2D}f^p$, where $f^2 = f_s^2 + f_c^2$. For cases where $p > 1$, the 1-D signal single-sided spectrum can be obtained by integrating the 2D spectrum in the cross track frequency dimension (note a factor of 4 arises from the fact that we only integrate the positive side, and that this is the single-sided spectrum).

$$S_{1D}(f_s) = 4 \int_0^\infty df_c A_{2D} f^{-p} = 2A_{2D} B\left(\frac{1}{2}, \frac{p-1}{2}\right) f_s^{-p+1}$$

where $B(x,y)$ is Euler's integral of the first kind (beta function). To derive the overall error spectrum, we consider a 2D slope of $p=8/3+1$, which is consistent with all available observations from AMRS-E and the Jason-1/2 AMRs for wavelengths > 100 km. This results in a 1-D wet tropo signal given by:

$$S_{wet\ tropo}(f) = 3.156 \cdot 10^{-5} f^{-8/3}, \lambda > 100\ km$$

Below 100 km, initial high-resolution measurements made by JPL's High Altitude MMIC Sounding Radiometer (HAMSR), indicate a slightly lower slope of -2.33, for a wet tropo signal given by:

$$S_{wet\ tropo}(f) = 1.4875 \cdot 10^{-4} f^{-2.33}, \lambda \leq 100\ km$$

Given the signal, the residual swath-average error for a nadir-looking radiometer is given by:

$$E_{wet\ tropo\ swath}(f) = 2 \int df_c S_{wet\ tropo}(f) (1 - sinc(2 C_{max} f_c))$$

where C_{max} corresponds to the maximum extent of the swath (60 km). For a single radiometer channel looking at nadir (such as for the Jason series of altimeter), the overall error over the swath would be then be sum of the contributions of the swath average error and the nadir radiometer error (including algorithm retrieval errors), ie:

$$E_{wet\ tropo\ nadir}(f) + E_{wet\ tropo\ swath}(f)$$

where the nadir error contribution is derived from analysis from models (MERRA, NCEP, and WRF), with an envelope given by:

$$E_{wet\ tropo\ nadir}(f) = \begin{cases} 9.5 \cdot 10^{-5} f^{-1.79}, & 10^{-3} \leq f < 0.0023 \\ 0.036 f^{-0.814}, & 0.0023 \leq f < 0.0683 \\ 0.32, & f \geq 0.0683 \end{cases}$$

which is shown in **Figure 11**. Since for scales shorter than 130 km, the total error exceeds the actual signal of the wet tropo (due to the fact that the radiometer nadir correction is not contributing information about the signal, but only adding as an uncorrelated signal), the retrieval needs to be filtered for frequencies below that point.

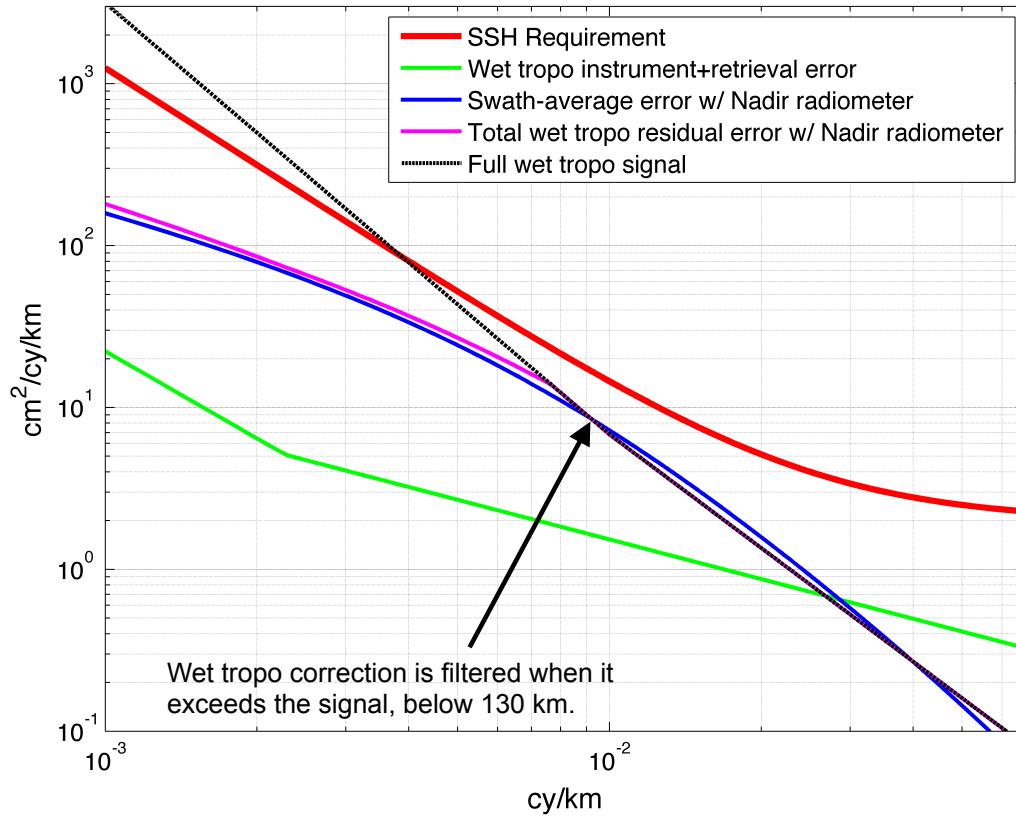


Figure 11. Break-down of the wet troposphere errors for wavelengths up to 1,000 km: a radiometer measurement + algorithm error, and the swath-average error that results from a nadir-based radiometer measurement.

The SRD, however, requires the implementation of a cross-track radiometer, which is a dual-channel (three-frequency) radiometer, where two measurements are collected at approximately +/- 40 km in the cross-track direction. This has the benefit of reducing the wet tropo swath average error and therefore the total wet tropo error contribution for wavelengths above 84 km, as shown in **Figure 12**. The final expression of the total wet tropo error for a cross-track radiometer implementation, including filtering the error for scales shorter than 84 km, can be approximated by three segments as follows:

$$E_{wet\ tropo\ total}(f) = \begin{cases} 0.205 f^{-0.7911}, & f < 0.0049\ cy/km \\ 0.0179 f^{-1.2492}, & 0.0049 \leq f < 0.0119 \\ 1.448 \cdot 10^{-4} f^{-2.33}, & f \geq 0.0119 \end{cases}$$

which is shown in **Figure 12**.

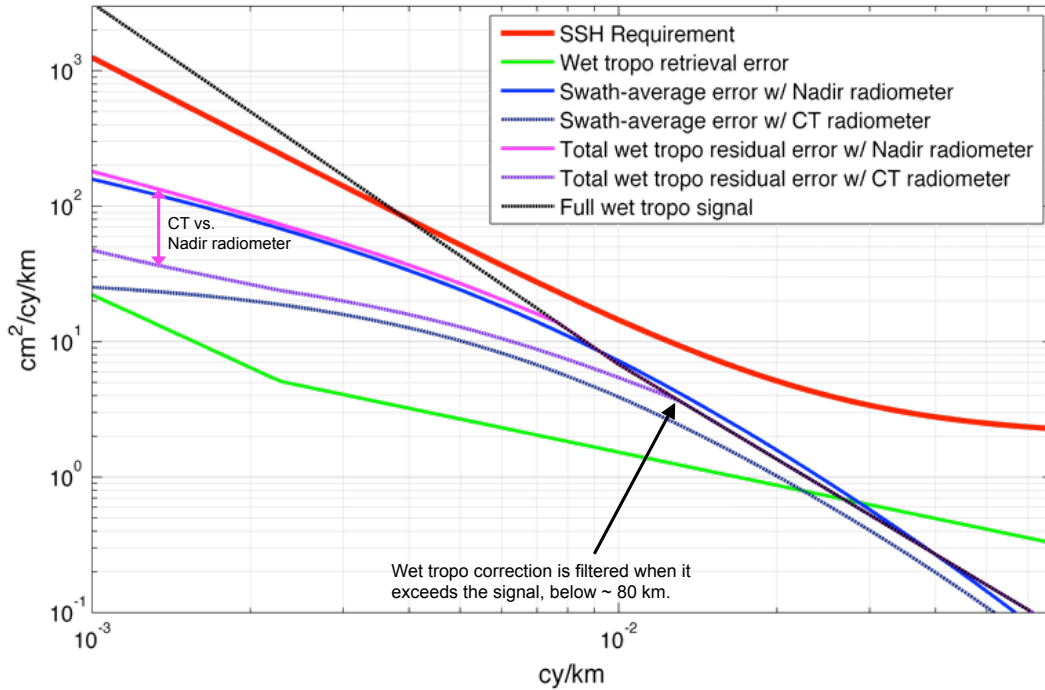


Figure 12. Wet-tropo total residual and error break-down that would be achieved for a cross-track radiometer measurement (two measurements performed at approximately +/- 40 km in the cross-track direction).

The effective impact of a cross-track radiometer is therefore to reduce the wet tropo error integrated from 15 km to 1,000 km wavelengths from 0.62 cm to 0.426 cm, particularly reducing the errors around the wavelength region between 125 and 150 km.

The sub-allocation of the wet tropo error between the radiometer instrument and algorithms was derived from simulations, as follows:

$$E_{wet\ tropo\ algorithm}(f) = 2 \cdot 10^{-7} f^{-2.6}, \quad f < 10^{-3} \text{ cm}^2/\text{cy}/\text{km}$$

$$E_{wet\ tropo\ instrument}(f) = \begin{cases} 0.0026f^{-1.192}, & 10^{-3} < f < 0.00228 \text{ cm}^2/\text{cy}/\text{km} \\ 0.0471f^{-0.7133}, & 0.00228 \leq f < 0.0682 \text{ cm}^2/\text{cy}/\text{km} \\ 0.32, & f \geq 0.0682 \text{ cm}^2/\text{cy}/\text{km} \end{cases}$$

The figure below shows the breakdown. As expected, the algorithm error dominates the large scales, since most of the systematic radiometer error sources appear on shorter scales.

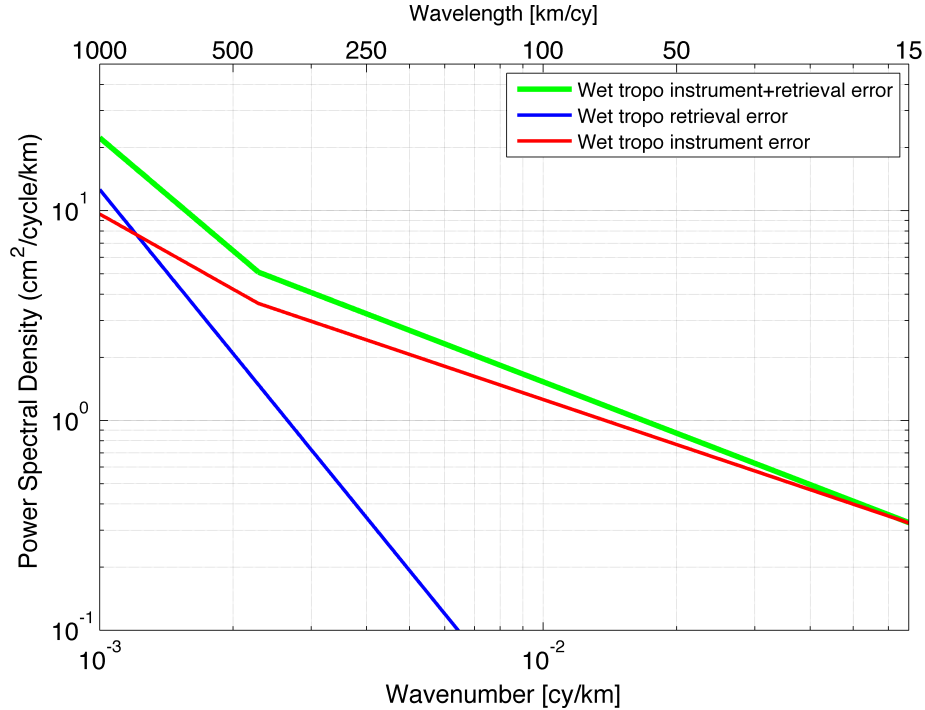


Figure 13. Breakdown of the wet tropo retrieval and instrument errors.

5.4 OCEAN RANDOM ERROR REQUIREMENTS

Random errors ultimately limit the accuracy of the height measurement that is required to resolve sub-mesoscale processes. An estimate of the interferometric phase error is obtained by the correlation of the complex returns from the two antennas, γ . For homogeneous targets, it is well known that the maximum likelihood estimator of the interferometric phase is given by:

$$\hat{\phi} = \tan^{-1} \left(\frac{\text{Im} \left(\sum_{k=1}^{N_L} v_1^k v_2^{*(k)} \right)}{\text{Re} \left(\sum_{k=1}^{N_L} v_1^k v_2^{*(k)} \right)} \right)$$

where N_L is the number of looks to be averaged, and v_1 and v_2 represent the voltage returns from the same resolution element received from each antenna. The MLE estimator is unbiased and for a large number of looks, as is the case for KaRIn, the phase variance follows the Crameo-Rao bound, which is given by:

$$\sigma_{\phi}^2 = \frac{1}{2N_L} \frac{1 - \gamma^2}{\gamma}$$

where N_L is the number of looks. This correlation coefficient is dependent on three key factors:

$$\gamma = \gamma_N \cdot \gamma_G \cdot \gamma_{\phi}$$

where γ_N is primarily driven by the system thermal noise; γ_G is the geometric correlation factor, due to the cross-track phase variations within each pixel (including co-registration errors of the two returns); and γ_{ϕ} is the angular (or volumetric) decorrelation. Note that there are additional decorrelation terms, such as those introduced by a common group delay, but they are very small and introduce negligible decorrelations. The main correlation terms are discussed hereafter; a high-level flow of its key components is shown in the figure below.

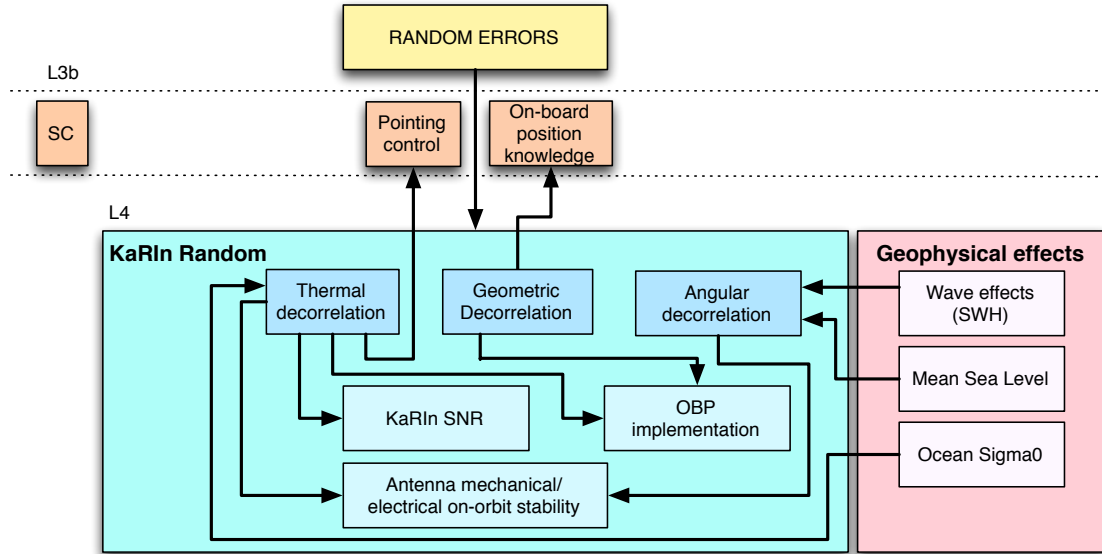


Figure 14. Conceptual high-level flow-down of the random errors to the key mission elements.

5.4.1 Ocean backscatter

The backscatter (σ^0 , or σ^0) of the ocean at Ka-band is derived from the Vandemark model[4], which parameterizes the backscatter as the following function of wind speed:

$$\sigma_{ka}^0 = \frac{|R(\theta)^2|}{mss'_{ka}} \sec^4(\theta) e^{-\frac{\tan^2 \theta}{mss'_{ka}}}$$

where θ is the incidence angle, $|R(\theta)^2|$ is the Fresnel reflectivity factor (with $|R(\theta)^2|=0.52$), and mss'_{ka} is a radar derived estimate of the surface wave slope variance (mss), which is parameterized as a function of the wind speed percentile, p , following the rayleigh global wind speed function derived by [5]:

$$mss'_{ka} = 0.019 \log \left(8.35 \sqrt{-\log(1-p)} \right)$$

The figure below shows the σ^0 over the KaRIn swath for three percentile cases, where the 68% is used hereafter in the SNR computations.

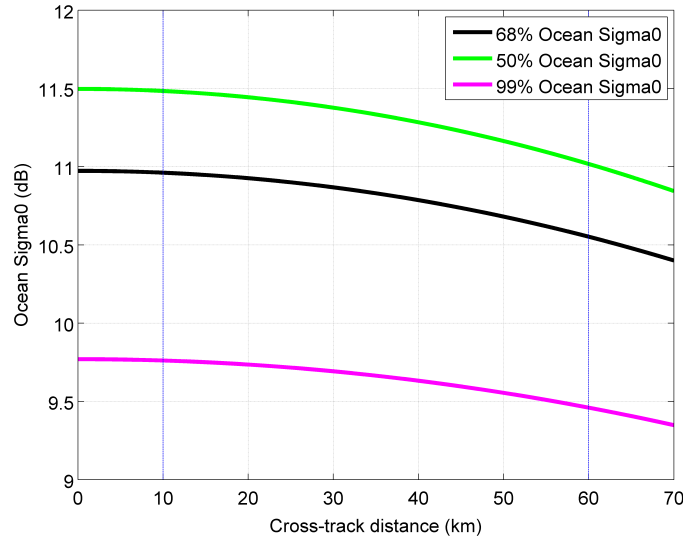


Figure 15. Ka-band Sigma0 as a function of cross-track distance for 68%, 50%, and 99% wind speeds.

The figures below show the global ocean wind speed PDF derived from a full year of Cross-Calibrated Multi-Platform (CCMP) ocean surface wind velocity L3.0 product and the resulting PDF of nadir sigma0's derived from these wind speeds.

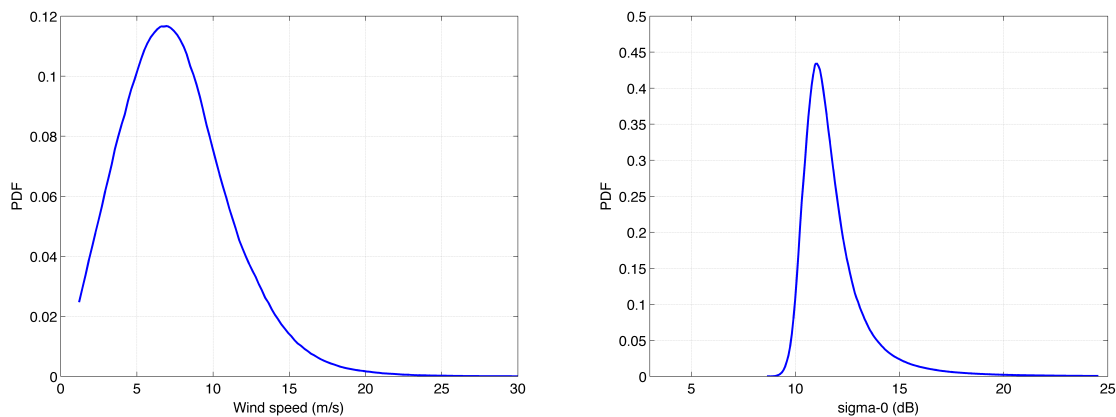


Figure 16. (left) PDF of the global ocean wind speeds from the CCMP product; the median value (50 percentile) corresponds to a wind speed of 7.4 m/s, and the 68 percentile to 8.9 m/s; (right) PDF of the sigma0's at nadir (0 deg incidence) derived from the ocean wind speeds using the Vandemark model described above. The 50 percentile corresponds to 11.5 dB, and the 68 percentile is 11 dB.

At a global scale, the ocean sigma0's predicted by the model are in agreement with the recent observations obtained by SARAL/AltiKa, as shown in the figure below.

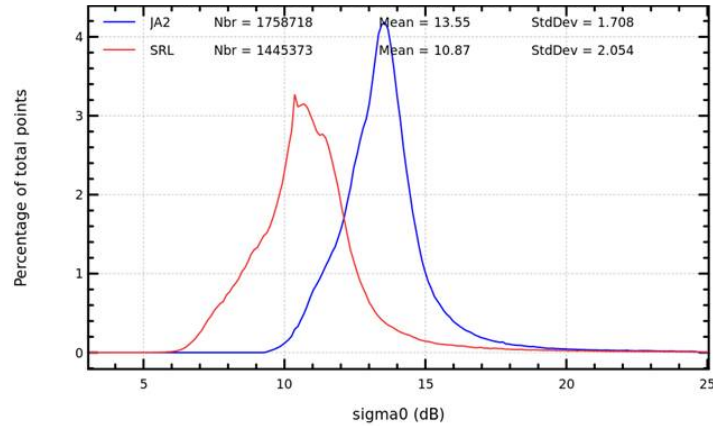


Figure 17. Histogram of the attenuation-corrected sigma0's (red) measurements taken by AltiKa from 06/27/2013 through 08/01/2013, and (blue) measured by Jason-2 (figure courtesy of CNES) for latitudes between -66 to +66 degrees. The mean ka-band sigma0 measurements is 10.87 dB.

5.4.2 Thermal decorrelation

As with any interferometric radar system, the thermal noise in the return signal cause the interferometric phase to contain random errors as described by the thermal correlation, γ_N , which includes the finite signal-to-noise (SNR) ratio available to the radar system, and other effects such as the degradation of the radar point-target response due the nominal antenna and variations along the orbit, Doppler centroid estimation errors, and pointing control errors. The thermal correlation factor, γ_N , taking into account all these factors, is given by:

$$\gamma_N = \frac{1}{1 + SNR^{-1}}$$

A margin of 5 dB is currently included in the KaRIn SNR.

5.4.3 Geometric Decorrelation

The main contributors to the geometric decorrelation are residual mis-registrations between the two images, errors in the spectral filtering implemented in the Onboard Processor, and spectral distortions in the Tx/Rx response of the system. In addition, dynamical geometric errors appear due to errors in the actual radial height (as a result of a combination of orbit errors, ocean variability, and onboard processing implementation choices in the reference surface that is used). These errors are briefly discussed hereafter.

Residual misregistration

Due to the fact that the two receivers are separated by the interferometric baseline, signals from the same point on the ground would arrive at different times at the receivers. This can be mitigated simply by adding a single delay between the channels so that the signals are perfectly corregistered for a given look angle. However, residual misregistration would still occur away from the selected direction. For KaRIn, the worst-case (far-swath) delay between antennas is:

$$\Delta r \approx B \sin(\theta)|_{\theta=\theta_{max}} = 0.72 \text{ m}$$

so that, if the two SAR images are co-registered at the swath center, the differential delay would be 0.36 m. Since this is close to being half the instrument's range resolution of 0.75 m,

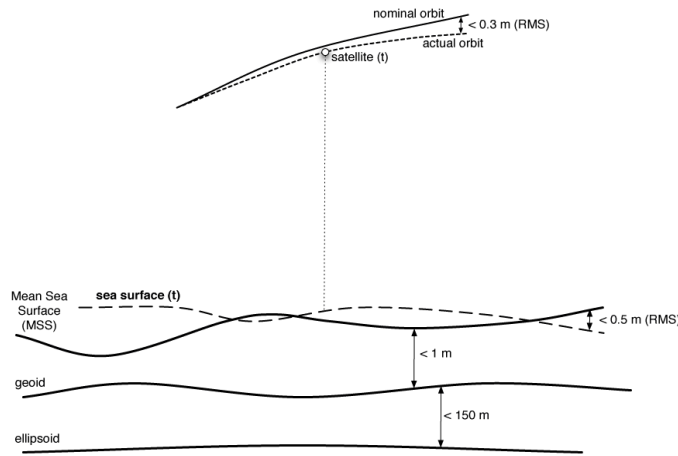


Figure 18. Sources of height errors: orbit errors, and sea surface deviations from the MSS reference surface.

will thus be to introduce an additional decorrelation term, thereby becoming a random error term; the correlation decreases as the look angle decreases, and therefore the error increases in the near swath. There are several sources of height errors that are relevant to this decorrelation: orbit errors, mean sea level, ocean variability, and tides. Some of these, such as orbit errors, have been mentioned in previous sections in relation to systematic errors. A key difference here is that for random errors we are not interested height error due to POD, but we are rather interested in establishing an upper bound to the total on-orbit height error, in order to limit the amount of decorrelation that can be tolerated.

The different height error sources are illustrated in Figure 18, and quantified in Table 3. First, there are errors associated to the platform's position. In nominal conditions, the radial orbit error corresponds to the maximum knowledge error with respect to the true in-flight orbit. This error is allocated 1 m, and would be achieved by a geodetic packet that DORIS provides to KaRIn on a periodic basis, using a similar capability to what is already implemented for the Nadir Altimeter.

Second, there are errors associated to the reference ground surface that is used as part of the onboard processing. Since the mean sea surface (MSS) is the reference surface implemented in the onboard processor for along-track height, the only residual height error (besides minor errors in the implementation of the MSS and a potential uncertainty of the MSS itself) is introduced by the deviation of the actual sea surface from this reference surface. This error can be decomposed into two major components: (1) the ocean variability, ie. the (tide-free) height variability above the MSS and ocean tides. The ocean variability is unknown on-orbit, but can certainly be bounded: the RMS of the sea level variability, relative to a one-year mean sea level is, at a global scale, much lower than 0.5 m: the Agulhas, Gulf Stream, and Kuroshio barely exceed 0.4 m, with a maximum of roughly 1.1 m found in a few extreme cases such as the Amazon Fan; and (2) Ocean tides, which naturally introduce an unknown on-orbit height error which have been assessed by Cherniawsky et al. [8] for the four principal tidal constituents (M2, K1, S2, O1). This enables us to bound the error, as shown in Table 3, to less than roughly 1.1 m RMS. Combining all the errors as a direct sum of all the RMS height error results in less than 4 m height error. In reality, this is a fairly pessimistic upper bound of the RMS height error, as it

differential range delays would cause severe decorrelation. To address this, the onboard processor implements a re-sampling stage. This is a standard technique for conventional SARs, where in order to perform channel registration, an interpolation algorithm using a finite interpolation kernel (e.g. sinc interpolation) is implemented, with the corresponding phase shift.

Radial height error

In addition, an unknown height error will affect the accuracy of the coregistration, introducing an additional misregistration between the two interferometric channels. The impact of an unknown height error

assumes that all the errors occur together. The decorrelation term associated to a 5 m height error is therefore part of the overall random error budget.

Table 3. Sub-allocation of all the height error sources for the ocean

Height Error Source	RMS	Max
Deviation from nominal orbit (allocated to S/C; fulfilled via specific DORIS packet)	< 1m	1 m
Implementation of MSS in KaRIn (allocated to KaRIn)	< 1.6 m	< 2.5 m
<i>Geophysical height errors:</i>		
Ocean Variability	< 0.5 m	< 1m
Tides	O1 < 0.20 m K1 < 0.31 m M2 < 0.44 m S2 < 0.15 m	O1 < 0.54 m K1 < 0.90 m M2 < 2.25 m S2 < 0.84 m
MSS Uncertainty	< 0.5 m	< 2.5 m
TOTAL SUM/RSS	< 5.0 m / <2.5 m	< 12 m / < 5m

Spectral filtering

A third source of this form of decorrelation is due to the fact that the interferometric phase is not constant for all the scatterers within a given resolution cell. This variation in the interferometric phase causes the total interferometric contribution from that cell to add slightly incoherently, thus reducing the signal correlation. However, for monochromatic signals, one can choose the wavelengths of the two channels to be such that the projected wave-vectors on the ground are identical for both channels [9]. In this case, the interferometric phase would be constant for all scatterers in the resolution cell, and the returns would add coherently. For a finite bandwidth signal, one can take the signal from both channels and shift the spectra in such a way that the appropriate wavelengths are multiplied together so that the phase variation over the resolution cell is canceled. The wave-number shift applies to SAR's, where the angular variation of the resolution cell in the azimuth direction is very small, so that iso-range and iso-phase lines are approximately aligned. However, this spectral shift means that noise is now brought into the processing bandwidth. In order to remove this additional noise, a low-pass filter is used so that only the parts of the spectra that overlap between both images contribute to the interferometric return. The penalty for this low-pass filter is a loss in resolution, but this loss is small and acceptable. Furthermore, due to the fact that the required shift and the amount of overlapping bandwidth of the two spectra depends on the incidence angle, if the filter response is made to be adaptive in the cross-track direction (which can be implemented by means of a bank of filters) to adjust for the changing frequency shift and bandwidth, then only the parts of the signal which correlate on the ground contribute to the return, and no additional noise is brought in due to the spectral shift. KaRIn's onboard processor implements this technique, and the wave-number shift is implemented by multiplying the spectra of the two signals with a range-dependent phase ramp in time, followed by a range-dependent finite impulse response (FIR) filtering of the signals.

This implementation approach virtually eliminates this source of decorrelation, and the residual loss of coherence is negligible.

Transmit/Receive Transfer Function Stability

Additional sources of decorrelation are associated to the stability of the transmit/receive function of the KaRIn instrument. The geometric correlation is given by:

$$\gamma_G = \frac{\int W_1(\omega - w)H_1(\omega)W_2^*(\omega + w)H_2^*(\omega)e^{-j\omega\tau_d}d\omega}{\sqrt{\int |W_1(\omega - w)H_1(\omega)|^2d\omega \int |W_2(\omega + w)H_2(\omega)|^2d\omega}}$$

where W_i are the range point target responses for each interferometric channel, and $H_i(\omega)$ are the (low-pass) Prati filters. It can be shown that there are two key contributors to the geometric correlation: the first one is related to the magnitude, and the second one to the phase. For KaRIn, specific requirements apply to linear and quadratic terms on the magnitude of the point target response, as well as due to ripple, which are derived from the magnitude term. In addition, a specific allocation for the standard deviation of the differential phase (to first order, is equivalent to a differential group delay, but in fact accounts for higher order non-linearities in the interferometric frequency response) is derived from the phase term.

5.4.4 Angular decorrelation

The angular decorrelation includes several effects. Primarily, the effect of the ocean waves introduces a volume scattering layer on the angle subtended by a range resolution cell, thereby introducing a volumetric decorrelation, as well as as a non-linear mixing of the ocean wavelengths termed the surf-board effect. In addition, and due to the fact that for a monostatic system such as KaRIn, the lines of constant range (iso-range lines), and the lines of constant phase (iso-phase lines), are only approximately aligned, the interferometric fringes vary over the range cell, even after the spectral shift described in the previous section, introducing an additional (yet small) amount of decorrelation. Each one of these effects is discussed below.

Volumetric (wave) decorrelation

The statistics of the ocean surface height can be modeled with the following probability function:

$$f_s(h) = \frac{1}{\sqrt{2\pi\sigma_h^2}} e^{-\frac{h^2}{2\sigma_h^2}}$$

where h is the topographic mean height at a given point, and σ_h is the ocean height standard deviation, related to the significant wave height as $\text{SWH}=\sigma_h$. The resulting correlation in the presence of a SWH is given approximately by:

$$\gamma_a \approx e^{-2\sigma_h^2\left(\frac{kB}{\rho\sin\theta_0}\right)^2}$$

where θ_0 is the look angle at the time of closest approach for a target at a given range distance r , and ρ is defined for spherical Earth as:

$$\rho = \frac{2(H + R_E)^2}{(H + 2HR_E + r^2)} \frac{r^2}{R_E}$$

where R_E is the Earth radius and H is the satellite altitude. The amount of decorrelation due only to the iso-range and iso-phase misalignment (corresponding to a $\text{SWH}=0$ m case) is negligible for KaRIn's swath. The main source of decorrelation is due to the presence of waves, which can be significant for large SWHs. The Science Requirement Document specifies a SWH of 2 m in

the spectral requirement, which is accounted for as part of the KaRIn random error budget.

Surf-board effect

The presence of surface gravity waves introduces an additional source of height error. As previously described, the reported sea surface height (SSH) is in fact a weighted average of the sampled SSH over an area of 1km^2 . Even though the spectral content of the wave spectra is concentrated at wavelengths well below 1 km, the measured height is a nonlinear function of the wave height, which introduces spectral components at wavelengths above 1 km that are not filtered and will become an additional source of height error. This source of error is termed “surf-board effect”, symbolizing the iso-range line being the “surf-board” that cuts across the ocean wave such that the points of intersection create the highest return, as illustrated in the figure below.

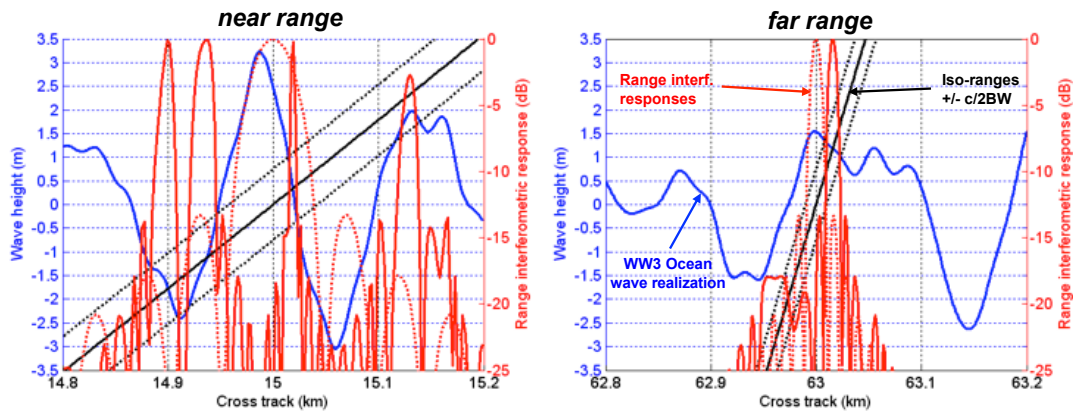


Figure 19. Illustration of the surf board effect in the cross track direction for simulated ocean waves realizations using WaveWath-3 for a SWH of 3 m (in blue), for two points in the swath (15 km and 63 km). The iso-range line (black) cuts the wave at various points, distorting the effective interferometric range response (solid red; nominal response in dashed red).

The height error increases in the near range inversely proportional to the sine of the incidence angle, and grows rapidly as a function of the SWH, starting to dominate in the near range over the thermal noise for SWH larger than 3 m, as shown in the figure below. This error is also accounted for in the KaRIn random error budget for SWH = 2 m, as specified in the Science Requirements Document, with a 1-sigma value of the swath-average height error of 2 mm.

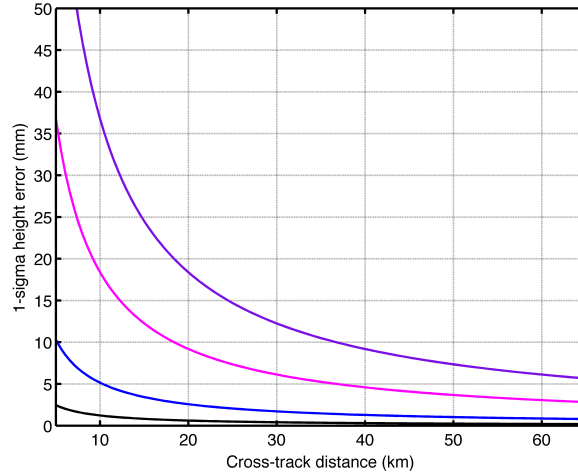


Figure 20. Surf-board effect as a function of cross-track distance for SWH=1, 2, 3, and 4 m.

5.4.5 Overall Random performance

The overall random error uses the decorrelation terms derived in the previous sections to derive the height error performance over a spherical Earth approximation. The coherences are shown in the figure below.

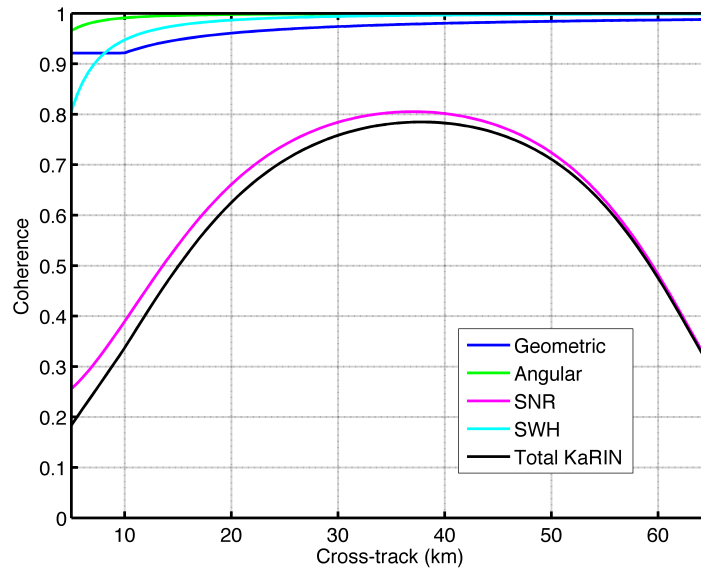


Figure 21. Geometric, angular, thermal (SNR), and volumetric (SWH) correlations across the swath.

The total number of effective looks over a 1 km² ground-range area, ranging from roughly 3,700 to 40,800 looks across the swath, take into account the slight loss in resolution introduced by the filtering stage of the wave-number shift. Finally, the standard deviation of the height error due to the random phase error, relative to the MSS surface implemented in the onboard processor, is given by:

$$\sigma_h = \frac{\rho \sin(\theta_0)}{kB} \sigma_{phase}$$

The standard deviation of the height error due to the overall random error performance across the

swath (including the surf-board effect) is shown in the figure below, with a swath averaged (10 km to 60 km) height error of 2.4 cm.

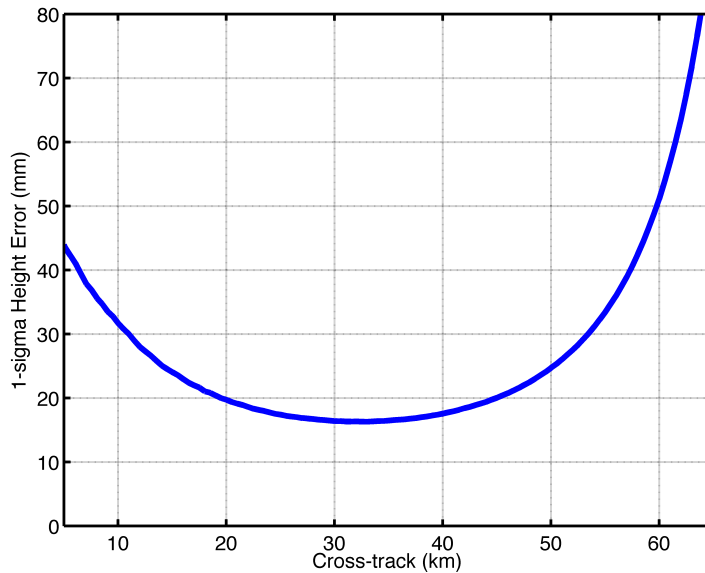


Figure 22. Final ocean height error performance due to all the random errors.

5.5 OCEAN SYSTEMATIC ERROR REQUIREMENTS

The overall flow of the key systematic errors across mission elements is illustrated in the figure below, and each component discussed in detail hereafter.

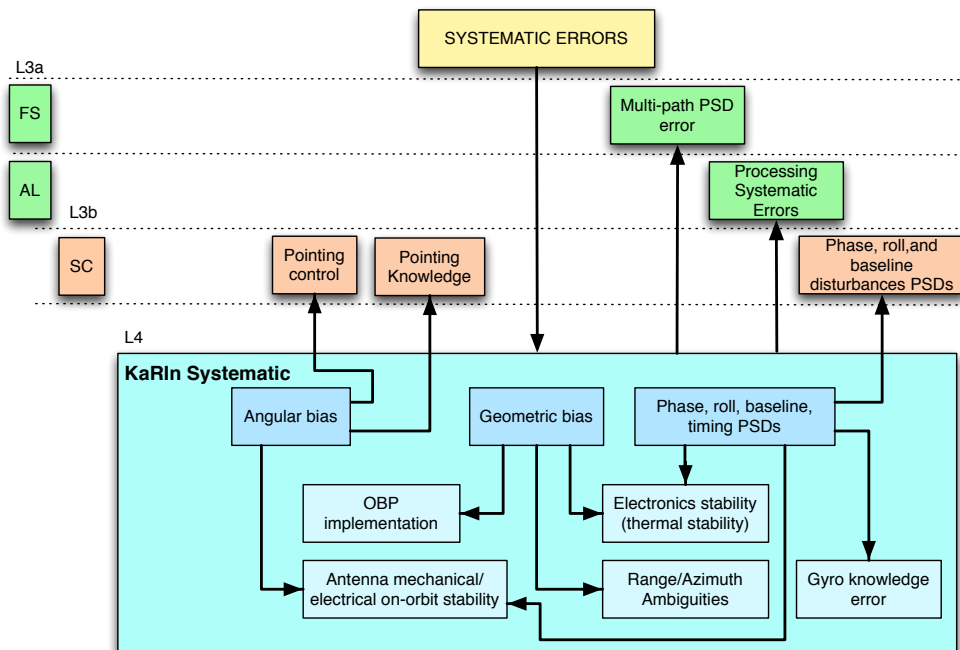


Figure 23. Conceptual high-level flow-down of the random errors to the key mission elements.

5.5.1 Overview of Roll Drift Errors

Knowledge errors in the interferometric roll angle induces height errors, as illustrated in Figure 24. At any given point in time, the height error, δh , due to a roll error $\delta\theta$, is obtained by:

$$\delta h(t) = r(t) \sin(\theta(t)) \delta\theta(t) \approx C \left(1 + \frac{H}{R_E}\right) \delta\theta(t)$$

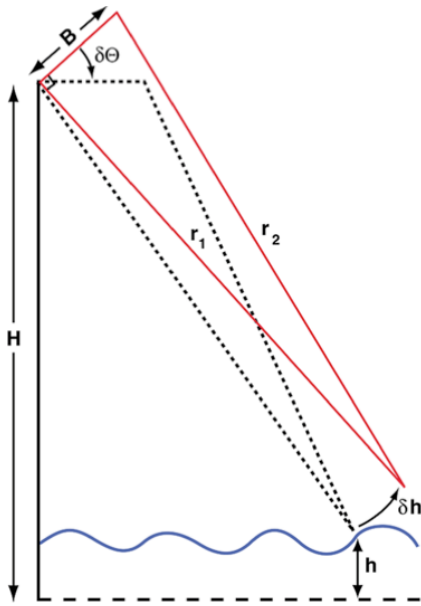


Figure 24. The effect of a roll error is to introduce a tilt to the measured surface

where C is the cross-track distance to the point of interest (i.e., the distance between the nadir point and the pixel of interest), and R_E is the radius of the Earth. The height error due to a roll error grows approximately linearly across the swath, thereby having the effect of creating a local tilt of the entire swath. As an example, a roll knowledge error of only 1/10,000 deg (0.36 arc seconds) would result in a height error of roughly 6 cm for a point situated at 35 km in the cross-track direction. It is thus clear that in order to meet centimetric stability accuracy, a very accurate knowledge of the roll drift is required for SWOT.

The main source of roll errors is knowledge errors in the spacecraft attitude. The KaRIn instrument concept would carry a dedicated, high-performance gyroscope, which would provide the required knowledge of the spacecraft rigid-body roll angle. Gyroscopes (or gyros) measure rotational values without reference to external coordinates. Most gyros for space applications measure the speed of rotation (also known as ‘rates’) in each axis. The residual roll knowledge error typically appears after integration of the rates as an angular drift, increasing linearly over time. The roll error requirement that is thus imposed to the interferometer’s gyro is a residual knowledge error (drift), rather than an absolute knowledge or control requirement. In other words, the platform is not required to limit (control) its roll attitude to very accurate (sub-arcsec) levels to ensure that the height error is bounded (within the limits established by the pointing requirements discussed later, which are not anywhere near these stringent levels), and it is not required to be known in an absolute sense either; the only requirement is that the gyro’s roll drift is small enough to meet the desired centimetric accuracy.

A second source of error in the roll knowledge is introduced by the KaRIn mechanical system formed by the boom and the antenna and feed support structures, due to thermal and vibration distortions. Changes in the on-orbit thermal environment, or dynamics (introduced, for example, during the rotation of the solar arrays, or by the reaction wheels on the S/C), can distort these structures and displace the antennas asymmetrically, effectively introducing a roll error.

Dynamic effects are usually small and can be mitigated by placing isolation mechanisms between the bus and the payload to dampen specific resonant frequencies of the interferometer’s mechanical structures, if needed. To tackle this from the onset, the KaRIn first mode requirement has been specified to be a minimum of 7 Hz, which ensures that any disturbances are not amplified below the 6.5 Hz which relate directly to the ocean SSH measurement spectrum.

The on-orbit thermal environment is typically slowly changing and therefore doesn’t introduce rapid changes in the roll; however the mechanical structures still need to be designed with very low coefficient of thermal expansion (CTE) materials, and standard thermal techniques, such as employing multi-layer insulation (MLI) blankets or low solar absorptivity coatings, where

possible, to minimize both the effect of solar flux transients as well as the effect of shadowing of portions of some specific mechanical structures by other spacecraft surfaces. The Earth’s infrared (IR) and albedo loads are less of disturbance drivers due to their diffuse nature and the relatively constant orientation of the SWOT KaRIn payload to Earth. Periods of eclipse entry and exit can result in sudden changes in incident solar flux, introducing fast disturbances; however, as specified in the Science Requirements Document, the performance requirements do not apply to these eclipse periods, provided the performance degradation does not exceed 5% of the time, including all possible effects.

Specifying the allowed height error as a function of time (or, equivalently, along-track distance), the roll power spectrum for a given cross-track distance, C , is just the height error power spectrum divided by C^2 . Specifically, if the root-mean-squared (RMS) error obtained by integrating the height error spectrum in a specific band for a given C is $\sigma_h|C$, the RMS roll spectrum (in radians) will be $\sigma_\theta|C = \sigma_h|C/C$. This raises the question of what cross-track distance should be used to define the requirement. In reality, the specification is given as a swath-averaged performance, rather than the performance at a given cross-track distance (e.g., the far swath). Denoting $f(\delta h, C)$ as the probability density function of height error and cross-track distance, the swath averaged height variance, σ_h^2 is given by:

$$\begin{aligned} \sigma_h^2 &= \int dC \int d\delta h (\delta h)^2 f(\delta h, C) = \sigma_\theta^2 \left(1 + \frac{h}{R_E}\right) \int dC f(C) C^2 \\ &= \sigma_\theta^2 \left(1 + \frac{h}{R_E}\right) \left[\frac{C_{max}^3 - C_{min}^3}{3(C_{max} - C_{min})} \right] \triangleq \sigma_\theta^2 \left(1 + \frac{h}{R_E}\right) \bar{C}^2 \end{aligned}$$

where it has been assumed that $f(C)$ is uniformly distributed over the swath. Therefore, the swath-averaged performance is equivalent to the performance evaluated at a point C given by:

$$\bar{C} = \sqrt{\frac{C_{max}^3 - C_{min}^3}{3(C_{max} - C_{min})}}$$

For KaRIn, with a swath extending from 10 km to 60 km, $C \approx 37.9$ km. The flow-down of the roll error into all the different elements is shown in the figure below.

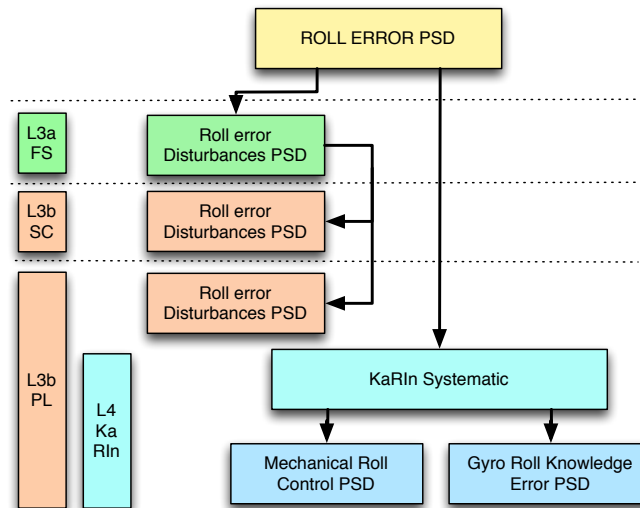


Figure 25. Conceptual high-level flow-down of the roll PSD to the key mission elements.

For KaRIn, the gyro roll error spectrum is directly allocated by KaRIn as part of its systematic errors, and is based upon the end-of-life noise model requirements for the candidate gyro. The noise model, following the IEEE standard for a single sided PSD, is then given by:

$$PSD_{gyro}(f) = 1.695 \cdot 10^{-8} + 6.303 \cdot 10^{-7}f^{-2} + 4.756 \cdot 10^{-13}f^{-3} + 5.168 \cdot 10^{-19}f^{-4} \text{ [asec}^2/\text{cy/km]}$$

and is shown in the figure below.

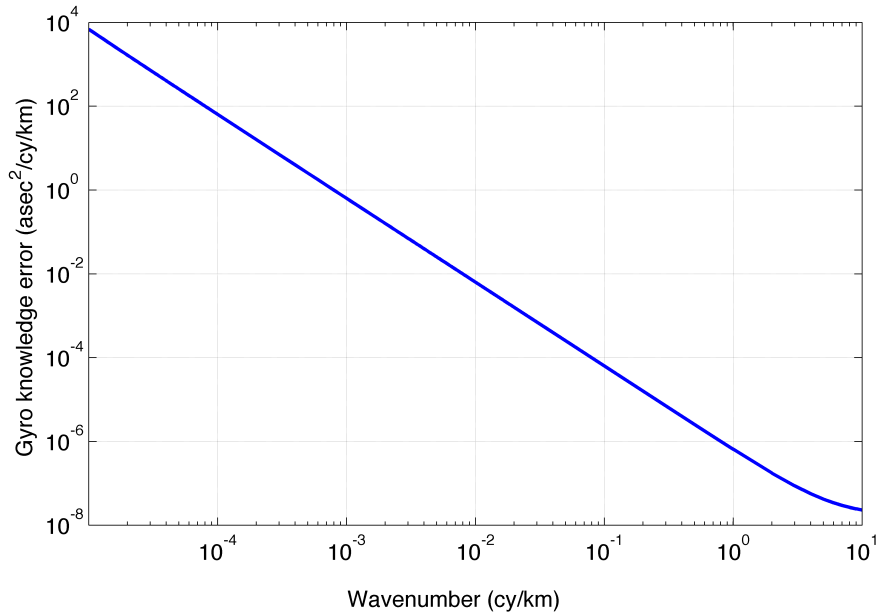


Figure 26. PSD of the gyro roll knowledge

The conversion to an SSH error is then given by:

$$E_{gyro}(f) = PSD_{gyro}(f) \cdot \left(1 + \frac{h}{R_E}\right)^2 \cdot \bar{C}^2 [km] \cdot 10^6 \left(\frac{cm}{km}\right)^2 \cdot \left(\frac{\pi}{64800}\right)^2 \left[\frac{cm^2}{cy/km}\right]$$

Of the overall systematic error, the roll error (excluding the gyro) is sub-allocated 20% of the systematic errors. The Flight System roll control error associated to dynamic effects on the KaRIn roll is sub-allocated a large fraction of the high frequency region, and less of the low frequency region, as given in the figure below. The rest is sub-allocated directly to the KaRIn mechanical structures. The corresponding PSDs, in units of asec²/Hz, are:

$$E_{F/S roll} = \begin{cases} 6.73 \cdot 10^{-8} f^{-2.17}, & f < 0.1367 \text{ Hz} \\ 5.05 \cdot 10^{-6}, & f \geq 0.1367 \text{ Hz} \end{cases} \text{ [asec}^2/\text{Hz]}$$

The Flight System PSD is then further sub-allocated into S/C and Payload (non-KaRIn) components. Of the total, 95% of the PSD goes to the S/C, where most of the disturbances (eg. reaction wheels, solar arrays, etc.) are expected. The residual 5% goes to the Payload to cover non-S/C induced dynamics (such as micro-dynamics associated to the payload structures).

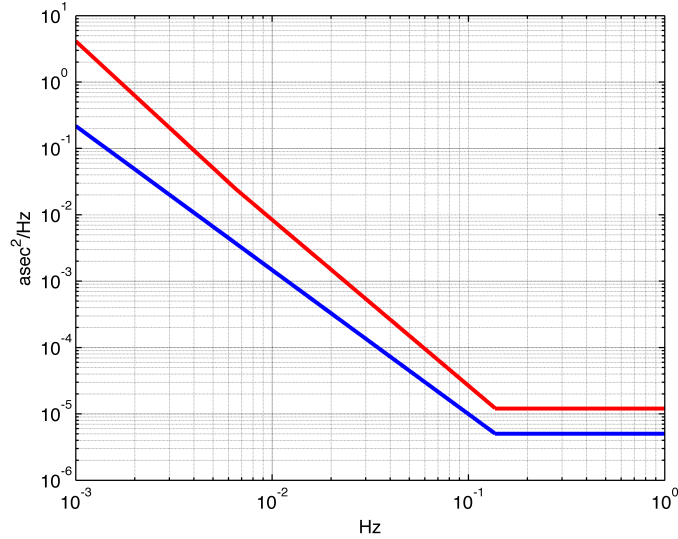


Figure 27. (blue) PSD of the roll allocation to the Flight System; for reference the total systematic error allocated to the roll is also shown (red)

5.5.2 Overview of Differential Phase Drift Errors

Systematic phase errors arise due to changes in the relative phase between the two signal paths in the interferometric pair. An illustration of the impact of a phase error on the height measurement is presented in **Figure 28**. The height error introduced by a phase error is given by:

$$\delta h = \frac{\lambda r \tan(\theta)}{2\pi B} \delta\phi \cong \frac{C}{kB} \left(1 + \frac{H}{R_E}\right) \delta\phi$$

A differential phase drift has the effect of creating a height error that also increases linearly across the swath, like a roll error. There are several contributors to the phase imbalance between the two interferometric radar channels, which are associated to the different Flight System and KaRIn elements:

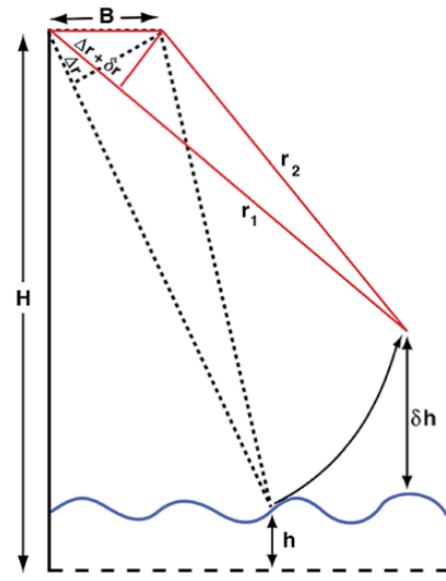


Figure 28. Illustration of the impact of a phase error on the height estimate.

1) A phase drift between the two interferometric radar channels introduced by any of the radar electronics subsystems. Phase drifts in the radar electronics are mostly temperature driven, and therefore slowly varying. On the one hand, any phase drift in the transmit chain automatically cancel outs since it is common to both receive channels. Therefore, only the relative drift between the two radar receive chains is of concern. To mitigate this error source, a calibration loop for each path is part of the instrument design, which can serve to correct some of the drifts. In addition, KaRIn defines thermal control drift rates requirements (both absolute and relative) for the thermal subsystem with regards to the relevant radar electronics boxes.

2) A phase drift introduced by the antenna and mechanical/thermal subsystem. These are thermal or vibration induced mechanical distortions in the antenna

subsystem (either in the reflectarray antennas or the feeds) that can change the phase response of the overall antenna system. Here, two distinct contributions pertaining to a systematic phase drift arise: (1) an effective displacement of the phase center of the antenna, and (2) a change in the actual far-field phase pattern response over the main-lobe (and over the transmit frequency bandwidth) that illuminates either swath. This second terms would be the variation of the “phase screen”, and requirements imposed on the KaRIn antenna and mechanical system ensure that this error term is appropriately bounded. In addition to thermal distortions, dynamic disturbances generated within the S/C may propagate through the KaRIn structures and generate resonances or oscillations in its structures and need to also be considered.

- 3) System phase mismatch. These are phase drifts induced by multi-path and external signals. If e.g. a small portion of the radiated power is reflected back by any of the spacecraft surfaces, a phase bias will be induced on the desired interferometric measurement. Any changes in the reflected signal over time (both in phase and amplitude), can result in a change of this bias term, thereby introducing a systematic phase drift. Multi-path signals can be classified as being either coherent with the direct signal, incoherent with the direct signal but coherent with itself (as measured by the two interferometric channels), or incoherent. The main effect of incoherent multi-path is only to reduce the available SNR, since it behaves as a noise source, thereby impacting the random error performance. Correction of multi-path errors is typically performed post launch, when a high-fidelity model of the spacecraft is available. Moving surfaces, such as solar array rotations, are expected to constitute the main source of multi-path induced phase drifts. However, the SWOT concept only rotates its solar arrays at the top and bottom of the orbit every few days, thereby greatly mitigating any multi-path induced phase drifts over the time scales associated to the sub-mesoscale measurement. In addition, part of the cal/val activities is the determination of a phase screen correction, which may need to be obtained as a function of solar array rotation.

The flow-down of the phase error to all of the appropriate elements is shown in the figure below.

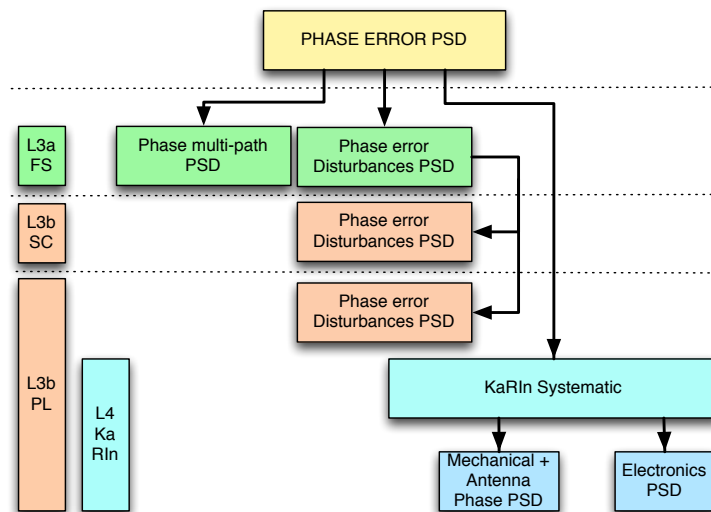


Figure 29. Conceptual high-level flow-down of the phase PSD to the key mission elements.

The total phase error is allocated 60% of the overall systematic error. The RMS phase drift for the swath average performance can be derived in a similar fashion as to what has been derived

before for the roll error:

$$\sigma_h^2 = \frac{\sigma_\phi^2}{(C_{max} - C_{min})} \left(1 + \frac{h}{R_E}\right) \int dC \left(\frac{C}{kB}\right)^2 = \frac{\sigma_\phi^2}{(kB)^2} \left(1 + \frac{h}{R_E}\right) \left[\frac{C_{max}^3 - C_{min}^3}{3(C_{max} - C_{min})} \right]$$

$$\triangleq \frac{\sigma_\phi^2}{(kB)^2} \left(1 + \frac{h}{R_E}\right) \bar{C}^2$$

The overall phase error spectrum is shown in the figure below, which is further sub-allocated to the Flight System (for dynamic effects on the KaRIn phase), system multi-path, and KaRIn. The phase error spectrum sub-allocated to the S/C is given by 95 % of the Flight System PSD below, in units of deg²/km, with the P/L receiving the remaining 5%.

$$E_{F/S}(f) = \begin{cases} 3.483 \cdot 10^{-7} f^{-2.17}, & f > 0.1367 \text{ Hz} \\ 2.614 \cdot 10^{-5}, & f \leq 0.1367 \text{ Hz} \end{cases}$$

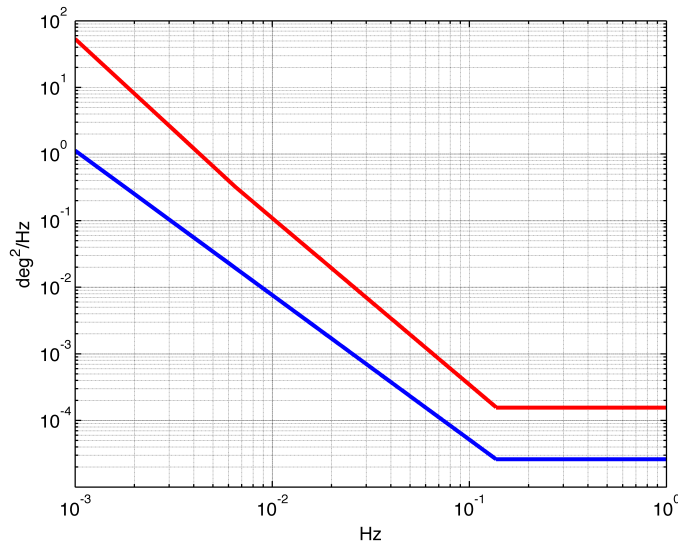


Figure 30. (blue) PSD of the phase allocation to the S/C; for reference the total systematic error allocated to the phase is also shown (red)

KaRIn received the remaining portion of the error spectrum of the differential phase drift, which is sub-allocated into the following components:

- The KaRIn mechanical/thermal, for distortions in the baseline, reflectarray antenna and feed support structures (20 %);
- The KaRIn antenna electrical performance, for deformation errors in the panels, changes in the dielectric constants of the panels (20%),
- The KaRIn electronics (RF and digital) and waveguides (57%).

The remainder (3%) is flowed up to the overall Flight System for multi-path effects. The current sub-allocations are based on engineering judgment and preliminary analysis, and will be adjusted as needed throughout the life of the mission. The figure below shows the KaRIn sub-allocations, as well as the system multi-path.

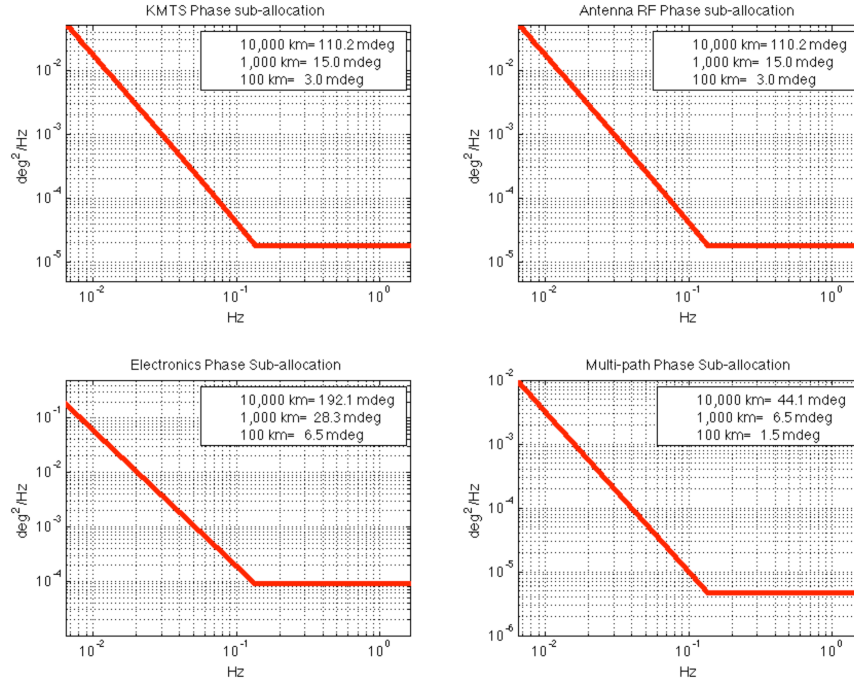


Figure 31. Sub-allocation of the differential phase drift onto the different KaRIn elements (KaRIn Mechanical/Thermal System –KMTS-, Antenna, and Electronics) and the Flight System multi-path.

5.5.3 Overview of Baseline Dilation Drift Errors

As with any interferometer, a change in the baseline length directly impacts the precision of the height measurements that can be obtained. For SWOT, the baseline length is to be understood as the projection onto the YZ plane of the line that crosses the two reference coordinate systems previously defined at each end of the mast. The height error introduced by a baseline error δB is given by:

$$\delta h = -\frac{r \sin(\theta) \tan(\theta)}{B} \delta B \approx -\left(1 + \frac{H}{R_E}\right) \frac{C^2}{HB} \delta B$$

A baseline dilation error has therefore the effect of creating a quadratic height error across the swath.

The baseline error is allocated 5% of the overall systematic error. The flow-down of the baseline error to all of the appropriate elements is shown in the figure below.

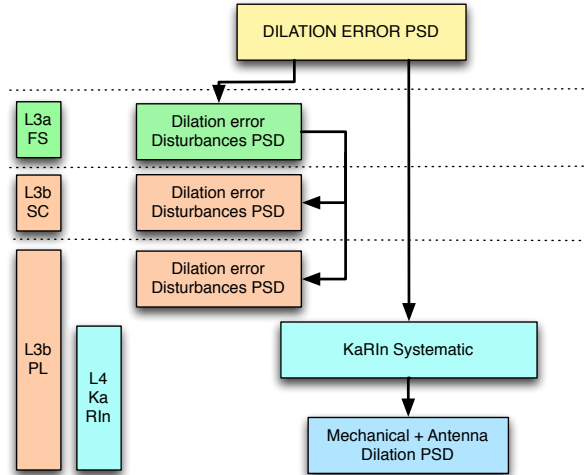


Figure 32. Conceptual high-level flow-down of the baseline PSD to the key mission elements.

The RMS baseline drift for the swath averaged performance can be derived in a similar fashion as to what has been derived before:

$$\sigma_h^2 = \frac{\sigma_B^2}{(C_{max} - C_{min})} \left(1 + \frac{h}{R_E}\right) \int dC \left(\frac{C^2}{HB}\right)^2 = \frac{\sigma_B^2}{(HB)^2} \left(1 + \frac{h}{R_E}\right) \left[\frac{C_{max}^5 - C_{min}^5}{5(C_{max} - C_{min})} \right]$$

The overall baseline error spectrum is shown in the figure below. The baseline error spectrum allocated to the Flight System (for dynamic effects on the KaRIn baseline length) is given by the PSD allocation below, in units of $\mu\text{m}^2/\text{km}$.

$$E_{F/S}(f) = \begin{cases} 0.0139 \cdot f^{-2.17}, & f > 0.1367 \text{ Hz} \\ 1.0445 \cdot 10^{-5}, & f \leq 0.1367 \text{ Hz} \end{cases}$$

Of that allocation, the baseline length error spectrum sub-allocated to the S/C is given by 95 % of the PSD below, in units of deg^2/km , with the P/L receiving the remaining 5%. KaRIn receives the rest of the allocation, and is allocated to the mechanical system.

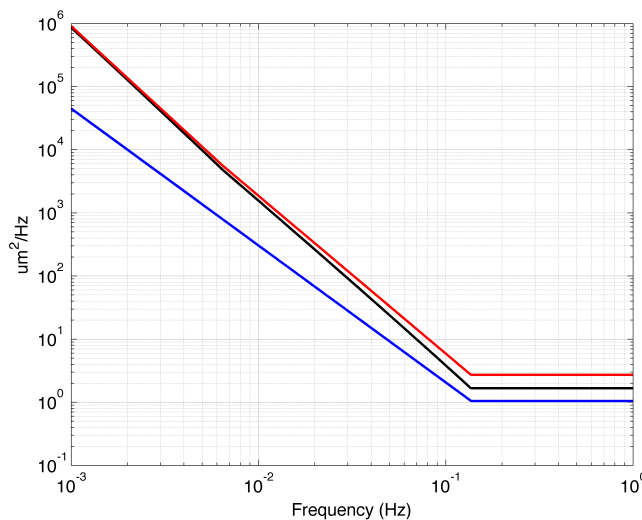


Figure 33. (red) total systematic error allocated to the baseline dilation; (blue) PSD of the dilation allocation to the F/S; (black) dilation error directly allocated to KaRIn.

5.5.4 Timing (Common Group Delay) Drift Errors

This system timing error corresponds in practice to a common group delay error. A system timing error δt will introduce a height error given by:

$$\delta h = -\cos(\theta) \delta r \approx \frac{c}{2} \cos(\theta) \delta t$$

where c is the speed of light, and θ is the look angle. Since KaRIn operates in a near nadir geometry, the look angle variation across the swath is small, and therefore a timing drift error has the effect, to first order, of creating a constant height bias across the swath. The RMS timing error for the swath average performance, ignoring the look angle dependence is thus given by:

$$\sigma_h^2 = \frac{\sigma_t^2}{(C_{max} - C_{min})} \int dC \left(\frac{c}{2} \cos(\theta_{look}) \right)^2 = \sigma_t^2 \left(\frac{c}{2} \right)^2$$

The timing error is allocated 10% of the overall systematic error. The flow-down of the timing error to all of the appropriate elements is shown in the figure below.

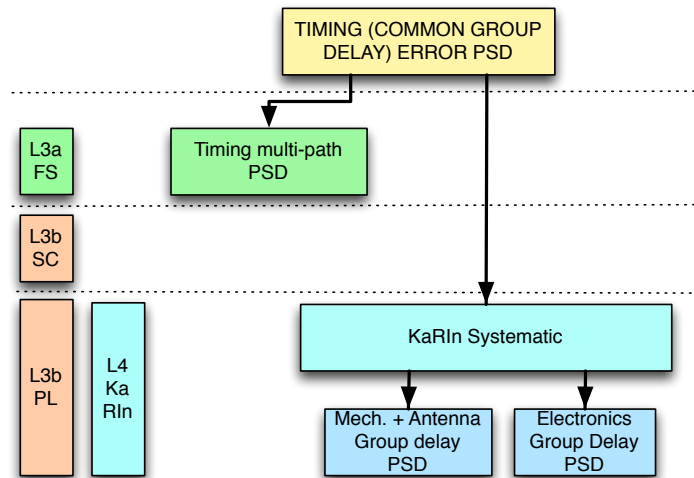


Figure 34. Conceptual high-level flow-down of the group delay PSD to the key mission elements.

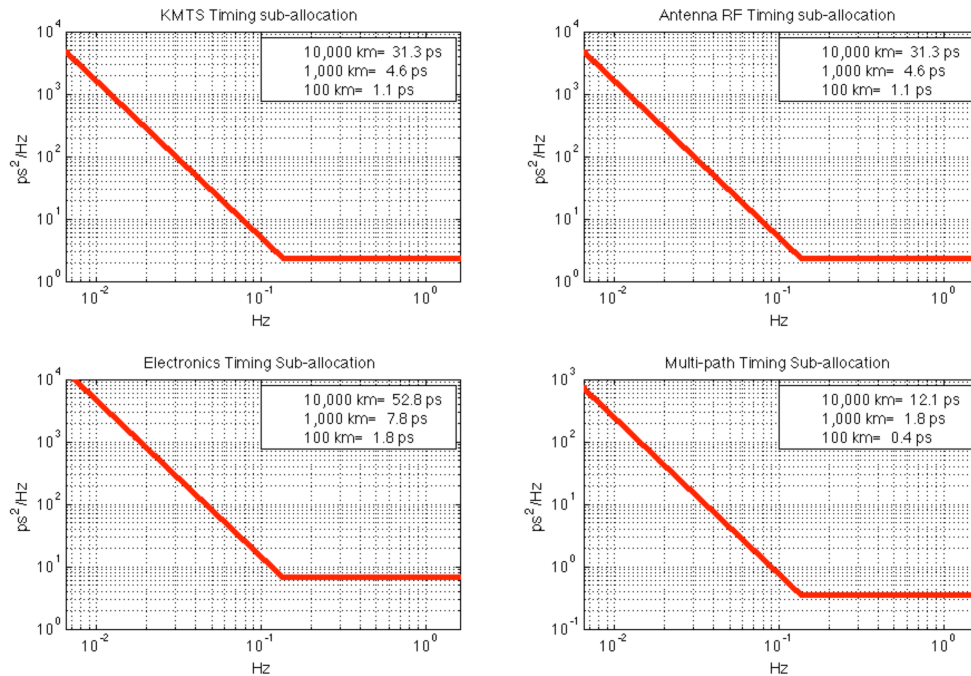


Figure 35. Sub-allocation of the group delay drift onto the different KaRIn elements (KaRIn Mechanical/Thermal System –KMTS-, Antenna, and Electronics) and the Flight System multi-path.

5.5.5 Orbit Radial Knowledge Errors

An orbit height error of δh directly translates into a high error of the same amount, since the desired topographic measurement assumes perfect knowledge of the orbit’s altitude.

In order to characterize orbit errors at the spatial scales of interest, a simulation was performed to obtain the spectral density of the POD height error, including short wavelengths (down to ~ 250 km). The simulation used a model of the spacecraft shape, volume, and orientation along its orbit, and a worst-case solar flux (the maximum observed for year 2001), and the OSTM spacecraft attitude control system (ACS). The simulation also included surface forces, such as drag, solar and Earth radiation, and Earth gravity field. As a result, orbit deviations from the nominal can be obtained, and the simulated residual error from the onboard high-precision GPS (similar to the one flying on Jason-2) is derived. The long-wavelength results (down to 10,000 km) exhibit the typical peak that occurs at the once per revolution frequency. The medium-wavelength plot shows that starting at wavelengths of 5,000 km and lower, the error starts behaving quite accurately as a power law, and is becoming quite small. This is expected, since the GPS does not really resolve the orbit down to these short scales, and the error is purely the actual orbit deviation –and the knowledge error is really just the error in the integrator used for POD reconstruction. This effectively imposes a full dynamic POD, where the orbital motion of the S/C is strongly constrained by dynamic models, to minimize the noise of the integrator. A similar analysis was performed using the DORIS solutions. Both results are shown in the figures below.

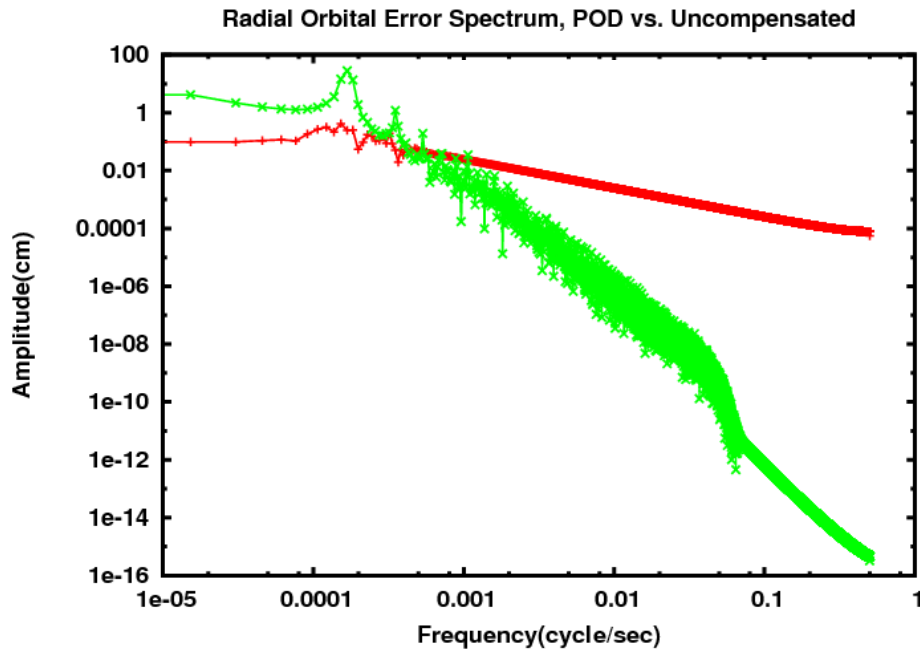


Figure 36. (green) theoretical radial orbital error spectrum due to the along-track perturbation without POD; (red) actual radial orbital error spectrum after POD using GPS, all error sources included. The two spectra intersect at about 3 cycle/rev. The POD solution does not reduce the high frequency errors, due to the GPS measurement noise and sampling rate.

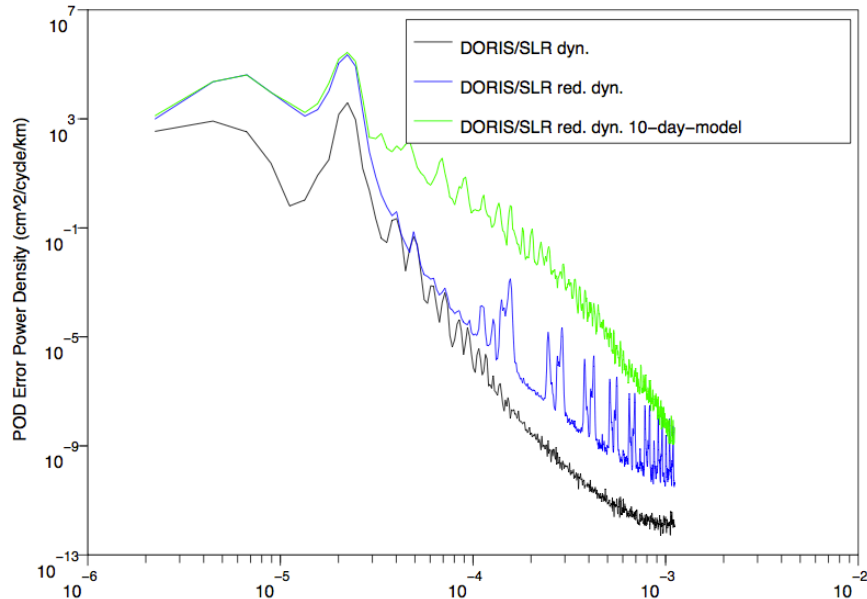


Figure 37. Spectral analysis of the radial differences between a degraded and a reference orbit solution (figure courtesy of CNES). The degraded orbit corresponds to ENVISAT DORIS-only orbit computed with the EIGEN-GL04S-Annual gravity field with the drift terms removed. The reference orbit is the DORIS/SLR reduced dynamic orbit with the most up-to-date gravity field model (10-day Grace solution). The radial difference between the degraded orbit and the reference orbit gives insight into the radial error.

An additional term associated to height uncertainty appears due to drifts in the Flight System Center of Gravity (CoG). For example, deformations in the solar array panels and the payload structures, and fuel consumption, will displace the CoG in the POD solution from the reference

CoG point that is used to make the height corrections.

Finally, an error term appears due to deformations of the interferometric baseline, which could cause a drift in its radial center. These deformations appear mainly due to on-orbit thermoelastic effects.

The following constitutes the overall spectral envelope for the orbit height error spectrum:

$$E_{Orbit}(f) = 1.9631 \cdot 10^{-5} f^{-1.9922} \text{ [cm}^2/\text{cy/km]}$$

The integrated SSH error for wavelengths between 1 and 1,000 km for the derived envelope is 0.14 cm. This error is sub-allocated as 90% to the Flight System, and 10% to the Mission System for POD processing. Of the first 90%, 90% is further sub-allocated to the S/C as the major contributor to the uncertainty in the drift of the CoG, 5% to the Payload for changes in the CoG associated to payload distortions, and 5% to shifts in the radial height of the KaRIn interferometric baseline. The flow-down of the allocations is shown in the figure below.

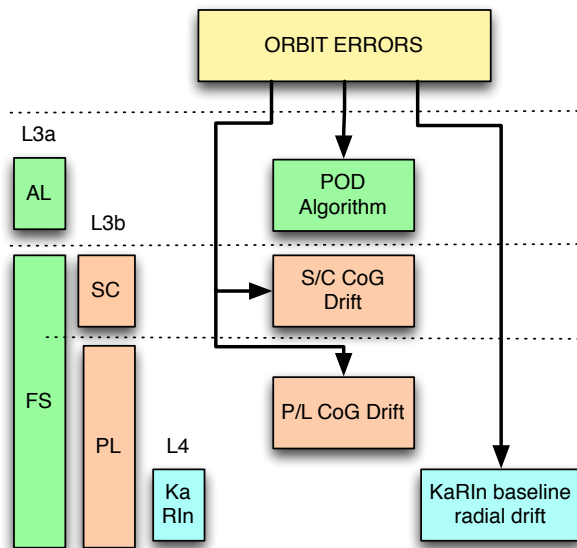


Figure 38. Flow-down of the Orbit height error.

The associated PSD, all expressed in $\text{cm}^2/\text{cy}/\text{km}$, are as follows:

$$E_{POD}(f) = 0.1 \cdot E_{Orbit}(f) = 1.9631 \cdot 10^{-6} f^{-1.9922}$$

$$E_{FS\ CoG}(f) = 0.9 \cdot E_{Orbit}(f) = 1.7668 \cdot 10^{-5} f^{-1.9922}$$

and the sub-allocations to the lower levels are:

$$E_{SC\ CoG}(f) = 0.9 \cdot E_{FS\ CoG}(f) = 1.59 \cdot 10^{-5} f^{-1.9922}$$

$$E_{PL\ CoG}(f) = 0.05 \cdot E_{FS\ CoG}(f) = 8.834 \cdot 10^{-7} f^{-1.9922}$$

$$E_{KaRIn\ radial\ drift}(f) = 0.05 \cdot E_{FS\ CoG}(f) = 8.834 \cdot 10^{-7} f^{-1.9922}$$

The figure below shows the PSD of all the components.

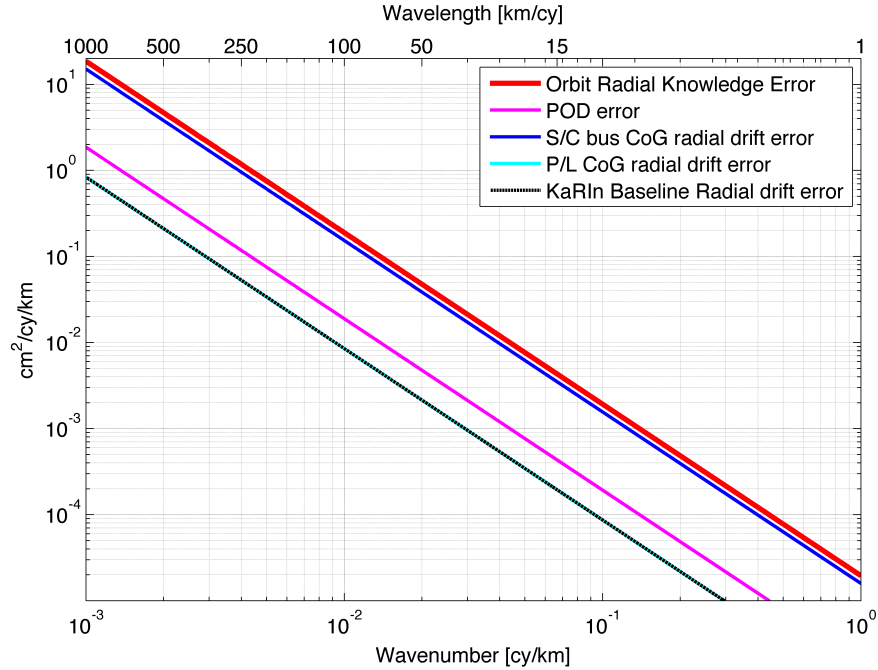


Figure 39. PSDs of the different contributors to the orbit radial height knowledge drift.

5.5.6 Wave Averaging Errors

The presence of surface gravity waves will introduce an additional source of height noise, since the average of the wave height over a 1 km² pixel would not be exactly zero. In this section we analyze this error source in detail, and show that the averaging introduces a small residual height error, which can be further reduced by simply using weighted averaging, which is implemented in the KaRIn Onboard Processor.

Real ocean wave spectra are a mixture of a continuous spectrum of wind-generated waves with swell, which is not generated by the local wind. For a continuous spectrum, the surface height can be written as

$$h(x) = \int dk a(k)e^{ik \cdot x}$$

where $k = 2\pi/\lambda$ is the wave-number, and $a(k)$ is the complex wave amplitude, related to the wave spectrum, $S(k)$, by:

$$\langle a(k)a^*(k') \rangle = \delta(k - k')S(k)$$

To obtain the average height over a given resolution cell of characteristic dimension L , we form the weighted average centered at coordinate x_0 , given by:

$$\bar{h}(x_0) = \frac{1}{L} \int dx w(x - x_0)h(x)$$

where:

$$L = \int dx w(x)$$

and $w(x)$ is the spatial weighting function. Defining $W(k)$ as the Fourier transform of $w(x)$, it is not difficult to show that the average height variance will be given by:

$$\langle (\bar{h})^2 \rangle \approx \int d^2 k S(k) |W(k)|^2$$

The figure below shows the height error as a function of ocean wavelength for a Pierson-Moskowitz wave spectrum for a fully-developed sea in two cases: unweighted (rectangular) and weighted (Blackman-Harris) averaging.

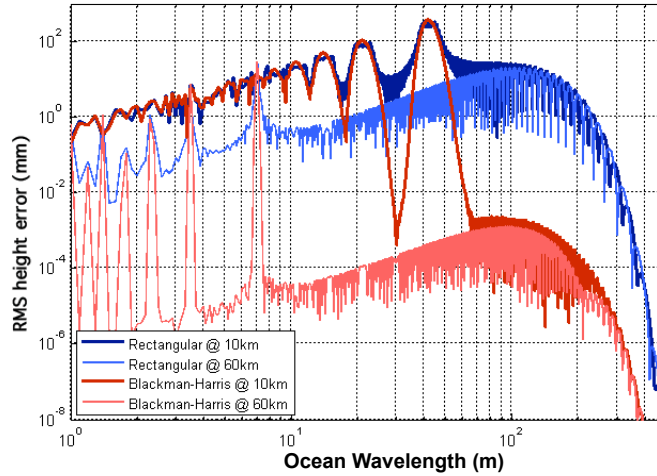


Figure 40. Height error as a function of ocean wavelength (in meters) using a Pierson-Moskowitz wave spectrum (not considering the effect of the instrument resolution).

This effect introduces height errors that are higher in the near-swath. Besides the fact that the number of cross-track pixels that can be averaged to form the 1 km² output pixel is smaller in the near swath due to the lower intrinsic resolution, a significant contribution to the overall error comes from the spectrum exhibiting numerous peaks at wavelengths smaller than 100 m, most remarkably at around 22 m and 43 m. This is in fact an aliasing effect that occurs when the wavelength, for a given look geometry, is such that $e^{ikx} = 1$, combined with the fact that the wave spectrum has a significant amount of energy in this wavelength region. The effect is worse at the near swath due to the lower incidence angle; at higher incidence angles, the peaks occur at much lower wavelengths, where the wave spectrum exhibits smaller amplitudes. In these cases, where the spectrum peaks, windowing cannot reduce the error.

However, the intrinsic resolution of the interferometer also needs to be taken into account, as the resolution at the near range is comparable to (or coarser than) these aliased wavelengths. In practice, this will smear the peaks and therefore reduce the error. Approximating the one-dimensional interferometric impulse response, $\chi(x)$, by a sinc-squared function of intrinsic resolution B_x (and ignoring here, for simplicity, the effect of the antenna pattern), the average height variance is now given by:

$$\langle (\bar{h})^2 \rangle \approx \int d^2 k S(k) \left| W(k) \Lambda\left(\frac{B_x}{2\pi} k\right) \right|^2$$

where $\Lambda(k)$ is the Fourier transform of $\chi(x)$, ie. the triangular function defined as $\Lambda(k) = \max(1 - |k|, 0)$. As a result, the system's limited resolution reduces the contribution of the wave spectra to within the range of wavelengths that can be resolved, effectively filtering out longer ones. The resulting residual error is large for the unweighted averaging case, where it reaches over 5 mm. However, using a Blackman-Harris weighting window lowers the residual error by almost four orders of magnitude, to less than 10⁻³ mm.

5.5.7 Processing and Bias correction errors

As previously discussed, the OBP plans to produce 9 different complex products from which a final averaged interferogram would be produced on the ground; as a result, a height map would be produced, among other products, on the ground.

As part of the ground processing, the following simplified set of corrections are required to compensate for some of the OBP simplifications and other error sources that introduce biases:

1. Remove the angular systematic bias that results from the iso-range lines and the iso-phase lines not being aligned.
2. Resample the beams to adjust for the different viewing geometries.
3. Compute heights for each beam correcting for the slightly different baselines.
4. Perform optimal beam averaging.
5. Resample the pixels to a fixed grid

Information on the spacecraft attitude will be needed to perform these corrections, as well as several basic static or quasi-static parameters (antenna phase screens, common and differential range delays, static roll angle, etc.), which would be obtained during the cal/val phase, or estimated periodically as needed.

A PSD for systematic errors associated to the algorithms used during ground processing to perform the bias and other corrections is allocated as 20% of the overall systematic errors, which is given by the following expression:

$$PSD_{alg}(f) = \begin{cases} 2.2 \cdot 10^{-6} f^{-2.5}, & 0.021 > f \geq 10^{-3} \text{ cy/km} \\ 3.42 \cdot 10^{-2}, & f > 0.021 \text{ cy/km} \end{cases}$$

The spectrum integrates to 0.219 cm from 15 to 1,000 km, and is shown in the figure below.

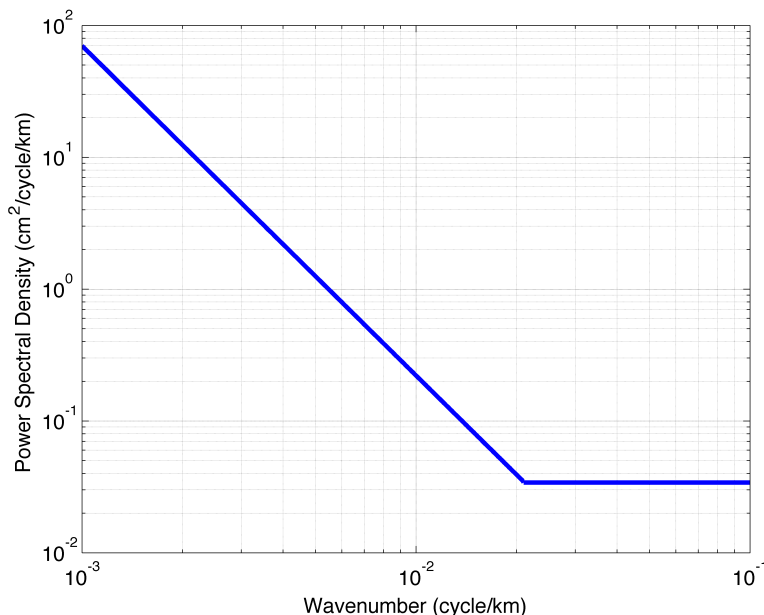


Figure 41. Sub-allocation of the systematic errors to Algorithms.

5.5.8 Wavelength drifts

While the initial transmit frequency of the radar would be measured and therefore known before launch, a drift over time of the KaRIn effective center frequency would introduce a height error given by the following equation:

$$\delta h = r_0 \tan(\theta) \sin(\theta) \frac{\delta \lambda}{\lambda}$$

Factors such as drifts in KaRIn's reference stable oscillator (STALO), spectral filtering, and notching in the waveforms affect the effective wavelength. For KaRIn, the primary source of drift is introduced by the STALO. However, the system is designed to limit the long-term drift of the oscillator, achieving a $\delta \lambda / \lambda < 1.5 \mu m$. In this fashion, this systematic error can be neglected, as it contributes < 0.1 mm of error.

6 HYDROLOGY MEASUREMENT REQUIREMENTS AND ERROR BUDGET

The error budget for hydrology can be split into three main sections: height errors, slope errors, and water classification errors. All of these are discussed in the following sections.

6.1 Height and slope accuracy requirements

The hydrology height error requirement is 10 cm for an area of 1 km². The derivation of the error budget follows the same methodology and structure as that of the ocean in terms of the top-level errors, which are separated between media, systematic, and random errors. The main differences for hydrology are that: 1) Sea State Bias errors over surface water are not considered since, with the exception of the Great Lakes region and other very large water bodies, the effects of SWH over rivers and other water bodies is considered to be negligible; 2) contrary to oceanography, there is an understanding that the requirements apply over time periods that are longer than a land pass. In order to be able to compute storage change, any drift between two given passes needs to be removed. This requires the use of calibration techniques (e.g., cross-overs), which are able to delete the time history of any drifts between two passes using optimal interpolation techniques.

The characteristics of the errors change depending on the direction. For height errors, the cross-track errors are dominated by the residual error after cross-over correction, leaving an uncorrected slope error going into the land pass that is not insignificant, whereas in an along-track sense, the slope is changing slowly. For slopes, the most significant error term is associated with the random noise of the measurement since, as will be discussed later, the derivative of a spectrally “flat” white noise becomes a red spectrum that grows as the square of the frequency.

A top-level break-down of the error budget is summarized in the table below:

Hydrology Error Component	Height Error [cm]	Slope Error [urad]	Comments
Ionosphere signal	0.8	0.1	RMS of the full signal for maximum solar activity (100 TECU), using IONEX model
Dry Troposphere Signal	0.7	0.1	RMS after correction with weather models, based on Jason heritage
Wet Troposphere Signal	4.0	1.5	Model-based correction
Orbit Radial Component	1.62	0.5	Orbit error RMS
KaRIn Random and Systematic Errors after Cross-Over Correction	8.9	8.2	Includes cross-over correction residual
Total Allocation (RSS)	9.95	8.35	Total error, as allocated
Unallocated margin RSS/SUM	1.0 / 0.05	5.5 / 1.65	
Total (RSS) Error	10	10	Requirement

6.1.1 KaRIn Performance for Hydrology

The KaRIn performance over land surface water is again divided into systematic and random errors. The break-down of the overall KaRIn requirement is shown in the table below.

KaRIn Hydrology Error Component	Height Error [cm]	Slope Error [urad]	Comment
KaRIn Random	4.4	8.0	Height based on a 1km ² averaging area of water-only pixels; slope based on a 10 km downstream averaging of a 100 m river.
KaRIn Systematic cross-track errors after cross-over correction	7.4	1.7	Residual after cross-over correction; these are the RMS cross-track slopes (and associated height) for the entire along-track land pass.
KaRIn Systematic along-track height bias error	1.5	0.08	This is the RMS timing and dilation along-track height errors accumulated down to 0 Hz.
High Frequency errors	1.15	0.5	RMS of systematic errors > 6.5 Hz
(Unallocated margin, RSS)	1.23	0.31	
Total (RSS) Error Requirement	8.9	8.2	Requirement

6.2 Cross-over correction for Systematic Error removal

This technique exploits the fact that, at ocean cross-over points, a direct comparison can be made between KaRIn measurements, and that some of the interferometer systematic errors can be estimated (and therefore, reduced) from the cross-over differences themselves. The geometry of the cross-overs is illustrated in figure Figure 42. This approach can only use cross-over points over the oceans but, conceptually, has the effect of reducing any drifts incurred due to “past history” so that the absolute error over land throughout the mission only needs to consider the residual errors after this correction, plus any drifts accumulated over the land passes themselves.

For each cross over point, a cross over diamond grid, indicated by the dashed area, results from the overlap between an ascending and a descending pass. It is important to note that there are two relevant time scales involved: first, the time (or distance) separation between all of the adjacent cross-over points along the orbit that fall over the oceans. For the proposed SWOT orbit, this time (the separation between consecutive ocean cross-overs points) would always be less than 80 sec, or ~500km, and it is a strong function of latitude. The second time scale is associated to the fact that a given cross-over point is formed by the intersection of two separate orbital ground tracks, which correspond to observations of the ocean that could be as far apart as several days. Assuming only passes that are within +/- half a cycle are used in forming the cross-overs, that results in a maximum separation of up to 11 days between the crossing swaths.

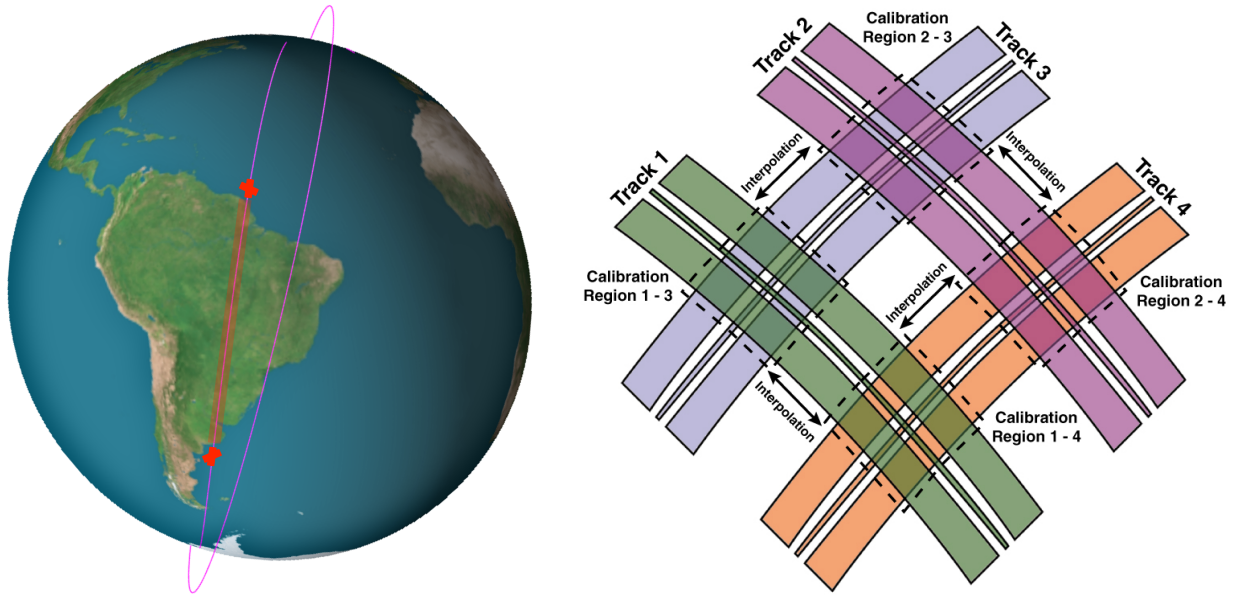


Figure 42. (left) Illustration of the closest cross-over points for a given land pass; (right) Illustration of the cross-over geometry. The diamonds where the slope errors are estimated are indicated by the dashed line; in between them, the slopes are interpolated.

The cross-over algorithm, in its most basic form, performs the correction in two distinct steps: 1) first, it estimates at every cross-over point, using a least squares fit, the equivalent cross-track slopes that the roll, phase, baseline, and other errors introduce; and 2) uses these estimates for all the cross-over points to perform an optimal interpolation and obtain the optimal slope throughout the orbit. Since the effect of a roll error and a phase error is effectively the same, i.e., to create a linear height error across the swath, the algorithm is not able to separate roll from phase errors, and a combined phase plus roll error is estimated. In addition, the phase and group delay errors may not generally be the same for both swaths, requiring the algorithm to estimate separate errors for each swath (left and right).

The accuracy of the estimated parameters depends on the number of cross-overs that can be used simultaneously in the estimation, their spatial and temporal separation, which as previously mention varies as a function of latitude, and the magnitude of the errors. The fundamental limitation to this technique is actually established by the decorrelation time of the ocean over the cross-over points used for estimation, which for the most part determines the minimum residual slope error that can be achieved (corresponding to roughly 0.8 urad). This also effectively limits the algorithm to using only cross-overs that are relatively close in time (within +/- half a cycle between the passes that form the cross-over point).

Initial results based on simulations indicate that the cross-over technique is able to remove systematic errors and meet the required residual error allocations. The figures below illustrate the results of using this technique, where the residual RMS over land is 1.4 urad (and the residual for the ocean is 0.7 urad).

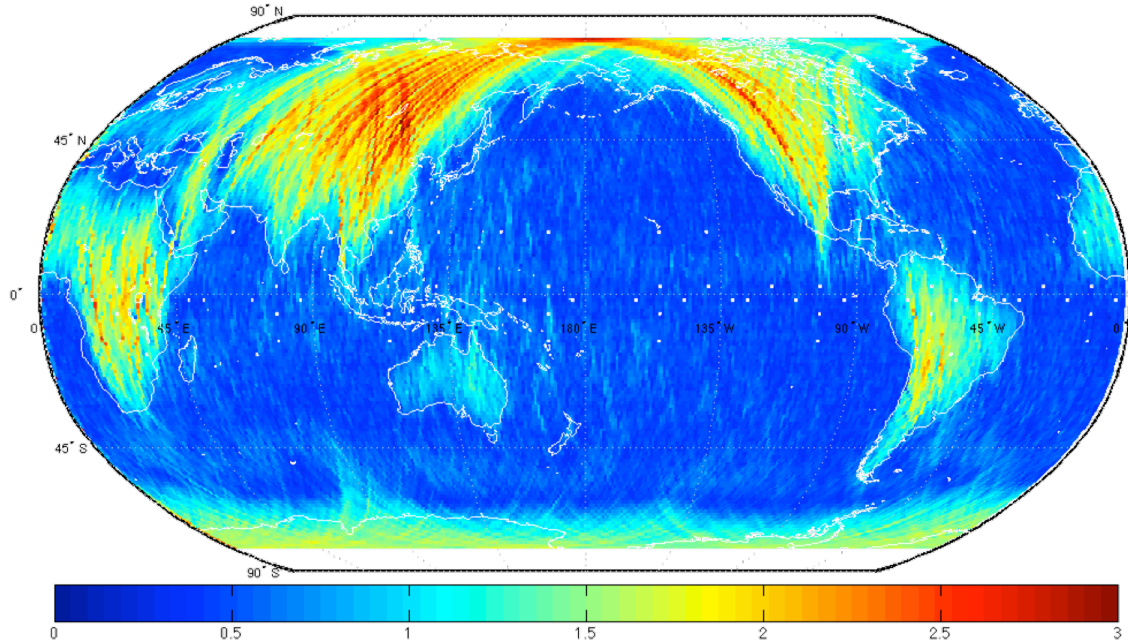


Figure 43. Illustration of the global residual systematic errors after cross-over correction.

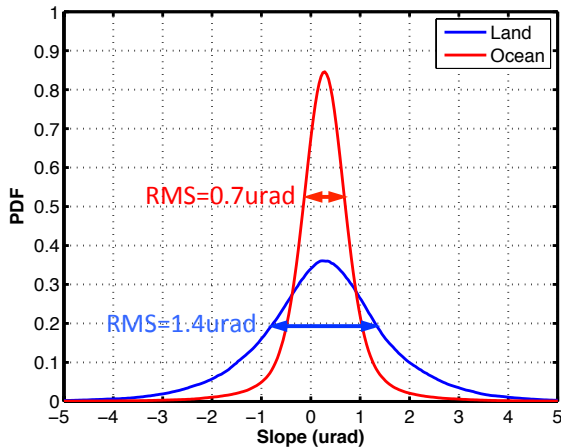


Figure 44. PDF of the residual cross-track slope error after cross-over correction, both over land (blue line) and over the oceans (red line). The associated RMS is 0.7 urad over the oceans and 1.4 urad over land.

We now consider the along-track error integrated over the land pass between cross-over points. A bound to the accumulated error can be obtained from simply integrating the power spectral density of the error. Considering that most errors follow a generic power law PSD given by

$$E(f) = Af^{-\alpha} ,$$

with $\alpha > 1$, the variance of the error accumulated over a pass of length L is bounded by:

$$\sigma_L^2 = \int_{1/2L}^{\infty} df Af^{-\alpha} = \frac{2^{\alpha-1}}{\alpha-1} AL^{\alpha-1}$$

for the particular case of $\alpha=2$, this reduces to:

$$\sigma_L^2 = 2AL$$

For the error budget, the main quantity of interest is the RMS of the error for all the land passes. An effective pass length can thus be estimated from the above result, which will yield the effective length to be considered when retrieving the integrated error for all passes in an RMS sense. Given that the global RMS is given by:

$$\sigma^2 = \frac{\sum_n \left(\frac{2^{\alpha-1}}{\alpha-1} AL_n^{\alpha-1} \right) L_n}{\sum_n L_n} = \frac{2^{\alpha-1}}{\alpha-1} A \frac{\sum_n L_n^\alpha}{\sum_n L_n}$$

the effective pass length is thus:

$$L_{eff} \approx \left(\frac{\sum_n L_n^\alpha}{\sum_n L_n} \right)^{\frac{1}{\alpha-1}}$$

which for $\alpha=2$ reduces to:

$$L_{eff} \approx \left(\frac{\sum_n L_n^2}{\sum_n L_n} \right)$$

The resulting effective length to be considered is however the RMS length of the passes between cross-overs. The resulting effective length computed for the lengths between cross-overs is approximately 3,500 km, and therefore the integration range that needs to be considered for the error that is accumulated over land for a error spectrum of slope -2, is $[1/7,000, \infty]$ cy/km, resulting in an integrated error of $7,000A$.

It is also important to note that the cross-over correction obtains a slope at cross-over points, and therefore is not automatically eliminating height biases that would result from integrating some of the drifts over long periods of time. While relative height biases between passes at cross-over points could also be estimated, this approach has limitations due to the inherent variability of the ocean. Instead, the algorithm needs to use the coincident nadir altimeter measurements, averaging them for relatively long durations as required so as to reduce the random error of the altimeter (the vast majority of the nadir altimeter error is random, and not drifts, as demonstrated by its capability in the Jason series to track sea-level rise). Therefore, the KaRIn measurements in the near swath would be averaged for the same durations, and corrected to follow the nadir altimeter height measurements, thereby reducing height errors associated to long-term drifts to very small levels.

6.3 Hydrology Random Error Requirements

6.3.1 Height Error

The KaRIn random performance needs to consider the fact that over land, KaRIn performs azimuth pre-summing by a factor of 2 (or 2.5), and BFPQ to 3 bits. In addition, a flat σ_0 of 10 dB across the swath is considered. This results in the random performance across the swath shown in the figure below (in the following, a presuming factor of 2.5 has been considered), with a swath average (10 km to 60 km) of 4.4 cm (including 5 dB of SNR margin).

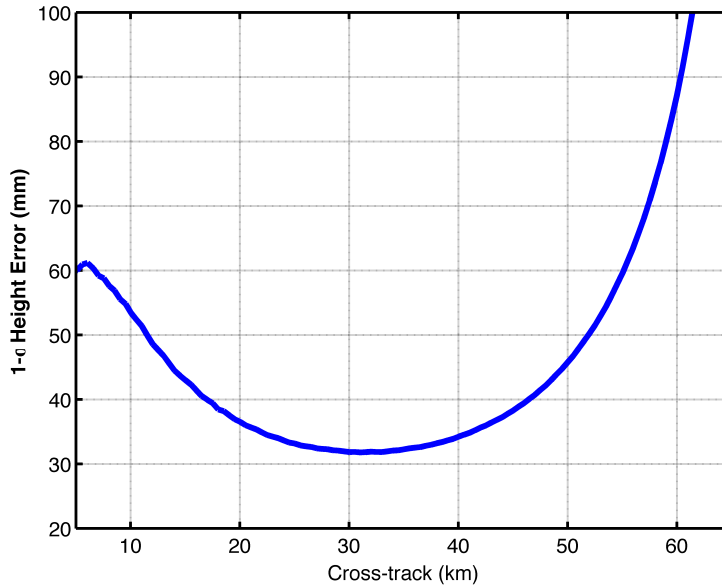


Figure 45. KaRIn random performance across the swath (requirement is specified from 10 to 60 km).

6.3.2 Slope Error

The slope requirement is dominated by the high-frequency noise of the KaRIn system. Considering a river or surface water body of width W and length L , we first need to translate the standard deviation of the random height error specified at 1 km², $\sigma_h^{(1\text{ km}^2)}$, to the spectral density that corresponds to a pixel of size given by the river width; this would then be the noise level that will be integrated along the length of the water body to retrieve the slope error. The scaling from 1 km to W (also in km) is simply given by:

$$N_{\text{random}}(k) = \sigma_h^{2(1\text{ km}^2)} [\text{cm}^2] / [1/\text{km}] \frac{2}{W[\text{km}]} \quad [\text{cm}^2/\text{km}^{-1}]$$

Given this, the spectral density of the slope error can now be computed as (see appendix B for a complete derivation of the PSD of the slope):

$$\text{Slope}_{\text{random}}(k) = N_{\text{random}}(k) [\text{cm}^2/\text{km}^{-1}] (2\pi)^2 \left(f \left[\frac{1}{\text{km}} \right] \right)^2 \left(\frac{10 \mu\text{rad}}{\text{cm}/\text{km}} \right)^2 \quad [\mu\text{rad}^2/\text{km}^{-1}]$$

which is effectively the derivative of the height error; in frequency domain, this is equivalent to multiplying by a factor of $(2\pi)^2 f^2$. This has the effect of turning a “flat” white noise random height error into a red spectrum that grows as f^2 at the high frequencies. The overall RMS slope error for the random component can now be derived by integrating the above equation over the length of the water body:

$$\sigma_{\text{slope}}^2 = \int_0^{\frac{1}{2L}} dk \text{Slope}_{\text{random}}(k) = \frac{(2\pi)^2}{12} 10^2 \sigma_h^{2(1\text{ km}^2)} [\text{cm}^2] \frac{1}{L^3 W} \quad [\mu\text{rad}^2]$$

Perhaps the most interesting outcome of this derivation is that the error decreases inversely proportional to the water body area plus a L^2 factor; while white random noise decreases strictly with the area, the slope error is a red spectrum, and therefore the error decreases significantly faster with the length of the water L . This fact is illustrated in the figure below, where the line of

a constant slope error consistent with the random error allocation is plotted as a function of water body width and length; this corresponds to in fact solving the above equation for the particular case where $\sigma_h^{(1 km)} = 4.4 cm$ and a standard deviation of the slope, σ_{slope} of $8 \mu rad$, as given by the following equation:

$$W = \frac{1}{(\sigma_{slope})^2} \frac{(2\pi)^2}{12L^3} 10^2 \sigma_h^{(1 km)}$$

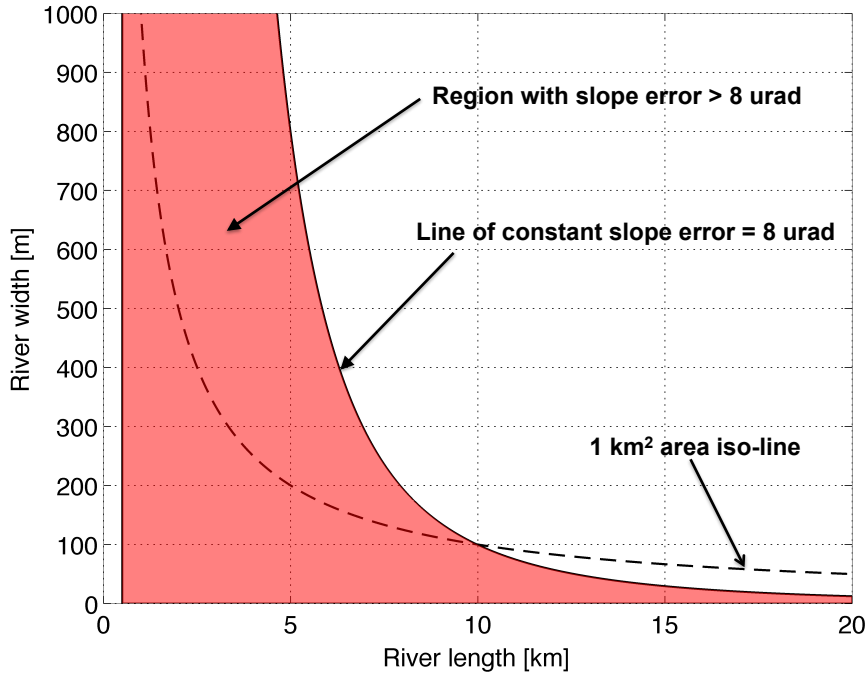


Figure 46. The areas where a certain pair of water body width and length would exceed a slope error of $8 \mu rad$ is illustrated by the highlighted area in red. Also show, for reference, is the line of constant $1 km^2$ area.

A different way to illustrate this is shown in the figure below, where the slope error is shown against the averaging length for widths of 50 m, 100 m, 200 m, and 500 m.

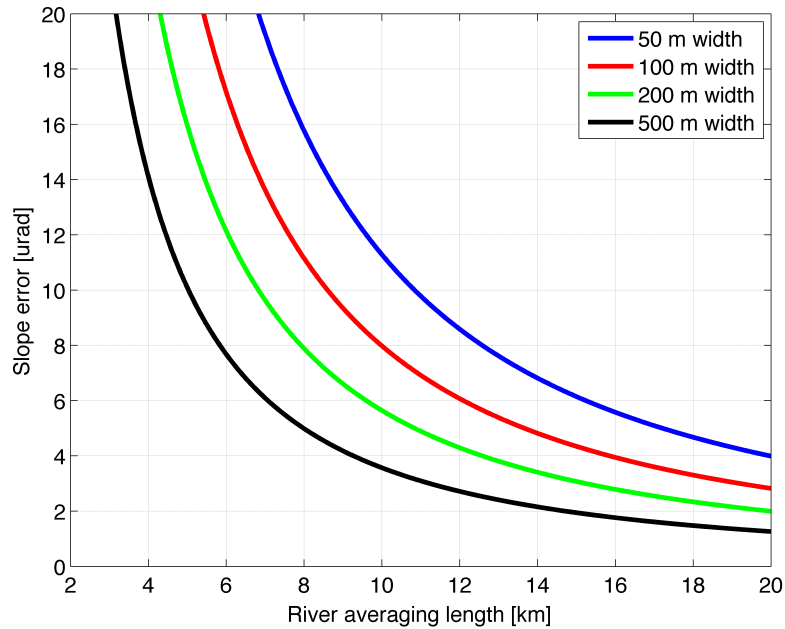


Figure 47. Slope error as a function of averaging length for different widths (not including systematic or media errors)

6.4 Systematic errors

The overall flow down of the key systematic errors across mission elements is shown in the figure below, with every component discussed in the following sections.

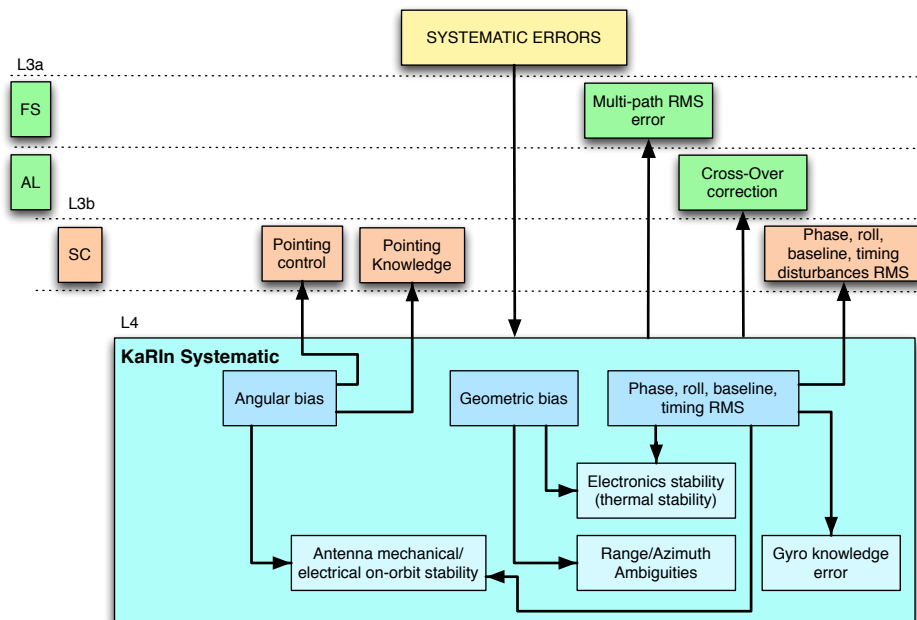


Figure 48. Conceptual high-level flow-down of the systematic error to the key mission elements.

The flow down is similar to the ocean; the difference here is that: 1) the errors are not expressed as a PSD since specifying how the errors are temporally accumulated is not relevant, rather only that the individual integrated error allocations over the effective pass length is met; given that the effective pass length is greater than 1,000 km, the allocations constitute separate requirements

from the ocean spectra; and 2) in forming the high resolution images for surface water bodies, it is necessary to impose additional constraints on systematic errors above the 1 km (6.5 Hz). This will constitute “high-frequency” error allocations, formulated as the equivalent of integrated RMS for frequencies from 6.5 Hz to infinity. The expected source of these errors is not thermoelastic effects, rather disturbances such as the ones generated by the S/C bus reaction wheels, solar array rotations, etc.

The derivation of the systematic errors starts from the PSD of the systematic errors that is required for the ocean, and above 1,000 km, the systematic error is allowed to grow at a faster slope, to balance the errors across the error budget. The expression of the overall systematic error PSD is given by:

$$E_{systematic}(f) = \begin{cases} 2.21 \cdot 10^{-6} f^{-2.733}, & f \leq 10^{-3} \text{ cy/km} \\ 1.1 \cdot 10^{-5} f^{-2.5}, & 0.021 > f \geq 10^{-3} \text{ cy/km} \\ 1.71 \cdot 10^{-1}, & f > 0.021 \text{ cy/km} \end{cases}$$

Similarly to the ocean requirements, the break-down of the systematic requirements is as follows: 60% to phase, 20% to roll, 5% to dilation, 10% to timing (5% left as unallocated margin), while the gyro knowledge error is allocated separately.

The along-track slope errors can be obtained for every systematic error component by integrating its spectrum in a similar fashion as what was done for the random error, i.e.:

$$\int_{1/2L_{eff}}^{\infty} df \text{ Slope}_{systematic}(f) = \int_{1/2L_{eff}}^{\infty} df (2\pi)^2 f^2 \left(\frac{10 \mu\text{rad}}{\text{cm/km}} \right)^2 E_{systematic}(f)$$

This results in the following top-level allocations, where $2L_{eff}=7,000$ km is imposed, corresponding to a time duration of 18 min.

Systematic Error Component	Height Error [cm]	Along-track Slope Error [urad]	Comments
Roll error	0.94	0.096	These errors is corrected by cross-overs and the residual (uncorrected) error is the RMS integrated up to 7,000 km (0.00092 Hz)
Phase error	1.63	0.166	
Gyro roll knowledge error	1.30	0.230	
Dilation error	0.47	0.048	These errors are not corrected by cross-overs and therefore these are the RMS integrated down to 0 Hz.
Timing error	0.67	0.068	
Total Systematic Allocation (RSS)	2.4	0.3	

From the perspective of the high-frequency errors, there are different scenarios that need to be taken into account, depending on how the river is aligned with respect to the flight track. The bounding cases appear when considering that the river is either parallel, or perpendicular, to the flight track, as illustrated in the figure below.

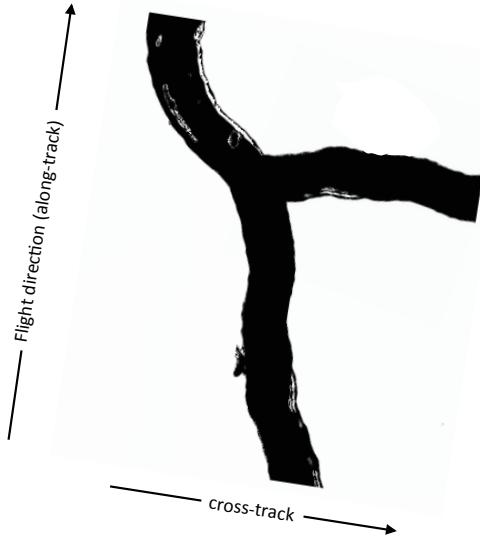


Figure 49. Illustration of the two cases considered for high frequency slope errors for a river (represented by the black surface), where one reach is aligned in the flight direction and the other one perpendicular to it.

In cases where the river is roughly oriented perpendicular to the flight direction, and for relatively small river widths, a high frequency disturbance will basically introduce an instantaneous, constant slope error across the reach length, which can be seen as an additional cross-track slope in addition to the residual slope after cross-over correction. As such, and approximating for the moment that all error sources (phase, baseline, and roll) contribute solely as a linear slope, the error is simply given by the integral of the PSD of the height error, as an effective RMS above 6.5 Hz, converted to an angle by dividing by the equivalent cross-track distance, \bar{C} .

$$(\sigma_{slope}^{HF})_{cross-track}^2 = \frac{1}{\bar{C}^2} \int_{6.5 \text{ Hz}}^{\infty} df E_{systematic}(f)$$

In cases where the river is roughly oriented in the flight direction, the disturbances really need to be considered as a slope spectrum given by:

$$(\sigma_{slope}^{HF})_{along-track}^2 = \int_{6.5 \text{ Hz}}^{\infty} df (2\pi)^2 f^2 \left(\frac{10 \mu\text{rad}}{\text{cm/km}} \right)^2 E_{systematic}(f)$$

However, the slope will not be estimated by integrating the along-track spectrum. In its most basic form, the algorithm to estimate the slopes will use a linear fit to the height measurements over a distance of 10 km for every line of high-resolution pixels within the river width. Effectively, this can be seen as a low-pass filter that will remove any high-frequency components above 1 km. Therefore the effect on the slopes of these high-frequency terms can be neglected, given that they are already bounded by the errors introduced in the cross-track direction.

The requirements integrated from 6.5 Hz to 0.00092 Hz (18 min) are thus as follows:

- Roll: 45 msec (1-sigma), sub-allocated as 14 msec (1-sigma) to the Flight System for disturbances, and 43 msec (1-sigma) to KaRIn.
- Phase: 161 mdeg (1-sigma), sub-allocated as 32 mdeg (1-sigma) to the Flight System for disturbances, and 158 mdeg (1-sigma) to KaRIn.
- Baseline: 21 um (1-sigma), sub-allocated as 6 um (1-sigma) to the Flight System for disturbances, and 20 um (1-sigma) to KaRIn.
- Timing: 44.7 ps (1-sigma), only sub-allocated to KaRIn.
- Gyro: the gyro knowledge error is sub-allocated 0.065 msec (1-sigma), only sub-allocated to KaRIn.

At the other end of the spectrum, the high-frequency (>6.5 Hz) RMSs are derived from allowing each error to create a maximum of 1.15 cm height error at the equivalent center of the swath, which is 37.9 km, as derived in the ocean section. For a roll, this means:

$$\delta\theta_{roll} \approx 10^{-5} \left(\frac{648000}{\pi} \right) \frac{\delta h_{[cm]}}{C_{[km]}} \left(1 + \frac{h}{R_E} \right)^{-1} = 47.6 \delta h_{[cm]} \text{ [msec]}$$

and therefore the roll allocation is an overall RMS error of 34 milliasec. For phase, the error is:

$$\delta\phi \approx 10^{-2} \frac{180}{\pi} \left(\frac{B_{[m]} k_{[m]}}{C_{[km]}} \right) \left(1 + \frac{h}{R_E} \right)^{-1} \delta h_{[cm]} = 98.9 \delta h_{[cm]} \text{ [mdeg]}$$

For baseline dilation the error is:

$$\delta B \approx -10^{-2} \left(\frac{B_{[m]} H_{[m]}}{C_{[km]}^2} \right) \left(1 + \frac{h}{R_E} \right)^{-1} \delta h_{[cm]} = -56 \delta h_{[cm]} \text{ [\mu m]}$$

where B is 10 m.

The high-frequency (>6.5 Hz) RMS errors are allocated as follows:

- Roll : 34 msec (1-sigma) to the Flight System, sub-allocated as 30 msec (1-sigma) to S/C bus and 16 msec (1-sigma) to KaRIn.
- Phase: 71 mdeg (1-sigma) to the Flight System, sub-allocated as 50.2 mdeg (1-sigma) to S/C bus, and 50.2 mdeg (1-sigma) to KaRIn.
- Dilation: 24 μm (1-sigma) to the Flight system, sub-allocated as 20 μm (1-sigma) to S/C bus and 13 μm (1-sigma) to KaRIn.

The associated height errors for each element are shown in the table below.

High-frequency (>6.5 Hz) Error Component	F/S allocation	S/C bus sub-allocation	KaRIn sub-allocation
RMS Roll > 6.5 Hz (Height error) (Cross-track slope error)	34 msec	30 msec	16 msec
	(0.71 cm) (0.19 urad)	(0.63 cm) (0.17 urad)	(0.33 cm) (0.09 urad)
RMS Phase > 6.5 Hz (Height error) (Cross-track slope error)	71 mdeg	50.2 mdeg	50.2 mdeg
	(0.72 cm) (0.19 urad)	(0.51 cm) (0.135 urad)	(0.51 cm) (0.135 urad)
RMS Baseline > 6.5 Hz (Height error) (Cross-track slope error)	24 μm	20 μm	13 μm
	(0.43 cm) (0.11 urad)	(0.36 cm) (0.095 urad)	(0.23 cm) (0.06 urad)
Total Allocation (RSS)	1.1 cm 0.29 urad	0.89 cm (0.24 urad)	0.65 cm (0.17 urad)
Unallocated Margin (RSS/SUM)	0.36 / 0.05 cm (0.4 / 0.21 urad)	0.23 / 0.025 cm (0.25 urad / 0.11 urad)	0.23 / 0.025 cm (0.3 urad / 0.18 urad)
Total (RSS) RMS Error	1.15 cm 0.5 urad	0.92 cm 0.35 urad	0.69 cm 0.35 urad

6.4.1 Orbit Knowledge Error Requirements

As previously discussed, the knowledge error of the true radial height above a reference surface has several contributors: 1) errors in the orbit determination of the satellite: the fundamental vector provided by POD is from the Center of Mass (CM) of the Earth system to the CM of the satellite. The required error figure of 1.5 cm RMS (a 24h RMS number) to cover the ocean

wavelengths greater than 1,000 km with the nadir altimeter pertains to the uncertainty in the radial component of this ~7,400 km long vector. Many phenomena contribute to this error, including modeling errors of atmospheric drag, solar radiation pressure and gravitational effects. It is important to note that this error already accounts for drifts in the phase center of the POD instruments. The same requirement already levied on the POD is compatible with the errors associated to retrieving the height of the satellite CM above the reference ellipsoid for hydrology; in order to meet this requirement, the POD requires an absolute knowledge error of the FS CoG of 5 mm. 2) drifts in the CoG of the satellite. From a POD perspective, the satellite's CoG is moving smoothly around the Earth's center, and any changes (due to vibrations, thermoelastic effects including solar panel snaps, or fuel consumption, for example) will introduce a separate radial height error. The vector from the satellite CM to the DORIS or GPS phase center can actually be estimated as part of the POD process as a "nuisance parameter", and while this has been done for the Jason altimeters under certain circumstances to verify the prelaunch vector, or to identify potential mis-modeling of e.g. GPS antenna phase variations (due, for example, to multipath), these solutions are done outside of the science data system and are therefore not used operationally; the Flight System is therefore levied a not-to-exceed knowledge drift error requirement of 5 mm; and 3) drifts in the radial height of KaRIn's interferometric baseline (or, for the altimeter in the radial position of its phase center). Deformations of KaRIn's mechanical boom, due to on-orbit thermoelastic effects or dynamic disturbances would shift the radial position of the interferometer's baseline, resulting in a height error. While there is some commonality with shifts in the CoG (i.e., a thermoelastic deformation of the intererometric baseline can also induce a CoG shift), the radial displacement of the baseline would directly introduce a height error that is independent of how the deformation impacts the mass distribution of the satellite. Therefore, a requirement is levied on the stability of the radial center of KaRIn's interferometric baseline of 1 mm.

The POD errors are expected to be independent of thermoelastic effects that would cause drifts in the satellite's CoG and deformations of the KaRIn interferometric baseline. Therefore, the later two are added as a direct sum, which is then RSSed to the POD performance requirement. The allocation breakdown is captured in the table below.

Orbit Radial Error	Height Error [cm]
POD	1.5
Flight System CoG knowledge error	0.5
KaRIn baseline radial stability	0.1
Total Radial Error	1.62

The POD slope errors also need to be specified in order to meet the overall slope error requirement; an allocation of 0.5 urad is therefore levied on the Flight System and the POD performance. The allocation breakdown for slopes is captured in the table below (the same approach of direct sum and RSS as for height is used for slopes as well).

Orbit Radial Error	Slope Error [cm]
POD	0.4
Flight System CoG slope knowledge error	0.2
KaRIn baseline radial slope stability	0.1
Total Radial Error	0.5

6.5 LAND MEDIA ERROR REQUIREMENTS

6.5.1 Wet troposphere

The typical variability of the wet troposphere signal over land can be characterized from the quality controlled Integrated Global Radiosonde Archives (IGRA). An analysis of 981 globally distributed stations, using path delay profiles from 1980 to 2010, has been used to derive representative estimates of the mean values of the signal, as well as of the variability that can be expected between different passes. These are shown in the figures below.

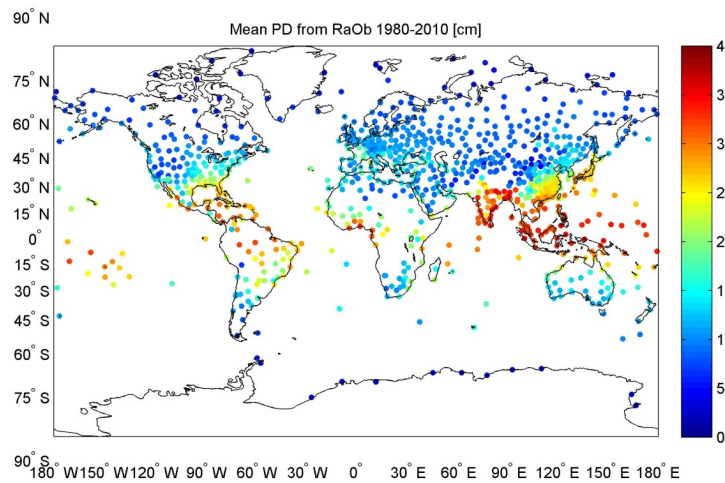


Figure 50. Mean path delay in cm, for each station.

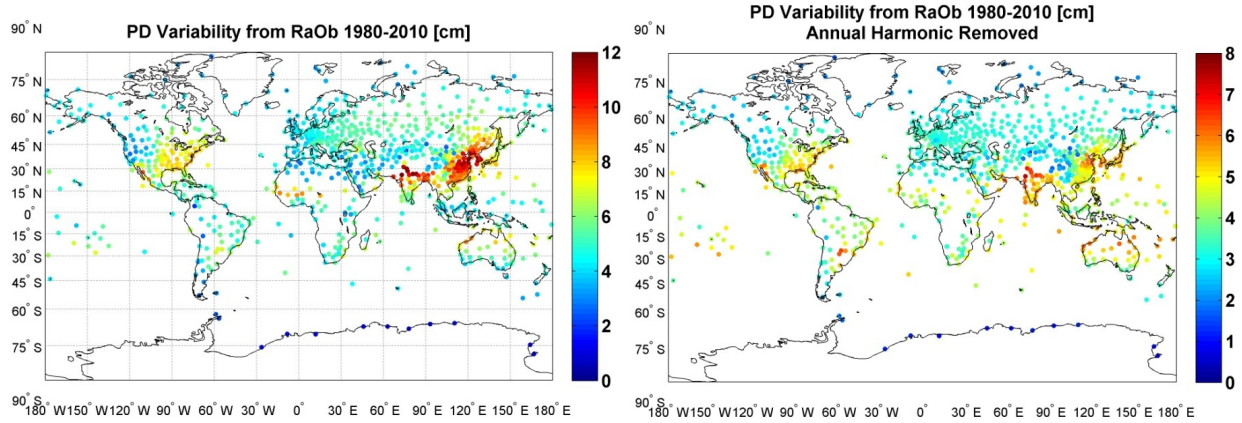


Figure 51. (left) total variability at each station derived from the path-delay standard deviation from 1980 to 2010; (right) variability after removing the annual harmonic

As one would expect, the variability scales with the magnitude of the path delay signal, with lower variability in winter in mid-to-high latitudes, and higher variability in low latitudes and in the summer months in mid latitudes. The total variability of the path delay, shown in the figure above, reaches a maximum of 12 cm. This is in fact dominated by the annual signal, and decreases to less than 7 cm maximum after removing it.

However, a model can be used to remove a significant fraction of the path delay signal. For example, the NCEP reanalysis product, available every 6 hours at a 2.5 deg resolution can be used to this end (other models such as MERRA and ECMWF are also available). An analysis performed by comparing the NCEP model estimates to actual measurements acquired by the US Department of Energy’s atmospheric radiation measurement facilities, most of which include an upward looking microwave radiometer providing 1-min measurements of the wet tropo path delay, shows that the difference is always smaller than 4 cm at all stations, ranging from 1.1 cm to 3.8 cm; the measurement error of the radiometers is estimated to be approximately 0.5 cm, so most of the residual error points to the model.

Based on this, the allocation to the wet tropo error over land is 4 cm, and would require the Algorithm System to implement the ingestion of model estimates to correct the wet tropo variability.

6.6 Dry troposphere and Ionosphere

The dry troposphere and ionosphere signals for hydrology are extracted from models. We have used the ECMWF pressure model for the dry troposphere and the Ionex model for the ionosphere. Based on global simulations of these models, we extract the following spectral envelopes after removing the annual mean:

$$E_{dry\ tropo}(f) = 2 \cdot 10^{-7} f^{-3} \quad [cm]$$

$$E_{ionosphere}(f) = \begin{cases} 1.1 \cdot 10^{-13} f^{-4.593}, & f \leq 3.2 \cdot 10^{-3} \\ 3.15 \cdot 10^{-2}, & f > 3.2 \cdot 10^{-3} \end{cases}$$

These spectra are shown in the figure below:

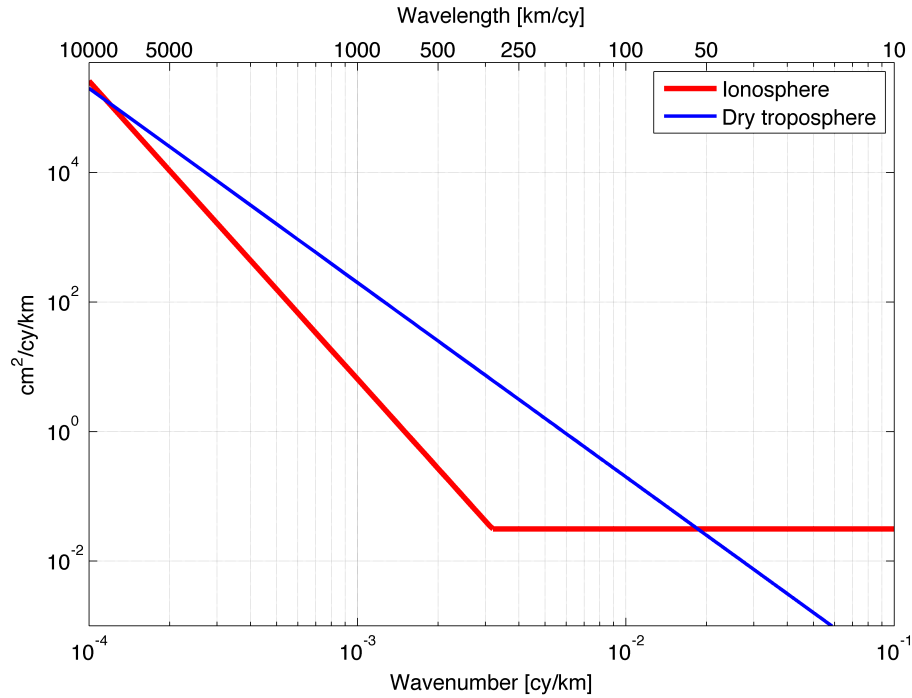


Figure 52. Spectral envelopes for the ionosphere and dry troposphere signals over land.

For the dry troposphere, the overall RMS error integrated over 2,000 km is 0.64 cm, and it is 3.75 cm over 10,000 km. For the ionosphere, the overall RMS error integrated over 2,000 km is 0.2 cm, and it is 3.77 cm over 10,000 km.

The current allocations of require global models are used to reduce these errors over land, to at least eliminate the global daily mean. The dry troposphere is to be corrected with weather models, like it is done operationally for the Jason series of altimeters, and the ionosphere will use ionospheric models such as Ionex.

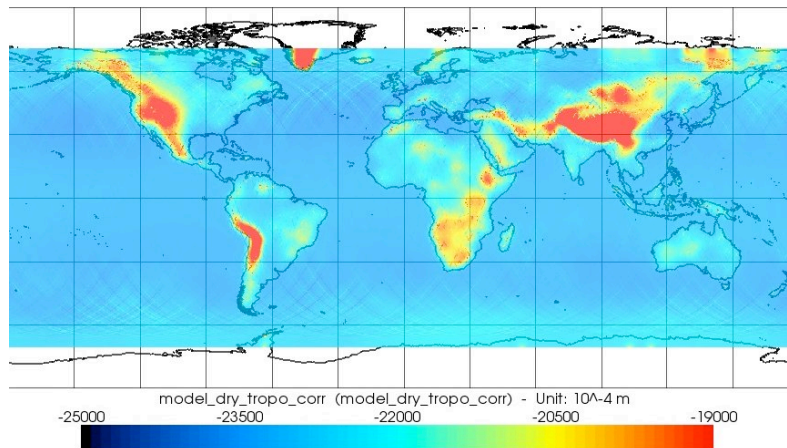


Figure 53. Example of the amplitude in meters of the dry troposphere correction computed from the ECMWF atmospheric pressures and model, as used to correct Jason-1.

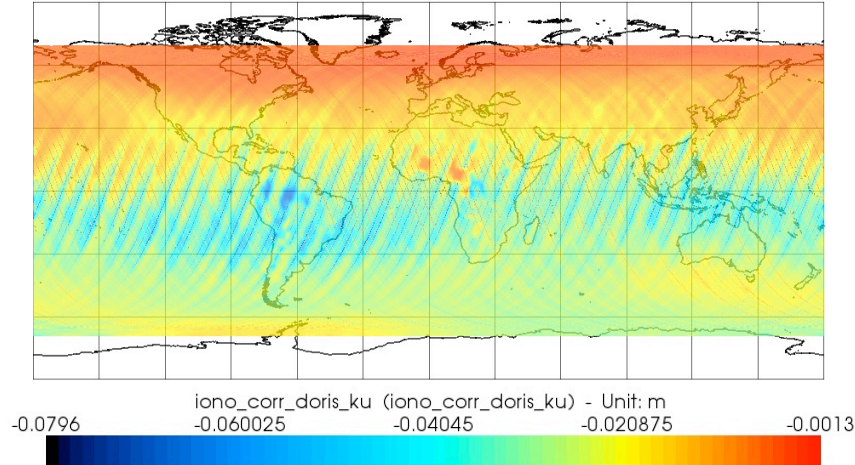


Figure 54. Example of the amplitude in meters of the ionospheric correction derived from DORIS measurements, as used to correct Jason-1.

The slopes that these media errors introduce, computed integrating the corresponding slope spectra, are small, at less than 0.1 urad for both signals.

6.7 Classification accuracy

The primary way in which water can be distinguished from land is due to the greater brightness of water relative to land. In its simplest and crudest form, the classification could take a number of looks by spatial averaging the full-resolution pixels to reduce the classification error, and then define classification thresholds based on land return statistics, followed by a simple 2-class Bayesian classification based on a single threshold for a local area. When considering a classification that is based on a single-pixel basis, it can be shown that the Bayesian classifier is in fact optimal. A post-classification algorithm would then remove outliers and consolidate water bodies.

The classification scheme can be conceptualized as finding the power threshold, P_t , where the two distributions of the powers associated to water, f_{water} , and land, f_{land} , meet, ie. $f_{water} = f_{land}$. For a small number of looks, the land or water pixel statistics, being dominated by speckle, are not Gaussian; instead, they can be modeled as follows:

$$f_{water}(N, P_w, P_n) = \frac{1}{(N-1)!} \frac{N^N}{P_w + P_n} \left(\frac{p_t}{P_w + P_n} \right)^{N-1} e^{-\frac{Np_t}{P_w + P_n}}$$

and

$$f_{land}(N, P_l, P_n) = \frac{1}{(N-1)!} \frac{N^N}{P_l + P_n} \left(\frac{p_t}{P_l + P_n} \right)^{N-1} e^{-\frac{Np_t}{P_l + P_n}}$$

where N is the number of looks, P_w and P_l are the expected value of the water and land power levels, respectively, and P_n is the noise level.

When the noise power level is close to the land power level, ie. $P_l + P_n \sim P_n$, as would be the case for SWOT since the return from land is expected to be below the noise level, a closed-form approximate solution can be found for the power threshold for an arbitrary number of looks (otherwise the solution depends on N), which is given by:

$$p_t = \frac{P_n}{P_w} (P_w + P_n) \log \left(\frac{P_w + P_n}{P_n} \right)$$

The misclassification probability can then be derived by integrating the respective tails of each distributions above/below the threshold value. In this case, a numerical simulation without making the above approximations has been used to find the threshold and derive the misclassification probabilities. The figure below present below swath-averaged results for different number of looks for a land σ_0 of 0 dB. In this simplified analytical analysis, the cross-track resolution varies from 10 m to 70 m (consistent with the KaRIn instrument resolution across the swath), and $N \times 6.6$ m (i.e., $N \times$ single-look resolution \times presume factor, where here we consider the worst-case presume factor of 2.5 discussed earlier). It is also worth noting that: 1) the classification probabilities are not symmetric, with water being more likely (mis)classified as land; and 2) this is a biased classification method, particularly for water bodies with areas close or comparable to the averaged resolution. This is because, due to the contrast, it is likely to classify a pixel that contains a significant portion of land, as water. More sophisticated classification methods based on mixed-pixel statistics can be envisioned which, together with using the coherence estimates in addition to the power images, can improve the classification performance and reduce or eliminate classification biases.

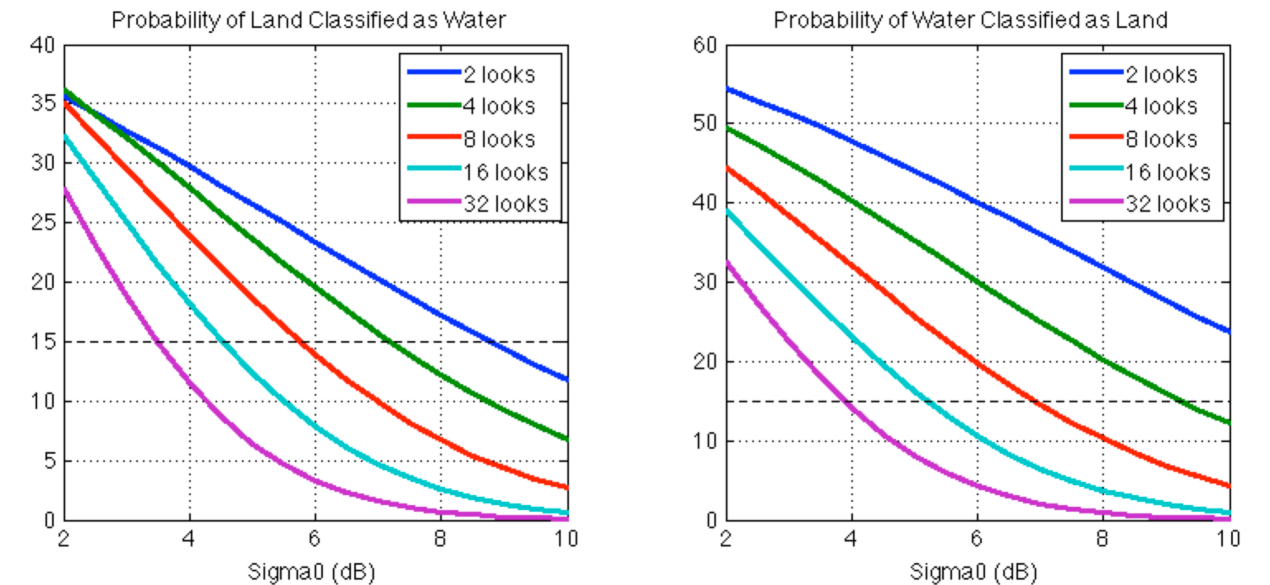


Figure 55. Swath-averaged classification errors for land and water as a function of the σ_0 of the water, and for $N=2, 4, 8, 16$ and 32 . The dotted line represents the current requirement of 15% misclassification. In all cases, a land σ_0 of 0 dB has been used.

As it can be seen from the above figure, this requirement primarily drives KaRIn’s SNR, together with an assumption of the minimum number of looks that can be used (as it relates to the minimum surface water body area).

In addition, the current assumptions for the classification performance include sufficient land-to-water contrast, as well as an absolute brightness of the water, as shown in the figurea above, in order to meet the classification requirement. While these are going-in assumptions, there is the potential that these parameters, at a global scale, may not be fully (or always) consistent with these assumptions. In these cases, height estimates (e.g., height continuity over neighboring water pixels) and correlation estimates (since the lower contrast and slopes of the surrounding

land areas will decrease the correlation) can also be use to help improving the classification retrievals.

7 Flagging Requirements

There are requirements to flag rain, sea ice (for ocean), and layover, rain, and frozen surface water (for surface water), all with an accuracy of 68%. The basic concept to generate the flags is to use a detection algorithm based on return power (SNR loss) and coherence loss (except for ice, which cannot be resolved, and external models are required). The initial assessment is that these requirements do not drive the mission performance requirements beyond what has been already discussed.

A simulation specifically to show the feasibility of meeting the rain flagging accuracy was performed using ocean simulation data that interpolated AMSR-E data to the swath (at 2 km pixels). To perform the evaluation, the AMSR flag was used as a proxy with a 100 km buffer around land (see map of valid data). The probabilities were computed from whether the radiometer pixel - either nadir or center of each swath - detected rain and what was found in the other swath pixels.

The simulation results for the cross-track radiometer are shown in the figures below over different ocean regions and across the swath, covering -60 to + 60 km.

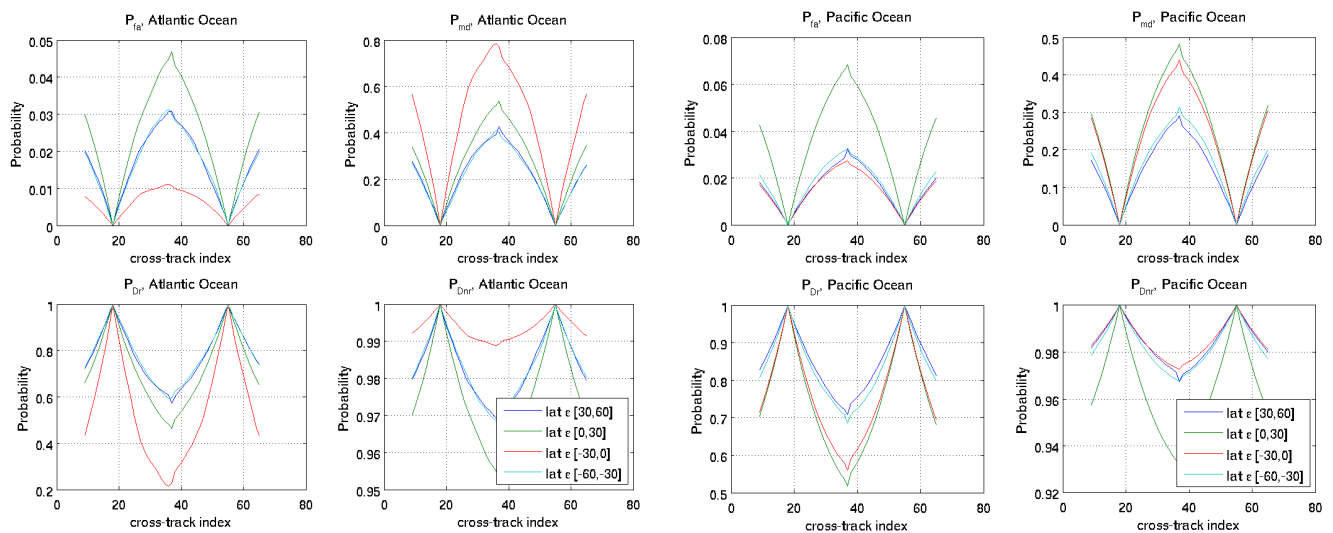


Figure 56. Simulation results for the Atlantic Ocean (left four plots) and Pacific Ocean (right four plots). For each one of these two cases, the four plots show: (1) the probability of false alarm (P_{fa}), upper left; (2) the probability of missed detection (P_{md}), upper right; (3) the probability of detected rain (P_{Dr}), bottom left; and (4) the probability of detected no rain (P_{Dnr}), bottom right.

The table below summarizes the results for each ocean region, which meets or exceeds the required 68% to detect rain in all cases.

Atlantic	Latitude Band: [-60, 60] deg
Probability of	
False Alarm	0.015
Missed Detect	0.281
Detect Rain	0.719
Detect No Rain	0.985
Pacific Ocean	Latitude Band: [-60, 60] deg
Probability of	
False Alarm	0.020

Missed Detect	0.192
Detect Rain	0.808
Detect No Rain	0.980
Indian Ocean	Latitude Band: [-60, 0] deg
Probability of	
False Alarm	0.017
Missed Detect	0.198
Detect Rain	0.802
Detect No Rain	0.983

8 Pointing Error Budget

The pointing error budget is in fact derived primarily from the random and systematic error budget, and it is discussed in this section in detail.

Pointing requirements are broken up into:

- *Absolute pointing control requirements*: mainly driven by the random error performance. Absolute pointing requirements apply to the 3 axis.
- *Relative pointing knowledge requirements*: mainly driven by the systematic error performance, as previously discussed. Roll drift is the driving knowledge requirement.
- *Absolute pointing knowledge requirements*: mainly driven by the systematic error performance, which apply to the 3 axis.

There is also a requirement to yaw-steer the S/C to zero Doppler along the orbit. To first order, this is a very slowly varying sinusoidal steering angle of $\sim\pm 4$ deg with a period of one orbit.

8.1 Absolute Pointing Control Requirements

The main consideration for the absolute pointing control requirement is the overlap of the two interferometric antennas to maintain the SNR. Since a given swath is imaged from both antennas, their footprint on the ground need to overlap to ensure that the overall SNR, as it relates to the random error performance, is preserved. In particular, a roll error can be directly related to a SNR loss. The impact of beam misalignment in the SNR is sufficiently small when the errors amount to less than $1/10^{\text{th}}$ of the beamwidths.

The second consideration arises from the decorrelation associated to the interferometric iso-phase and iso-range misalignment increasing as beams move away from the azimuth boresight (nominally 0 degrees). A pitch or a yaw create an angular decorrelation; a pitch angle has an impact roughly 15 times larger than a yaw.

Finally, SAR operation is typically impacted by the Doppler Centroid, but the onboard processor implements Doppler Centroid tracking to mitigate this error.

The optimal nominal pointing that optimizes the overall interferometric performance is for a nominal KaRIn electrical boresight(s) elevation pointing angle of ± 2.7 deg. In order to preserve the random error performance, the electrical elevation and azimuth boresight angles of the KaRIn antennas need to remain within 0.067 deg (1-sigma) of the nominal angles during science observations. This is in principle compatible with the pointing error requirement for the Jason series of altimeters of 0.2 deg (3-sigma), satisfying the nadir altimeter needs as well. These pointing errors appear both from contributions from the S/C as well as from the KaRIn antennas themselves, and therefore are sub-allocated to both elements. The control requirement of 0.2 deg 3-sigma for all 3-axis yields an additional 1-sigma error of approximately 2.5 mm, and a 3-sigma error 7 mm, which is to be RSS'ed with the nominal random performance. This is illustrated in the figure below.

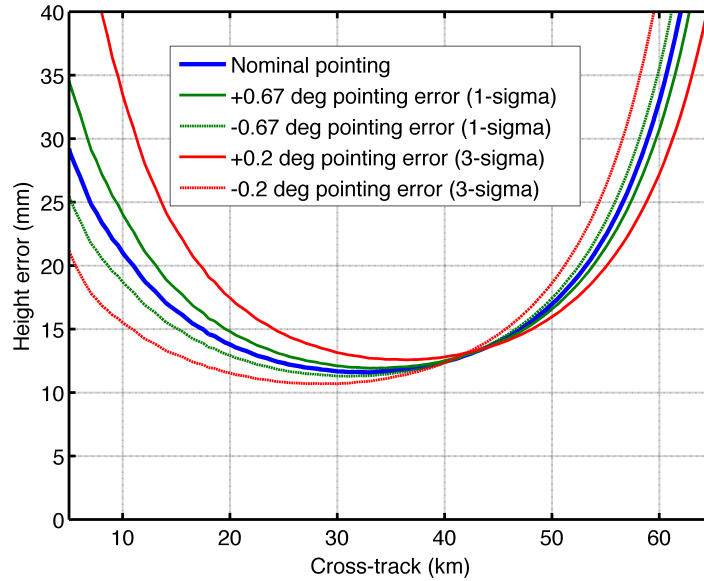


Figure 57. Impact of the overall pointing control error on the random performance of KaRIn for 1-sigma (± 0.067 deg) and 3-sigma (± 0.2 deg) cases.

In addition, the antennas need to maintain a relative azimuth pointing between them. This follows the same principles as before, but it is only sub-allocated to KaRIn. Given the narrow beamwidth of the antennas in the azimuth direction, of approximately 0.11 deg, the requirement is a tenth of that, or 0.011 deg (1-sigma), to yield a 1-sigma error < 1 mm.

8.2 Relative pointing knowledge requirements

The relative pointing knowledge requirements are driven by systematic errors. As discussed in the systematic error section, the roll introduces an error that is proportional to the roll angle error times the cross-track distance; the pitch and yaw introduce significantly smaller errors. Therefore, a knowledge drift error of 2.5 asec over 2.6 min is allocated to the KaRIn gyro (which, in fact, provides the same level of knowledge on all 3 axis).

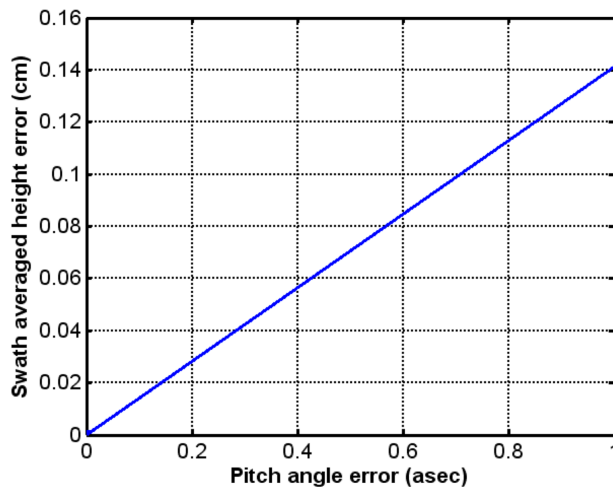


Figure 58. Swath average height error as a function of pitch drift knowledge error

8.3 Absolute pointing knowledge requirements

The absolute pointing knowledge errors are driven by geolocation errors as well as the ability to calibrate out any systematic errors introduced as part of the onboard processing. A pitch knowledge error of 0.01 deg at the 1-sigma pitch control error (0.067 deg) would create systematic errors as high as 6 cm, as shown in the figure below, and which are non linear across the swath.

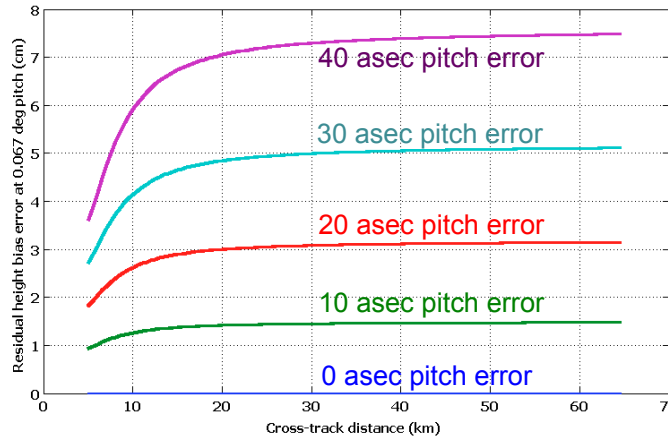


Figure 59. Residual bias errors for different pitch knowledge errors at a pitch of 0.067 deg

In order to ensure that these errors do not create a height non-linearity that exceeds 0.5 cm across the swath (comparable to the magnitude of the residual wet troposphere errors), the absolute knowledge pitch error requirement is specified as 0.006 deg (3-sigma). The sensitivity to roll errors is not as high, and therefore the absolute roll knowledge error requirement is specified as 0.03 deg (3-sigma), as is the yaw. KaRIn does not have any “knowledge” of thermoelastic effects; therefore it is required that any contribution of any thermoelastic effects on the absolute azimuth pointing drift of each of the KaRIn antenna beams shall not exceed 10 asec (0.0028 deg, 3-sigma) throughout the mission life. Note there’s an implicit requirement for alignment knowledge (static component), which needs to be obtained via on-flight calibration.

8.4 Pointing requirements summary

The pointing requirements can be summarized as per the table below:

Requirement	Allocations
Elevation Absolute Pointing Control of 0.2° (3σ)	<ul style="list-style-type: none"> • 0.1° (3σ) to payload (KaRIn) • 0.1° (3σ) to S/C bus (roll and alignment)
Azimuth Absolute Pointing Control of 0.2° (3σ)	<ul style="list-style-type: none"> • 0.1° (3σ) to payload (KaRIn) • 0.1° (3σ) to S/C bus (pitch and alignment)
Azimuth Relative Pointing Control of 0.033° (3σ)	<ul style="list-style-type: none"> • 0.033° (3σ) to payload (KaRIn)
Pointing knowledge drift error	<ul style="list-style-type: none"> • Yaw & Roll: 2.5 asec over 2.6 min (KaRIn)
Absolute Pointing Knowledge: Yaw, Roll - 0.03° (3σ)	<ul style="list-style-type: none"> • Yaw, Roll: 0.03° (3σ) to S/C bus • Pitch:

Pitch - 0.0088° (3σ)	<ul style="list-style-type: none">• 0.006° (3σ) to S/C bus• 0.0028° (3σ) to payload (KaRIn)
Absolute Yaw Steering Control Error of 0.2 deg (3σ)	<ul style="list-style-type: none">• 0.2° (3σ) to S/C bus

9 Timing Correlation Error Budget

The timing errors that are being considered here corresponds to errors in the time-tagging accuracy of the payload data, as required to corregister all the different payload measurements. Errors in the time-tagging will result in systematic errors.

For a given signal $x(t)$ with a Fourier transform given by $X(f)$ and power spectral density (PSD) given by $S_x(f) = \lim_{T \rightarrow \infty} \frac{1}{T} E[|X(f)|^2]$, the error associated to a constant timing (bias) error in measuring it, is given by:

$$\begin{aligned} PSD \{x(t) - x(t - t_0)\} &= \lim_{T \rightarrow \infty} \frac{1}{T} E[|X(f)|^2 - |X(f)e^{-j2\pi f t_0}|^2] = \\ &= |S_x(f)|^2 |1 - e^{-j2\pi f t_0}|^2 \end{aligned}$$

In some cases, the signal is not fully known. However, an estimate of the order of magnitude of the timing accuracy can be obtained as a function of how many times the signal is above a pre-established knowledge requirement level, in spectral form. Assuming that the PSD of the signal, $S_x(f)$, is α times the PSD of a given knowledge requirement, $S_{req}(f)$:

$$S_x(f) = \alpha S_{req}(f)$$

and establishing that the residual error induced by the timing error should not increase the overall error in spectral form by more than p %, then we have that:

$$|1 - e^{-j2\pi f t_0}|^2 \alpha S_{req}(f) \leq \frac{p}{100} S_{req}(f)$$

therefore:

$$\alpha \leq \frac{p/100}{|1 - e^{-j2\pi f t_0}|^2}$$

With some further simple algebraic manipulations we can simplify this equation as follows, resulting in a timing accuracy of:

$$t_0 \leq \frac{1}{\pi f} \text{asin}\left(\frac{1}{20} \sqrt{\frac{p}{\alpha}}\right)$$

It is worth noting that there is a dependence with the frequency, and that the most restrictive time bias will be imposed by the maximum frequency of interest. Therefore, the timing required derived in this way is the one that adds a p % of error at that frequency.

The primary measurement that is most sensitive to timing errors are the gyros, given that they operate at the highest sampling frequency (the KaRIn gyros offer data synchronization via a sync signal, which will be used at 64 Hz), and the roll error, in particular, is one of the most important contributions to the error budget. A relative degradation of the gyro error measurement in a spectral sense of 1% is allocated at the maximum resolved frequency (half the sampling frequency, ie. 32 Hz). The magnitude of the roll signal that will be measurement during the mission is not known, but hereafter assumed to be <1.8 asec over 3 minutes. Given that the error knowledge of the gyro over the same interval integrates to approximately 25 milliasec, this results in a spectral signal-to-error ratio of $(1.8/25e-3)^2 \sim 5 \times 10^3$, requiring an overall time correlation relative stability error between the KaRIn measurement and the gyro measurement of better than 7 usec.

In addition, the system is imposed a 0.1 m ground geolocation knowledge requirement due to timing errors, which corresponds to 16 usec at the S/C velocity of 6.5 km/s.

In summary, the absolute time correlation error with respect to TAI is allocated a not-to-exceed bias of 16 us, which is sub-allocated as follows:

- S/C time 1 PPS absolute accuracy of 10 us.
- KaRIn: 5 us time accuracy (relative to the received 1 PPS).
- KaRIn gyro: 1 us time accuracy (relative to the received 1 PPS).

The a relative error between KaRIn and its gyro is allocated 7 us, which is sub-allocated as follows:

- S/C time 1 PPS stability: 1 us
- KaRIn: 5 us time precision.
- KaRIn gyro: 1 us time precision.

10 Appendix A: Proposed SWOT Orbit

Although more detailed orbital analysis will be captured on a separate document, here we discuss the basic characteristics of the proposed SWOT nominal science orbit, as defined today. These are provided for description purposes only and do not constitute the ultimate orbit/trajectory analysis.

The basic set of osculating orbital parameters are as follows:

- Semi-major axis: 7277.258 km
- Eccentricity: 0.001142
- Inclination: 77.50757728
- RAAN: 345 deg
- Argument of periapsis: 113.5266 deg
- Mean anomaly: 66.3 deg

Which are defined at time 1/1/2020, 12:00:00.

Some basic parameters, such as the geodetic altitude and beta angle for the SWOT platform are shown in the following figures.

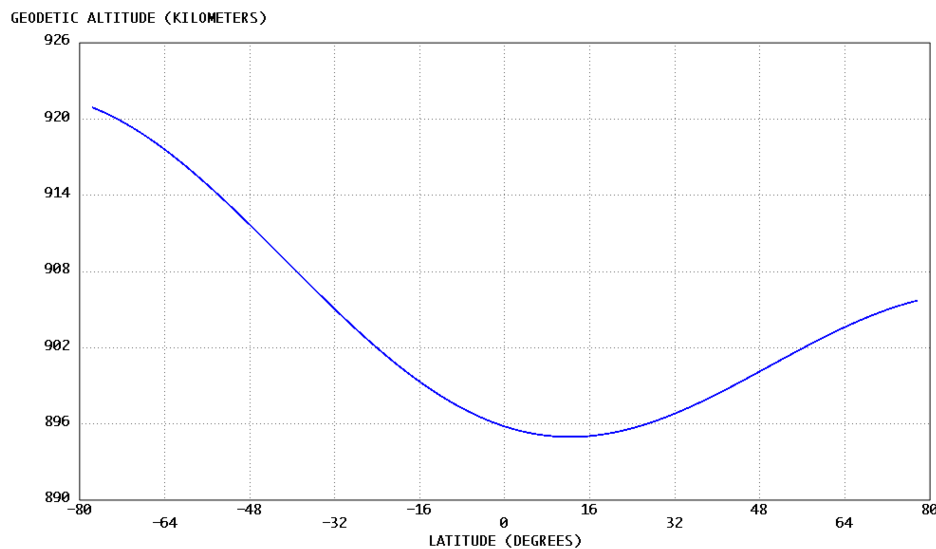


Figure 60. Geodetic altitude (in km) as a function of latitude.

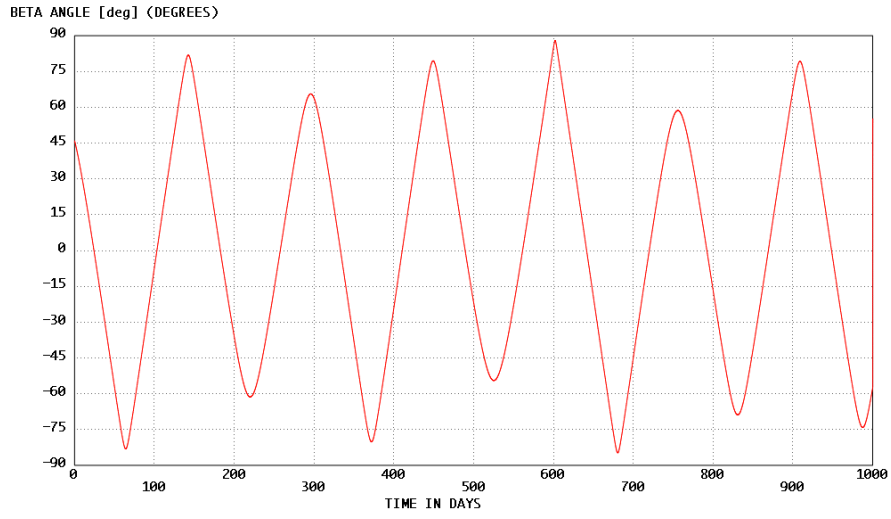


Figure 61. Beta angle as a function time in days

11 Appendix B: Derivation of the spectral form of the slope error

Starting from the basic definition of the slope $s(t)$ as the derivative of the heights, $h(t)$:

$$s(t) = \frac{h(t + \Delta t) - h(t)}{v_g \Delta t} = \frac{1}{v_g} \frac{\partial h(t)}{\partial t}$$

where v_g is the ground speed of the platform, and the units of the slope are radians when $h(t)$ is in cm and v_g is in cm/sec. The Fourier transform of the slopes, $S(f)$, is then given by:

$$S(f) = \int dt \frac{1}{v_g} \frac{\partial h(t)}{\partial t} e^{-j2\pi f t} = \frac{j}{v_g} 2\pi f \int dt h(t) e^{-2\pi j f t} = \frac{j}{v_g} 2\pi f H(f)$$

where $H(f)$ is the Fourier transform of the heights. The power spectral density (PSD) of the slopes, PSD_s is then related to the PSD of the heights, PSD_h by the following expression:

$$PSD_s = \frac{(2\pi)^2 f^2}{v_g^2} PSD_h$$

To convert from $\text{rad}^2/\text{cy}/\text{sec}$ to $\text{rad}^2/\text{cy}/\text{km}$, we need to multiply by v_g in units of km/sec:

$$\begin{aligned} PSD_s[\text{rad}^2/\text{cy}/\text{km}] &= v_g \left[\frac{\text{km}}{\text{sec}} \right] \frac{(2\pi)^2 \left(f \left[\frac{\text{cy}}{\text{sec}} \right] \right)^2}{\left(v_g \left[\frac{\text{cm}}{\text{sec}} \right] \right)^2} PSD_h[\text{cm}^2/\text{cy}/\text{sec}] \\ &= (2\pi)^2 \left(\frac{f \left[\frac{\text{cy}}{\text{sec}} \right]}{10^5 v_g \left[\frac{\text{km}}{\text{sec}} \right]} \right)^2 PSD_h[\text{cm}^2/\text{cy}/\text{km}] \\ &= (2\pi)^2 10^{-10} \left(f \left[\frac{\text{cy}}{\text{km}} \right] \right)^2 PSD_h[\text{cm}^2/\text{cy}/\text{km}] \end{aligned}$$

To convert the slope to units of μrad :

$$\begin{aligned} PSD_s[\text{rad}^2/\text{cy}/\text{km}] &= \left(10^6 \left[\frac{\mu\text{rad}}{\text{rad}} \right] \right)^2 (2\pi)^2 10^{-10} \left(f \left[\frac{\text{cy}}{\text{km}} \right] \right)^2 PSD_h[\text{cm}^2/\text{cy}/\text{km}] \\ &= (2\pi)^2 10^2 \left(f \left[\frac{\text{cy}}{\text{km}} \right] \right)^2 PSD_h[\text{cm}^2/\text{cy}/\text{km}] \end{aligned}$$